VILNIUS UNIVERSITY

CENTER FOR PHYSICAL SCIENCES AND TECHNOLOGY

ROKAS KONDROTAS

ELECTROCHEMICAL DEPOSITION OF Cu-Zn-Sn PRECURSOR AND FORMATION OF $Cu_2ZnSnSe_4$ SOLAR CELL

Doctoral Dissertation

Physical sciences, chemistry (03P)

Vilnius, 2015

This work has been carried out in 2010-2014 at the Department of Characterization of Material structure of Centre for Physical Sciences and Technology

Scientific Supervisor

Prof. dr. Remigijus Juškėnas (Centre for Physical Sciences and Technology, physical sciences, chemistry 03P).

VILNIAUS UNIVERSITETAS

FIZINIŲ IR TECHNOLOGIJOS MOKSLŲ CENTRAS

ROKAS KONDROTAS

ELEKTROCHEMINIS Cu-Zn-Sn PIRMTAKO NUSODINIMAS IR $Cu_2ZnSnSe_4$ SAULĖS ELEMENTO FORMAVIMAS

Daktaro disertacija

Fiziniai mokslai, chemija (03P)

Vilnius, 2015 metai

Disertacija rengta 2010 – 2014 metais Fizinių ir technologijos mokslų centro Medžiagų struktūrinės analizės skyriuje

Mokslinis vadovas

prof. dr. Remigijus Juškėnas (Fizinių ir technologijos mokslų centras, fiziniai mokslai, chemija – 03P)

Table of Contents

Introduction

Growing world population, emerging economies, higher living standards account for the increasing global primary energy consumption. The major part of generated energy is supplied from fossil fuel (coal, natural gas, oil). However, CO_2 is the by-product of burning process of the fossil fuel, which is thought to be one the main cause of the global warming [1]. European Union has set the task to reduce CO_2 emission and increase power generation from renewable energy sources by 20% in 2020. Naturally, in order to minimize CO_2 emission alternative (renewable) energy sources have to be implemented on a wide scale. As of 2013 renewable energy sources (wind, solar, hydro etc.) accounted only for 5.3 % of global power generation [2]. Although alternative energy market share is small, it is rapidly growing and over 2012-2013 power generation from renewable sources increased 16.3%. [2]. Solar power was the fastest growing branch of all renewable energy sources - 33% of growth, accordingly.

Sun is the major source of energy for the planet Earth. Sun provides an enormous amount of energy, it is estimated that average power density provided by the sun per year is 342 W/m^2 [3]. If one calculates amount of energy received to the whole earth, one would obtain 148 PWh. As a comparison, global primary energy consumption was 19.9 TWh in 2013 that means the amount of sun energy, which reaches Earth surface is 7400 times greater than actually required. This shows a huge potential of solar power.

Sun emits energy in a form of heat and light. Depending on how energy is converted several types of solar energy technologies exits:

- Solar hot water. Sunlight energy and heat is used to warm-up water through boiler system. Mostly implemented for domestic purposes.

- Solar electricity. Vast amount of sunlight is concentrated in small area to heat water or salt up to their boiling/melting point. Then turbines powered by steam are exploited to generate electricity. Mostly implemented in solar power plants.
- Photovoltaic systems. Solar panels directly convert sunlight to electricity based on photovoltaic effect in semiconductors. Solar panels are used both for domestic purposes as well as for building solar power plants.

Photovoltaic systems comprises of solar panels, whereas solar panels are composed of solar cells. First modern solar cell was fabricated in 1954 at Bell's lab. It was silicon based solar cell and had 6% power conversion efficiency (PCE). At that time because of very high solar cell fabrication costs and low efficiency it could not compete with other sources of energy. In order to exploit photovoltaic energy on mass scale one had to drastically reduce production cost of solar cells. As a result, second generation solar cells have been invented. Second generation solar cell utilize less expensive materials, effectively absorbs sunlight and cheaper fabrication methods are implemented, consequently production costs are significantly reduced. Second generation solar cells are often referred as thin film (TF) solar cells, because the thickness of the absorber layer usually is only few micrometres thick.

Mainstream technologies of thin film solar cells are a-Si, CdTe and $Cu(In,Ga)Se_2$ (CIGS). Although thin film solar cell technology had high growth expectations their part of photovoltaic energy market is relatively low – 16% [4]. Principally, the maturity of Si technology and China's cost reduction of wafer based technologies suspended TF growth. However, the bright future is forecasted for thin film solar cell technology.

Looking at future perspectives, photovoltaic is a fast growing market and can achieve TW (10^{12} W) level capacity in 10-20 years. Current CdTe and CIGS technologies exploit Te and In metals, which are relatively rare in the earth's

crust – 0.05 and 0.24 ppm, respectively [5]. Because of the scarcity of particular elements and that large part of indium is used for LCD production, substitute for CIGS has emerged – $Cu_2ZnSnSe_4$ (CZTSe) and Cu_2ZnSnS_4 (CZTS). It comprises of earth-abundant (Zn, Sn – 75, 2.2 ppm), non-toxic, elements as well as possess similar physical and optical properties as CIGS, therefore is an ideal absorber for thin film solar cells. However, CZTSe(S) is a more complex system, relatively new material comprising of 4(5) elements and crystallization conditions have not yet been optimized as for example, for CIGS. As a result, record power conversion efficiency for CIGS based solar cells is 21.7% [6], whereas for CZTSSe – 12.7% [7]. This indicates that CZTSe(S) is a complex system and the influence of technological parameters on CZTSe(S) formation mechanisms and its physical properties is not yet well understood.

Scientific novelty

There have been published many papers concerning the formation of Cu-Zn-Sn precursor by electrochemical deposition. In many cases the deposition process took long period of time (10 – 120 min) and solution agitation was rarely present. Here in this work we present optimized electrochemical co-deposition process (composition of electrolyte solution, deposition potential and pH) of CZT films with introduced solution stirring, which allowed to deposit the required 600-700 nm thick films within 3 – 4 minutes only.

In this study we have also presented the new electrochemical deposition setup with flow cell, which allowed to perform sequential layer deposition without exposing samples to the ambient air between deposition of separate layers. Further more, we have showed the application of particular system for stacked Cu/Sn/Cu/Zn precursor electrodeposition.

The published papers on reaction pathways of CZTSe formation often are based on the results of XRD and XRD *in situ* studies, however the selenization

conditions which were implemented in particular studies greatly differed from the conventional ones. In order to reliably determine the mechanism of CZTSe formation precise measurements are required to indentify the intermediate phases under traditional selenization conditions. The task becomes especially challenging, because the most intensive diffraction peaks of ZnSe and Cu_2SnSe_3 overlap with those of $Cu_2ZnSnSe_4$ and cannot be resolved with conventional XRD optics. Thus in this study we present advanced XRD studies of CZT precursor phase composition using CALSA analyzer, which allow to distinguish closely located diffraction peaks.

The surface morphology and cross-section of CZTSe layer have to be thoroughly investigated in order to understand the processes that undergo during selenization. As a consequence, the gained knowledge enables to adjust selenization conditions and as a result high quality CZTSe absorber can be achieved. In the most reported papers of CZTSe formation cleaved cross section of CZTSe films are presented, however it is difficult to judge about the quality of Mo/$MoSe_2$/CZTSe interface and the location of ZnSe secondary phase. On the other hand, high resolution images of interfaces and the occurrence of ZnSe can be detected in FIB prepared cross section. By implementing SEM with embedded FIB we have thoroughly analyzed the interface of Mo and CZTSe.

The aim of the study

The main goal of this study is to fabricate and characterize CZTSe solar cell from electrodeposited CZT precursor. In order to achieve this goal, four tasks have been formulated:

1. To investigate electrochemical co-deposition of Cu-Zn-Sn thin films. By introducing solution stirring to reduce the deposition duration and to

obtain compact, homogenous, smooth and well-adherent to Mo CZT precursor.

2. To examine the possibility of implementing new electrochemical deposition setup with flow cell for sequential Cu, Sn and Zn electrochemical deposition. To find suitable electrolytes and deposition conditions (potential, current density, electrolyte flow rate) for each of the metal electrodeposition.
3. To carry out a detailed investigation of preheating treatment of CZT in the temperature range of 200 – 350 °C. To examine its effect on the selenization process and CZTSe solar cell performance.
4. To investigate the influence of selenization conditions (temperature, duration, Se quantity, Ar pressure) and initial CZT precursor composition on the CZTSe phase composition, morphology and CZTSe solar cell performance.

Scientific statements

1. By introducing solution agitation, the duration of co-deposition of CZT precursor is reduced by a factor of about 5 and homogenous in composition and thickness CZT films are achieved.
2. Using in this study presented new electrochemical deposition setup with flow cell, well-adherent to Mo with targeted composition stacked layer CZT precursor can be successfully deposited.
3. Electrochemically co-deposited CZT precursor with Zn-rich (Zn/Sn=1.1–1.2) and Cu-poor (Cu/(Zn+Sn)=0.8–0.9) composition contains hexagonal η-$Cu_{6.26}Sn_5$, cubic γ-Cu_5Zn_8 and tetragonal Sn phases.
4. The formation of Sn solid solution in η-$Cu_{6.26}Sn_5$ and γ-Cu_5Zn_8 intermetallic compounds occurs during preheating at temperatures

> 250 °C. After the preheating a segregation of Sn in CZT precursor occurs at room temperature.

5. The lack of CZTSe film integrity leads to existence of shunt paths and that could be one of the main reasons for poor overall CZTSe solar cell performance.

1 Literature review

1.1 Cu(In,Ga)Se_2 solar cells

Because CZTSe(S) originated from CIGS by replacing In and Ga ions with Zn and Sn, in this chapter CIGS solar cell technology will be briefly presented. As was mentioned in the introduction CIGS is one of the most developed thin film technology. Currently the highest power conversion efficiency (PCE) of CIGS based solar cells has reached 21.7 %. This is an unexpectedly high value for polycrystalline absorber with hetero p-n junction showing that thin film technologies have high potential to compete with other PV technologies.

CIGS is a direct band gap, naturally appearing as p-type semiconductor. Its crystal structure is chalcopyrite. Band gap value depends on Ga content and can be tunable from 1.0 eV ($CuInSe_2$) to 1.65 eV ($CuGaSe_2$). In the visible spectrum range absorption coefficient of CIGS is very high $\alpha > 10^4$ cm^{-1}, thus only few micrometre thick layer is enough to effectively absorb sunlight. Because of the attractive physical and optical properties, CIGS is an ideal candidate for thin film solar cells. The basic structure of CIGS solar cell is depicted in Fig. 1.1. It consists of three major parts: i) substrate and back contact ii) absorber iii) buffer and window layers.

Substrate. Most often soda-lime glass is used as substrate, but light-weight, flexible substrates has been exploited as well: for example, metal foil, plastic and polymers [9, 10]. All mentioned substrates are coated with Mo layer, which serves as a back contact.

Absorber. There are two major approaches for the formation of absorber layer: (i) co-evaporation of all constituents, firstly developed by Boeing and (ii) sputtering of metallic precursor followed by subsequent selenization or sulphurisation step. Co-evaporation technology has been developing and

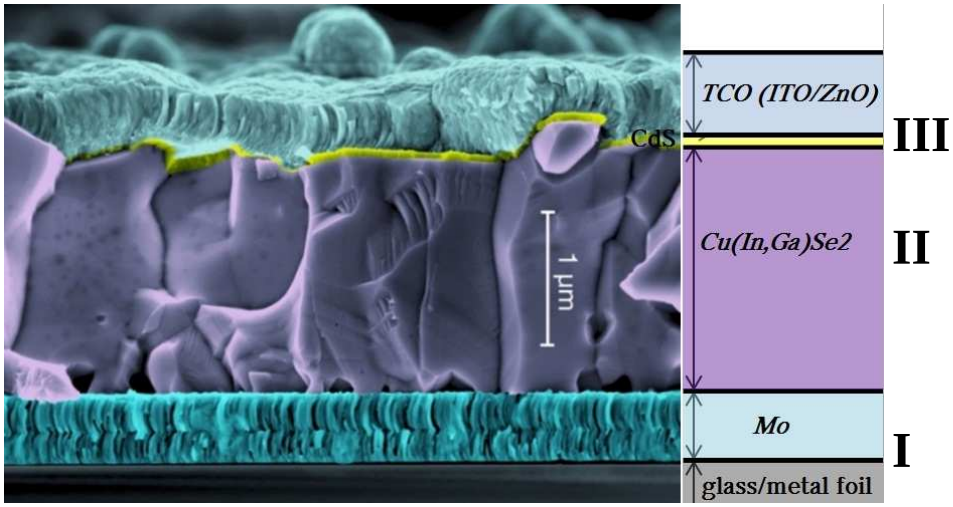

Figure 1.1: Colored SEM micrograph of typical CIGS solar cell structure. (Adapted from [8]).

currently research institutes like NREL, ZSW, Solar Frontier exploit three-stage evaporation of Cu, In, Ga and Se to form CIGS absorber, yielding greater than 19% efficiency [11, 12]. Other companies for example AVANCIS fabricate CIGS layer by annealing precursor in sulphur-containing atmosphere. In this case precursor is fabricated by DC sputtering CuGa and In on Mo substrate then thermally evaporating Se. With latter deposition conditions 14.7% of PCE has been obtained for CIGS mini modules [13]. Other growth methods such as chemical spray pyrolysis [14], paste coating [15] electrodeposition [16, 17] have been also applied for the formation of CIGS absorber, however vacuum-based technologies proved to be the best ones to obtain high efficiency CIGS solar cells. The variety of different growth methods is the result of ever-developing CIGS technology, searching more scalable and more efficient fabrication processes.

Front contact consists of buffer and window layers. In most of the thin film solar cells CdS is implemented as buffer layer. CdS is relatively wide band gap (2.4 eV) naturally n-type semiconductor and is electronically compatible with CIGS i.e. it forms II-type hetereojunction. Traditionally, 50-60 nm thick

CdS is deposited by chemical bath deposition method. Because Cd is considered hazardous and toxic metal it is listed in European Restriction of Hazardous Substances. Therefore scientists are searching for substitute for CdS buffer layer. Several compounds such as ZnS, ZnS(O,OH) and In_2S_3 have already showed promising results to replace CdS [18, 19, 20].

Window layer used in solar cells has to be transparent and conductive at the same time, therefore transparent-conductive oxides (TCO) are used. Mostly used materials for TCO are indium-tin oxide (ITO) and Al-doped zinc oxide (AZO). Sputtering method is usually applied for the formation of TCOs. Before deposition of TCO a thin intermediate layer of intrinsic ZnO is grown for couple of reasons: i) because it is highly resistive it prevents solar cells device from short-circuiting and ii) it protects CdS from damage caused during TCO sputtering.

Many companies have already started the production of CIGS modules and it is forecasted that capacity of the CIGS market will reach 2.3 GW in the several years [21]. However, CIGS market significantly lacks behind Si-based and in order to compete, CIGS technology must be more efficient, productive and cheaper. One of the relatively new emerging technologies as alternative to CIGS is CZTSe(S). Particular technology has a tremendous potential to reduce the production costs by using cheaper and earth-abundant materials. On the other hand, because of the immaturity of CZTSe(S) technology there is no commonly applied growth method as for example for CIGS, which would produce highly efficient CZTSe(S) solar cells. Therefore a huge increase of published papers concerning the formation of CZTSe(S) absorber by wide variety of growth methods has been observed for past several years. Thus, in the following section an overlook on CZTSe(S) development will be presented.

1.2 Development of $Cu_2ZnSnSe_4$ and Cu_2ZnSnS_4

The first synthesis of Cu_2ZnSnS_4 (CZTS) dates back to 1967. Swiss scientist R. Nitsche et al. have grown various types of chalcogenides ($A_2^I B^{II} C^{IV} X_4$) by iodine vapour transport, including CZTS [22]. At that time little was known about optical and physical properties of these materials. First, who rediscovered and understood the potential of CZTS for thin film solar cells were Japanese scientists Ito and Nakazawa [23]. They have synthesized Cu_2CdSnS_4 and Cu_2ZnSnS_4 layers by atom beam sputtering technique and measured physical and optical properties. It was determined that CZTS films posses very high absorption coefficient, $\alpha > 10^4$ cm^{-1} and determined band gap value was 1.45 eV. CZTS solar cell device was also fabricated by forming heterojunction with cadmium tin oxide and under illumination showed photovoltaic activity, V_{OC} = 165 mV.

The first "modern" CZTS solar cell has been fabricated by Katagiri et al. in 1996-1997 [24]. CZTS has been formed by sulphurization of electron beam deposited Cu/Sn/Zn stacked precursor under N_2+H_2S(5%) atmosphere. The corresponding CZTS thin film solar cells with architecture of SLG/Mo/CZTS/CdS/ZnO/Al provided a PCE of 0.66%.

This was a starting point for CZTS solar cell evolution where huge contribution was made by Nagaoka NCT. Year by year they implemented new approaches to the formation of CZTS, which resulted in higher CZTS solar cell efficiencies. One of the first key improvements were to reduce sulphurization time from 6-7 h to 1 h with increased temperature from 500 to 550 °C and substituting metallic Zn target with ZnS in evaporation process [25]. As a result, CZTS layers were more compact, with larger grains and showed an efficiency of 2.62%. Further improvements, such as achieving better base vacuum in the annealing chamber, changing deposition parameters for buffer layer and introducing sodium in the CZTS films resulted in increase of solar cell

efficiency up to 5.45 % [26]. Later on it was noted that soaking CZTS in deionized water for 10 min improved solar cell performance [27]. It was assumed that soaking in deionized water selectively removes metal oxide particles, therefore series resistance of the solar cell device was remarkably reduced. Adopting this method and optimizing growth parameters 6.77% efficiency was achieved for the CZTS based solar cells, which at that time was a world record.

Pioneer work of Nagaoka NCT showed a large potential of CZTSe(S) thin film technology, however there was still a lot of room for improvements. This was the reason why more and more scientists' groups joined in the development of CZTSe(S). As a consequence, a lot of papers were reported introducing to the new growth methods for CZTSe(S), more optimized sulphurization/selenization parameters. What is more, theoretical background of physical and optical properties as well as new insights and discoveries in achieving highly efficient CZTSe(S) solar cells have been reported.

In general the formation of CZTSe(S) can be divided into two main categories:

- **One step process**. In this case all constituents that is Cu, Zn, Sn, Se(S) are incorporated into precursor layer simultaneously. Co-evaporation and co-sputtering methods are usually applied for this approach. The best CIGS solar cells (21.7%) were achieved by this particular approach, however it is not the case for the CZTSe(S). The reason behind is associated with Zn and Sn volatility at higher temperatures, which makes deposition on heated substrates complicated. So far the best results for pure CZTSe solar cells (9.15%) have been achieved by NREL group using co-evaporation technique adapted from CIGS process [28].

- **Two-step processes.** In the first step precursor is formed by either vacuum or non-vacuum based growth methods. Recently, various low-cost and low temperature non-vacuum based growth methods have been applied to form either metallic or already chalcogenides incorporated precursors. In the second step the annealing of precursor in Se(S) containing atmosphere is conducted, so called selenization/ sulphurization. The highest CZTSe(S) solar cell efficiencies have been achieved by using particular approach [7].

It should be noted that in the major part of publications the formation of CZTSe(S) includes two steps. Herein we could further classify two-step processes into vacuum and non-vacuum (solution) based synthesis methods. Vacuum-based growth methods offer a good uniformity over large area, precise control of composition, good reproducibility and little or no contamination. On the other hand, equipment and maintenance is expensive in addition utilization of depositing materials generally is rather low. Advantages of solution based synthesis methods are cheap and rather simple equipment, inexpensive precursors, scalable on large substrates and high utilization of materials. In the early stage of kesterite development vacuum-based grow methods dominated and hold the world records for kesterite-based solar cell efficiency, see Fig. 1.2. The turning point was in 2010 when IBM reported CZTSSe solar cell efficiency of 9.66% where absorber was fabricated by ink-particle method [31]. At that time interest in CZTSe(S) drastically increased, which was associated with an increased CZTSe(S) efficiency (from 6.77% to 9.66%) and possibility to obtain high efficiency solar cells from solution based growth methods. Due to growing interest in the CZTSe(S) thin film technology various techniques and growth methods have been tested. Now a short introduction to technical aspect of the two-step process formation of CZTSe(S) will be given.

Composition. According to theoretical calculations a single phase region of CZTSe(S) is very narrow as opposite to CIGS [35, 36, 37]. This would suggest that only small deviation from stoichiometric composition is allowed in order to grow CZTSe(S) of pure phase. However, Nagaoka et al. grew single phase

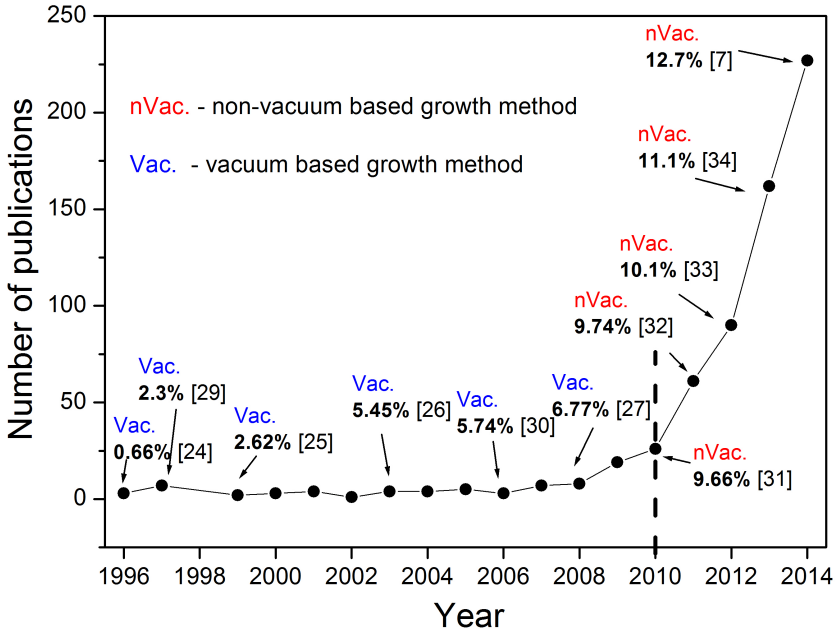

Figure 1.2: Evolution of number of publications related to kesterite topic. Research was done within sciencedirect journal database. Arrows and text indicate world record of kesterite-based solar cell PCE of particular year.

CZTSe and CZTS monocrystals with Zn-rich composition [38, 39]. No secondary phases were found by Raman or XRD methods. Nevertheless the neither growth methods nor precursor nature it was noticed that CZTSe(S) with Cu-poor and Zn-rich composition resulted in efficient solar cells, whereas with the stoichiometric one gave poor performance [40, 41, 42]. In general it has been shown that ratio of Cu/Zn+Sn in the range of 0.75 – 0.9 and Zn/Sn in the 1.10 – 1.3 is the optimum CZTSe(S) composition as far as solar cell efficiency is concerned [43, 44]. The particular suitable composition is thought to be related to defect formation in CZTSe(S). In Cu-poor and Zn-rich composition the formation of the V_{Cu} defects is promoted, whereas in stoichiometric

composition the lowest formation energy is of Cu_{Zn} antisite defects. V_{Cu} defect as in CIGS is a shallow acceptor, with transition energy of ~0.02 eV in contrast to Cu_{Zn} defect which is relatively deep - transition energy 0.11 eV [45]. Thus, at room temperature (0.025 eV) if V_{Cu} type defects are dominant all defects are ionized resulting in semiconducting CZTSe(S). On contrary, if Cu_{Zn} type defects are dominant only small part of defects are ionized resulting in highly resistive CZTSe(S) layer, which would lead to poor solar cell performance.

Precise control of metals can be challenging especially if evaporation techniques are used [46]. Authors concluded that evaporation at temperature higher than 350 °C leads to Zn and Sn losses. Volatile elements could be lost not only during evaporation/sputtering process but also during selenization/sulphurization.

Selenization/sulphurization. In order to fully convert metallic precursor to CZTSe(S) compound annealing at temperatures above 450 °C is necessary. Up to now it is not yet clear what is the exact reaction pathway of CZTSe(S) formation. Based on theoretical calculations, Hergert and Hock suggested the following reaction paths [47]:

$$Cu_2Se(S) + ZnSe(S) + SnSe(S)_2 \rightarrow Cu_2ZnSnSe_4 \quad (1.1)$$

or with intermediate ternary compound:

$$Cu_2Se(S) + SnSe(S)_2 \rightarrow Cu_2SnSe(S)_3 + ZnSe(S) \rightarrow Cu_2ZnSnSe(S)_4 \quad (1.2)$$

It was concluded that reaction (1.2) would be valid for synthesis routes in which chalcogenides form intermediately or are deposited directly, for example the annealing of stacked metallic precursor.

There are not many publications where experimental work is carried out to determine the reaction path of CZTSe(S). A detailed research by XRD and

Raman techniques was performed by A. Fairbrother el al. [48]. They investigated sulphurization mechanism of sputtered metallic precursor. According to their results firstly forms ZnS at 300 °C, then Cu-S binaries forms at 450 °C and SnS in parallel with CZTS starts to form at 500 °C. They suggested that solid-liquid-gas reaction is involved with an eutectic mixture of Cu_2S-SnS to the formation of CZTS, avoiding the formation of ternary Cu_2SnS_3 compound.

Another group, leading by Schurr using *in situ* XRD method has investigated the reaction path of electrochemically co-deposited Cu-Zn-Sn with thermally evaporated S on the top precursor [49]. They have prepared two types of precursors: Cu-rich (Cu/(Zn+Sn) ratio 1.5-1.6) and Cu-poor (Cu/(Zn+Sn) ratio 0.9-0.96). They concluded that reaction path depended on the composition of precursor. In the case of Cu-rich, binary sulphides form from Cu_3Sn and CuZn intermetallic alloys at 390 °C and 510 °C, respectively. At ~550 °C Cu_2SnS_3 starts to form from $Cu_{2-X}S$ and SnS_2 and the kesterite crystallization is completed by solid state reaction of Cu_2SnS_3 and ZnS at ~575 °C. As for Cu-poor case, binary sulphides form at lower temperature. Reaction path is similar to Cu-rich case except that intermetallic alloy Cu_6Sn_5 together with Cu_3Sn and CuZn is observed. They have concluded that the presence of Cu_6Sn_5 leads to a preferred formation of Cu_2SnS_3 via the reaction educts $Cu_{2-X}S$ and SnS_2 which were the decay products of Cu_4SnS_6.

Using the same *in situ* XRD method Yoo et al. studied the reaction path of co-sputtered metallic precursor with a capping layer of Se [50]. The as-deposited Cu-Zn-Sn precursors comprised of Sn, CuZn, Cu_5Zn_8 and CuSn phases. First, melting of Sn and Se occurred at 220-230 °C and then sluggish selenization of Sn and Zn in addition to the formation of intermetallic compounds up to 415 °C were observed. At 415 °C remaining intermetallic alloys melt, triggering crystallization of ZnSe and SnSe together with $Cu_XSn_YSe_Z$ and/or Cu_2SnSe_4 phases which later by increasing temperature converts to

Cu_2SnSe_3. They did not detect Cu selenides and it was suggested that copper was bound to intermetallic alloys up to 415 °C and then reacted to form Cu_2SnSe_3. Above 415 °C Cu_2SnSe_3 compound reacts with ZnSe to form quaternary $Cu_2ZnSnSe_4$.

A very similar work, reported by Wibowo et al. was carried out on the formation of CZTSe from stacked metallic precursor [51]. Various stack orders were prepared to thoroughly investigate metallic phase dynamics as well as binary phase formation in the temperature range of RT-550 °C by XRD and differential scanning calorimetry (DSC) techniques. The as-deposited Cu-Zn-Sn precursor contained metallic Sn and Cu as well as intermetallic compounds Cu_6Sn_5 and Cu_5Zn_8. According to their results, no binary selenides form up to 320 °C. They suggested that intermetallic compounds such as CuZn, Cu_3Sn and $Cu_{41}Sn_{11}$, which forms during annealing up to 300 °C, form a passivating layer that prevents selenization below 320 °C. By further increasing temperature the gradual formation of ZnSe from zinc containing intermetallic compounds occurs. At 450 °C α-brass and $Cu_{41}Sn_{11}$ directly react with liquid Se and form ZnSe, Cu_2Se and SnSe respectively. Above 530 °C the formation of ternary Cu_2SnSe_3 occurs by alloying Cu_2Se, SnSe and Se. Solid state reaction of $Cu_2ZnSnSe_4$ is completed by final step where Cu_2SnSe_3 reacts with ZnSe from 530 °C.

The above mentioned examples illustrate that there is no universal mechanism for reaction path of the CZTSe(S) formation and that it is dependent on the nature of precursor, composition and sulphurization/selenization conditions.

During selenization/sulphurization step atmosphere control is very important. Due to volatile metals as well as volatile binary sulfides (SnSe, SnS) decomposition of CZTSe(S) may occur at high temperatures [52]:

$$Cu_2ZnSnSe(S)_4 \leftrightarrow Cu_2Se(S) + ZnSe(S) + SnSe(S)\,(g) + Se(S)\,(g) \quad (1.3)$$

To prevent decomposition and Sn loss authors introduced SnS_2 in the graphite box in the form of powder. Their results confirmed the validity of decomposition reaction (1.3) and it was concluded that incorporating excess of Sn and Se(S) in the annealing environment significantly improves solar cells efficiency and reproducibility.

Another option of preventing decomposition reaction was to deposit a capping layer of $SnSe_2$ on top of CZTSe which was suggested by Redinger group [53]. By doing this they have achieved above 5% efficiency solar cells and significantly reduced series resistance.

What is more, it was also proposed that during annealing step, CZTSe(S) can react with Mo inducing phase segregation at the Mo/CZTSe(S) interface [54, 55]. The proposed decomposition reactions for pure CZTSe [54] and CZTS [55] compounds are slightly different because of different annealing approaches, however general decomposition reaction could be written as:

$$2Cu_2ZnSnSe(S)_4 + Mo \rightarrow 2Cu_2Se(S) + 2ZnSe(S) + 2SnSe(S) + MoSe(S)_2 \quad (1.4)$$

It shows that binary phases segregate at the back contact of solar cell significantly reducing solar cell performance. To overcome this problem scientists used barrier layers, ZnO [54, 56], TiN [57, 58] to prevent Mo selenization/sulphurization.

Secondary phases. The aforementioned facts, for example growth with non-stoichiometric composition, decomposition reactions induced by the lack of volatile educts or CZTSe(S) reaction with Mo almost always will result in the formation of secondary phases. For example, in the Cu-poor and Zn-rich growth conditions ZnSe(S) forms inevitably. It was noticed that ZnS segregated at the Mo/CZTS interface significantly increases series resistance [59]. Other research group has found out that ZnSe formed at the surface of

the absorber blocks current to the front contact thus decreases j_{SC} [60]. Because $Cu_2SnSe(S)_3$ E_g is lower than CZTSe(S), the formation of latter secondary phase reduces solar cell V_{OC} [61]. Due to conductive nature of copper and tin sulphides/selenides existence of latter phases create shunt paths therefore shunt resistance of solar cell is significantly reduced.

It is evident that secondary phases are detrimental to the CZTSe(S) solar cell performance and their formation must be minimized. One of the ways to control it is to remove secondary phase by chemical etching.

Firstly, KCN etching adapted from CIGS was implemented to remove oxides and copper sulphides/selenides from the surface. It worked perfectly for CIGS and improved performance of CIGS solar cells, however it was not the same for CZTSe(S). Timmo et al. has tested five different etching solutions for CZT(S,Se) monograins [62]. They have found out that aqueous 10 % HCl preferably removes Sn and S(Se), whereas KCN-etching removes Cu, Sn and S(Se). Other tested solutions NH_4-OH have been found out to remove selectively Cu and S(Se) and etching in Br_2-MeOH solution have resulted in Sn-rich CZT(S,Se) surface. The combination of several etching solutions has significantly improved V_{OC} of CZT(Se,S) monograins solar cells – from 300 mV to 575 mV.

Because commonly employed growth composition of CZTSe(S) is Cu-poor and Zn-rich, ZnSe(S) is the most probable secondary phase, whereas copper sulphides/selenides are less expected. In order to selectively remove ZnS secondary phase Fairbrother et al. tested HCl etching at elevated temperature (75 °C) and demonstrated an efficiency increase from 2.7% to 5.2% of CZTS solar cells mainly due to increased j_{SC} and reduced R_s [63]. An elegant approach for selective etching of ZnSe was proposed by López-Marino et al. [64]. They used two step etching route firstly by oxidizing ZnSe in $KMnO_4$ + H_2SO_4 solution, followed by removal of elemental selenium in Na_2S solution. A substantial increase in solar cell efficiency from 3.6% to 5% was observed.

It should be mentioned that location of secondary phases i.e. if it form on the surface, in the bulk or at the interface of CZTSe(S) and back contact, are also important and affect device performance differently. Hsu et al. investigated the Zn excess in CZTSe and concluded that ZnSe formed on the surface of CZTSe is detrimental to device performance, whereas ZnSe located at the back does not affect solar cell efficiency [65].

In summary, it is obvious that $Cu_2ZnSnSe(S)_4$ is a complex system and to synthesize (obtain) high quality single phase CZTSe(S) film is a challenging task. The highest kesterite based solar cell efficiency (12.7%) is well beyond the 21.7% achieved for CIGS technology. It indicates that there are a lot of technological issues that has to be addressed and optimized in order to obtain highly efficient CZTSe(S) solar cells.

The fact that the best solar cell CZTSe(S) absorber was synthesized via spin-coated solution + particle method shows a huge potential for low-cost vacuum-free growth methods to be implemented in the formation of CZTSe(S). Concerning other non-vacuum growth methods, for example spray pyrolysis [66], monograins [67] and electrochemical deposition [68] have also demonstrated efficient CZTSe(S) solar cells. Among the mentioned solution-based growth methods electrodeposition is an attractive approach because of very high material utilization (~90%), deposition is easily scalable on large substrates, inexpensive precursors and maturity of technology. Galvanization of metals with Sn and Zn has been used in industry for many years, meanwhile Cu electrodeposition is well-established in the electronics. Recently the number of papers, regarding formation of CZTSe(S) from electrochemically deposited precursors has substantially increased. Because electrochemical deposition is the main instrument for forming metallic precursors in this study, a more detail overlook on the synthesis of CZTSe(S) absorber from electrodeposited precursors will be given in the following subsection.

1.3 Molybdenum substrate

Just before starting literature review about electrochemical deposition of Cu-Zn-Sn precursors, properties of the most commonly used substrate – Mo will be addressed. Mo serves as a back contact for CZTSe(S) solar cells thus it has to be well adherent to the glass and conductive to minimize series resistance. When electrodeposition method is applied, requirement for adherence of Mo to the glass is even more important. The reason is because during electrodeposition of metals at negative reduction potential, hydrogen evolution occurs, which in turn can induce Mo layer to peel off.

The most commonly applied fabrication method for thin Mo film is magnetron sputtering [69 – 76]. It was noticed that single layer Mo films are not well adherent and conductive at the same time. Among all deposition parameters working Ar pressure during sputtering has the largest impact on Mo structure and physical properties. According to the literature Mo films deposited at high Ar pressure (5-20 mTorr) have columnar grains with porous microstructure and are very well adherent to the glass, however films exhibit high resistivity [69, 70]. On the other hand, Mo films sputtered under low Ar pressure (< 5 mTorr) are densely packed with relatively large grains and conductivity is close to the value of the bulk Mo, however films are under high compressive stress and are poorly adhered to the glass. To overcome the latter problem scientists fabricated Mo thin films consisting of two or more layers deposited under different Ar pressure [70 - 73]. By finding optimum sputtering condition for Mo layers they have successfully synthesized bi-layer Mo films, which were good-adherent to the glass and possessed low resistivity.

Another option to obtain well-adherent and conductive Mo films is to use RF magnetron sputtering method. The influence of Ar pressure on film resistivity and adhesion is much less pronounced than in DC sputtering regime

[74, 75]. However, CIGS solar cells prepared on RF sputtered Mo substrate showed lower power conversion efficiency in comparison to the same cells fabricated on DC sputtered Mo film [74].

Another important property of Mo is that during selenization chemical activity of Mo is dependent on its microstructure. Mo layers, deposited at low Ar pressure are readily selenized, whereas only little part of Mo grown at high pressure is selenized [76]. The higher chemical activity of Mo sputtered at low pressure with Se was also observed by Kapur et al. [77]. They concluded that residual stresses in the Mo layer enhance Se reaction rate with Mo.

In conclusion, in order to meet the requirements for back contact and serve as high quality electrode during electrochemical deposition, appropriate sputtering condition have to be chosen for the formation of multi-layer Mo film.

1.4 Electrochemical deposition of Cu-Zn-Sn precursor

Due to inexpensive equipment, high material utilization and low-cost source materials electrochemical deposition method is an attractive approach for thin metal film deposition. The latter deposition method becomes especially advantageous for fabrication of Cu-Zn-Sn precursors. Electrodeposition of each metal has been studied for many years and is already well-established in industry. Furthermore, electrodeposition was successfully applied in other thin film solar cell technologies: CdTe [78] and CIGS [79]. First attempts to form CZT precursor by electrodeposition for CZTSe(S) formation were conducted in 2008-2009. Soon it became apparent that there are two major approaches for the formation of CZT precursors by electrochemical deposition method: i) stacked (sequential) layer deposition and ii) co-deposition of metals or all constituents. Both approaches have their pros and cons, which are summarized in table 1.1

Table 1.1: The comparison of different electrodeposition approaches for CZT precursor formation.

Approach	Advantages	Disadvantages
Co-deposition	Single bath All constituents can be deposited in one-step process Low material consumption Less quantity of waste water	Complex chemistry Fast Sn^{2+} oxidation in the presence of other metals ions Need of accurate control of ion concentration Large discrepancy between metals' standard redox potentials Limited control of element gradient
Stacked layer deposition	Possibility to exploit element gradient Higher quality metal films can be obtained Possibility to use galvanostatic deposition Stable electrolytes	Multiple baths Requirement of rinsing after each deposition More difficult to implement in industry Relatively high material consumption

Major part of this work is dedicated to the investigation of CZTSe formation from electrochemically co-deposited Cu-Zn-Sn precursor. Concerning sequential layer deposition only the proof of concept of implementing electrochemical flow cell for deposition of stacked metal layers is shown. Therefore literature review will be focused more on CZTSe prepared from electrochemically co-deposited CZT precursors.

1.4.1 CZTSe(S) from co-deposited Cu-Zn-Sn precursor

First attempts to form kesterite absorber from electrochemically co-deposited CZT precursor were published in 2009. Ennaoui et al. published study, where CZT precursor was electrochemically co-deposited using sodium-pyrophosphate as supporting electrolyte with dissolved Cu, Sn and Zn salts,

additives and complexing agents [80]. Duration of electrochemical deposition was 20 min. Circulation pumps and sprayer system were used to provide homogenous hydrodynamic conditions. Sulphurization was performed under gas mixture of Ar+H_2S (5%) for 120 min at 550 °C. The whole annealing process including heating and cool-down steps took approximately 8 h. SEM micrograph of cleaved CZT precursor cross-section revealed that film comprised compact grains of columnar structure which extended through whole film thickness. Solar cell cross-section images also revealed that large voids and local delamination occurred at the Mo/CZTS interface. Measurements of solar cell parameters showed highest power conversion efficiency of 3.6% after light soaking, high series resistance and low FF value, which according to the authors, were caused by the formation of ZnS at the Mo/CZTS interface.

Araki et al. co-deposited Cu-Zn-Sn film in classical three-electrode cell from solution, containing 20 mM $CuSO_4$, 200 mM $ZnSO_4$, 10 mM $SnCl_2$ and 500 mM tri-sodium citrate [81]. Deposition was carried out potentiostatically (-1.1 – -1.2 V vs Ag/AgCl/$KCl_{sat.}$ reference electrode) for 20 min and no stirring was applied. CZT was sulphurized in glass container with sulphur powder inside, under 1 bar N_2 gas at 580-600 °C for 120 min. Pillar-shaped grains were observed in the CZT morphology, similar to the ones observed by Ennaoui [80]. Sample annealed at 600 °C comprised larger grains in comparison to sample annealed at 580 °C and XRD results confirmed the formation of single phase Cu_2ZnSnS_4. Solar cell prepared from precursor annealed at 600 °C demonstrated 3.16% PCE.

It should be noted that in the major part of publications related to electrochemical co-deposition of Cu-Zn-Sn precursor solution stirring was not provided [81 – 87]. In the classical assembly of three-electrode cell without solution agitation a preferential electrodeposition occurs at the bottom as well as at the edges of the working electrode, resulting in non-uniform layer

thickness and composition. Even though stirring was not provided solar cells fabricated from electrochemically co-deposited precursors were relatively efficient [81, 82, 83, 87]. For example, Zhang et al. in order to form homogeneous and compact Cu-Zn-Sn layer without solution agitation, used strongly diluted electrolyte solution [82]. CZT layers were deposited from citrate-based electrolyte which contained 3 mM $CuSO_4$, 2 mM $ZnSO_4$ and 3 mM $SnSO_4$ at -1.3 V vs Ag/AgCl/$KCl_{sat.}$ reference electrode. To achieve desired thickness of the CZT film, deposition was conducted for 60 min at elevated temperature + 65 °C without stirring. Authors stated that implementing very low concentrations of metal ions improved film density and compactness, however prolonged duration of deposition was required to achieve thick enough layers. Annealing was performed at 500 °C under 30 Torr Ar pressure in graphite container with selenium particles inside and different heating rates: i) very slow *ca.* 5 °C/min (CFA) and ii) rapid ca. 100 °C/s (RTA). Phase investigation of as-deposited CZT precursor revealed that it contained Sn, CuZn, CuSn, Cu_5Zn_8 and Cu phases, however because of overlapping diffraction peaks and the lack of XRD resolution intermetallic compounds were not unambiguously identified. Clusters comprised of nanometer-size grains were observed in the SEM surface morphology of as-deposited CZT films. HR-SEM image revealed that clusters are not fully coalesced and there is no cross-section image presented, which would enable to estimate film porosity and adhesion to Mo. A well-grained, single phase CZTSe layer has been obtained by RTA approach. Champion solar cell, prepared from particular absorber showed 4.5 % PCE and extremely high j_{SC} – 38.81 mA/cm^2. It should be mentioned that in this study a comparison between RTA and CFA approaches is not entirely adequate, because heating rate, annealing duration and cool-down steps for CFA were excessively long and as a result all Se source drains out causing the decomposition of CZTSe. This could be the reason why they obtained CZTSe of poor crystal quality, layer comprised of

small grains and secondary phases were detected in samples selenized by CFA approach.

Another posing issue regarding electrochemical co-deposition of Cu-Zn-Sn layers is the duration of deposition. In order to acquire dense, compact CZT films, scientists have used low metal ion concentrations, consequently long (45-120 min) deposition time is required to deposit film with appropriate thickness [82, 84]. For instance, Zhu et al. co-deposited CZT precursor in citrate-based electrolyte containing dissolved three metal salts [84]. Deposition was carried out without stirring for 120 min at -1.2 – -1.25 V vs SCE reference electrode to achieve 500 nm thick CZT layer. Before selenization CZT films were preheated in vacuum at 250 °C. Selenization took place in two-zone quartz reactor with saturated selenium atmosphere, where the source of selenium was set to 380 °C and the substrate temperature varied from 300 to 550 °C. After preheating of co-deposited CZT precursor initial phase such as Zn, Sn, Cu_6Sn_5, $CuZn_2$ converted to Cu_6Sn_5, Cu_3Sn and CuZn as was confirmed by XRD method. Authors suggested that fully alloying CZT precursor leads to better quality of CZTSe. Unfortunately, no SEM images of morphology or cross-section of either as-deposited or preheated CZT precursor were presented. Optimal temperature for selenization was found to be 550 °C because ZnSe phase was no more detected at this temperature. SEM micrograph of CZTSe solar cell cross-section revealed that layer comprised of large well-defined micrometer-size grains with intermediate layer of smaller irregular shape grains at the Mo/CZTSe interface. Very much alike structure was also observed in the samples, investigated in this thesis. Despite the large and high quality CZTSe grains, solar cell performance was relatively low, demonstrated only 1.7 % PCE, mainly due to very low V_{OC} and FF.

Several solutions to decrease electrochemical co-deposition time could be implemented: i) to increase metal ion concentration in the solution ii) to increase deposition efficiency by providing solution stirring. Albeit higher (10

– 330 mM) concentration of metal ions was added to the electrolyte, deposition still took 10-20 min without solution agitation [83, 85, 86, 87]. Liu et al. in their work have co-electroplated CZT precursor using higher ion concentration electrolyte solution, though deposition duration still was relatively long [83]. Electrolyte contained 35 mM $CuSO_4$, 20 mM $SnSO_4$ and 200 mM $ZnSO_4$ and two complexing agents – 0.1 M potassium sodium tartrate and 0.5 M sodium citrate. CZT precursor was deposited in classical three-electrode electrochemical cell without stirring at -1.2 V vs SCE reference electrode for 10 min, pH adjusted to 6 by NaOH and temperature was held at +25 °C with a help of thermostat. CZT films were annealed in two-zone furnace, where sulphur held at 200 °C and substrate at 580 °C for 60 min. In particular study two approaches of controlling pressure in the tube were tested: i) a flux of Ar gas along the tube was introduced at atmospheric pressure (open-zone) and ii) static pressure of Ar and sulphur gas mixture was kept at 50 kPa (close-zone). SEM, Raman and XRD results showed that large well-defined, high crystalline quality grains have formed in the close-zone conditions. Solar cell prepared from absorbers formed with close and open zone conditions showed 3.62 % and 2.72 % PCE, respectively. It should be noted that high V_{OC} value of 686 mV have been demonstrated. Authors concluded that high quality grains and better phase purity achieved in closed-zone condition have led to the better solar cell performance.

The second option of increasing deposition rate was implemented in the Chassaing et al. work [88]. They have introduced rotating disc electrode in order to increase the uniformity of the films. Therefore deposition from 5 mM of each metal sulphates, 50 mM K_2SO_4 and 50 mM of sodium citrate containing electrolyte took only ~5 min. Deposition was carried out at 25 °C, solutions' pH adjusted to 4.75 and deposition potential was -1.9 V vs MSE reference electrode. Because of the high overpotential a dendritic growth was observed in the CZT films, however according to authors after selenization

dendritic morphology was markedly reduced. Selenization was performed in Se atmosphere at 530 °C for 15 min with a heating rate of 40 °C /min. Little details are given about structural properties of CZTSe films, nevertheless champion solar cell prepared from particular absorbers has shown 5.8 % PCE.

1.4.2 CZTSe(S) from sequentially deposited Cu-Zn-Sn precursor

A pioneering work on stacked layer electrodeposition was conducted by Scragg et al. In 2008 they published paper, where photoelectrochemical investigation was carried out on Cu_2ZnSnS_4 film, prepared from sequentially electrodeposited Cu, Sn, Zn layers [89]. For the deposition of Cu and Sn electrolytes containing NaOH, sorbitol, $CuCl_2$ and $SnCl_2$ were chosen, whereas Zn was deposited from $ZnCl_2$ solution containing hydrion buffer. Layers were sequentially deposited at room temperature without stirring in separate 3—electrode cells. Sulphurization was performed in graphite container, which was inserted into a tube furnace filled with 1 bar pressure Ar gas at 550 °C for 120 min. Island-like growth of Sn on Cu layer was observed by SEM. Visually after sulfurization CZTS films appeared rough and dark grey colour. Photoelectrochemical measurements revealed that diffusion length of carriers is very short and space charge region width is narrow 0.2 ± 0.1 μm in CZTS. Because of the latter mentioned observation, carrier collection in CZTS is very ineffective. In order to improve the quality of CZTS layers, Scragg et al. have changed annealing conditions, by introducing H_2S flow instead of S powder in the tube furnace. As a result, CZTS films were composed of larger grains, lower defect density and better crystalline quality in general. Albeit crystal quality of CZTS was increased, films suffered from decreased integrity exposing large areas of MoS_2 and smaller particles of Zn and Sn sulphides.

A substantial improvement of uniformity by introducing rotating disc electrode and changing electrolyte composition has been achieved by the

same group [90]. Sorbitol Sn deposition bath was changed to methanesulfonic acid electrolyte, which resulted in change of film morphology from island-like to compact, crack-free continuous layer. The order of the metallic stack was also changed from Cu/Sn/Zn to Cu/Sn/Cu/Zn. The precursor was placed in the graphite container with 100 mg of elemental S inside. Annealing was performed in tube furnace under 0.5 bar pressure of N_2+10% H_2 gas at 575 °C for 120 min. An improved uniformity of CZT precursor has led to uniform formation of CZTS absorber. The maximum 3.2 % efficiency was obtained for CZTS solar cells. A very detailed research of particular electrochemical deposition and sulphurization of Cu, Sn, Zn layers can be found in [91].

Up to now the best performing kesterite-based solar cells formed by electrodeposition method in general were achieved from stacked layer approach [68, 92, 93]. Absorber of 8% efficiency CZTS solar cell was formed by electrochemically depositing Cu, Sn and Zn layers which afterwards were preheated at 310 °C for 40 – 150 min in the evacuated borosilicate glass ampoule [68]. Cu, Sn and Zn were electrodeposited potentiostatically at -0.4, -0.54 and -1.2 V vs Ag/AgCl/$KCl_{sat.}$ reference electrode, respectively. Citrate-based solution was used for deposition of Cu, whereas Sn was deposited from methanesulfonic electrolyte containing empigen BB detergent as an additive. Zn was deposited from solution containing zinc and potassium sulphates at pH 3. These deposition conditions are similar to the ones reported in [90], although no details are given about electrochemical cell design or solution agitation. Sulphurization of preheated precursor was performed again in evacuated borosilicate glass ampoule with 5-10 mg of S powder at 590 °C for 10 min. A significant cracks as well as ZnS segregation was observed at the Mo/CZTS interface, nevertheless high values of FF and V_{OC} have been achieved 72% and 650 mV, respectively. The best results were achieved with Cu/Sn/Zn precursors preheated for 150 min and authors concluded that the reduced CZTS film roughness from 0.67 μm to 0.15 μm resulted in the

smoother CdS-CZTS interface, which in turn improved solar cell performance. However, no morphology investigation of as-deposited or preheated Cu/Sn/Zn precursor has been presented.

A more industry-oriented approach for stacked layer electrodeposition has been suggested by Ahmed et al. They have successfully fabricated CZTSe and CZTS solar cells exceeding 7 % efficiency [92, 93] on 15 x 15 cm^2 area substrates. The stack order of electrodeposited CZT was Mo/Cu/Sn/Zn or Mo/Cu/Zn/Sn. Metals were deposited from commercial electrolytes except for a Zn, which was deposited from home-made solution. A galvanostatic deposition (j = 10 – 20 mA/cm^2) was applied to obtain thin metal films. It should be noted that electrodeposition took place in large volume paddle cell and a co-planar deflector electrode was implemented to increase the uniformity of deposits. Before sulphurization and selenization CZT precursors were preheated at 350-360 °C for 30 min to promote intermixing of elements. For champion CZTS solar cell sulphurization was conducted in sealed quartz ampoule with 2-5 mg of S under nitrogen atmosphere at 585 °C for 12 min, whereas selenization was performed at 585 °C for 7 min with 40-45 mg of Se in the quartz ampoule as well. Solar cell parameters V_{OC}, j_{SC}, FF, η of champion CZTS solar cell were 567 mV, 22 mA/cm^2, 58.1 %, 7.3 %, respectively, whereas for CZTSe solar cell 369 mV, 32.4 mA/cm^2, 58.5 %, 7 %, accordingly.

It is clear that preheating step of sequentially deposited precursor is necessary to obtain highly efficient CZTSe(S) solar cells. The influence of preheating step on Cu/Sn/Zn morphology and phase formation was investigated by Ikeda et al. [94]. Using conventional three-electrode cell they have electrodeposited Cu, Sn, Zn layers under potentiostatical control. Preheating was done in evacuated Pyrex ampoule at 350 °C for 20 – 40 min. After preheating step CZT precursors contained Cu_6Sn_5, Cu_3Sn, Cu_5Zn_8 and Sn phases as was confirmed by XRD. Morphology of as-deposited and preheated

CZT film was found to be island-like because of the inhomogeneous electrodeposition of Sn layer and film morphology was not significantly affected after preliminary annealing. The best performing CZTS solar cell was fabricated from Cu/Sn/Zn precursor preheated for 20 min and demonstrated 5.6% PCE, whereas for sample preheated for 40 min PCE was 2.6%. These results are rather contradictive to the ones mentioned before [68]. Disregarding small preheating temperature difference, long preheating duration of 150 min was required to achieve 8% efficient solar cell, meanwhile in the study of consideration – preheating for 20 min gave best solar cell parameters. In both cases electrodeposition and sulphurization conditions were almost the same. This indicates that preheating step has a positive effect on the formation of CZTSe(S), however it is not yet clear how and why.

Influence of stacking order of CZT precursor on the formation of CZTSe(S) layer is not clearly identified. The most commonly used sequence of metal deposition is Cu/Sn/Zn, however for example, Ahmed et al. obtained same good results using both stacking orders Cu/Zn/Sn and Cu/Sn/Zn [92]. Mkawi et al. found out that among tested stacking orders of Sn/Cu/Zn/Cu, Zn/Cu/Sn/Cu, Cu/Zn/Cu/Sn and Cu/Sn/Cu/Zn the latter gave the best results as far as structural properties and solar cell efficiency is concerned [96]. Generally speaking stacking order does not have a significant effect on the CZTSe(S) formation, especially if preheating step is applied, although Cu should be deposited as a first layer because of best adherence properties to Mo among other metals.

The truly one-step deposition, where in addition to metal deposition chalcogenide is incorporated, have been reported as well [96-103]. Because this approach is not used in this work, only general remarks will be given. Notably, there are much more publication regarding CZTS one-step deposition [98-103] in contrast to CZTSe [96, 97]. The most used solution composition is very similar to co-deposition of metals except that for the source of S, mainly

sodium-thiosulphate is added. As for the source of Se different compounds have been used, for example SeO_2 [96] and Na_2SeO_3 [97]. Traditionally, films deposited at one-step approach suffer from poor morphology [96, 98, 99], however it was improved by applying pulse electrodeposition [100, 101, 102]. So far the best performing solar cell, prepared from co-electroplated Cu-Zn-Sn-S precursor have been achieved by Jiang et al. [103]. They have electrochemically co-deposited CZTS precursor from electrolyte containing sodium-citrate, dissolved metal salts and sodium thiosulphate at -1.15 V vs $Ag/AgCl/KCl_{sat.}$ for 30 min. The annealing of precursor was performed at 590 °C for 15 min with a heating rate of 20 °C/min. SEM images clearly showed that after sulphurization CZTS film comprised of two layers: compact one, with large CZTS grains and particulate-like containing stacking faults and secondary phases. However, CZTS solar cell demonstrated 5.5 % PCE and relatively high j_{SC} (18.7 mA/cm^2) as for pure sulphur based absorber.

2 Experiment description

All experimental details which were implemented in this study will be given in this chapter. Firstly, Mo sputtering conditions are introduced. Then two approaches of metallic precursor fabrication are described: electrochemical co-deposition and stacked layer deposition. Furthermore, flow cell design and operation is presented. Lastly, characterization techniques used in this work are briefly described.

2.1 Molybdenum sputtering

Mo coated soda lime glass substrates were prepared by DC magnetron sputtering method. Mo was sputtered using PVD225 sputtering system, distance between target and substrate was 270 ± 2 mm. Mo plate with purity of 99.95% was used as a target. The substrate was rotated at 15 rpm to improve the uniformity of the deposited Mo films. Glass substrate surface was cleaned with alcohol, acetone followed by plasma etching at the end. Base pressure in the chamber was 10^{-4} mTorr. Working Ar pressure was varied in the range of 1.5 – 20 mTorr. Unless otherwise noted soda-lime glass substrate was kept at room temperature. The sputtering power varied in the range of 200 – 400 W depending on the working pressure.

2.2 Electrochemical co-deposition of Cu-Zn-Sn precursor

Electrolyte solution for co-deposition comprised of $CuSO_4 \cdot 5H_2O$ (purity 99%), $ZnSO_4 \cdot 7H_2O$ (purity 99%), $SnSO_4$ (purity 99%) and sodium citrate (purity 99%) salts dissolved in deionized water. As an antioxidant for Sn^{2+} ions hydroquinone was used in the electrolyte. The pH of solution was adjusted to

5.75 with H_2SO_4 of spectroscopic purity. Electrodeposition was performed in classical three electrode electrochemical cell and solution agitation was provided with magnetic stirrer. As a working electrode soda-lime glass coated with a molybdenum layer was used. Working electrode dimensions were 1x2.5 cm^2 with an active surface area of 1-1.5 cm^2. Counter electrode was platinum plate (purity 99.999%) with much larger dimensions than those of working electrode. Saturated $Ag/AgCl/KCl_{sat.}$ electrode (+0.197 V vs NHE) was used as a reference electrode which was introduced to vicinity of the working electrode through Luggin capillary. Before deposition Mo substrate was processed by three different Mo surface preparations methods, which are described in the §4.2.1. Electrolyte temperature was kept at constant value (+20 ±1 °C) with a help of thermostat. Before deposition oxygen was purged off by bubbling electrolyte with Ar gas (purity 99.9995%) for 20 min. CZT films were deposited under potentiostatic control using PI-50-1.1 potentiostat. The deposition potential for CZT films varied in the rage of -1.1 – -1.4 V vs $Ag/AgCl/KCl_{sat.}$.

2.3 Stacked CZT precursor layer deposition with flow cell

Schematic representation of flow cell is depicted in Fig. 2.1. Flow cell comprises of two parts i) bottom, where working electrode of 1x2.5 cm^2 can be inserted and connected to the external wires and ii) top, where electrolyte flows and auxiliary electrode is implemented. Pt wire, which is located at the bottom part of the flow cell (see Fig. 2.1) is used as a reference electrode. Pt plate, with dimensions larger than those of the working electrode is used as auxiliary electrode. The volume of the chamber where electrolyte flows is 11.25 cm^3.

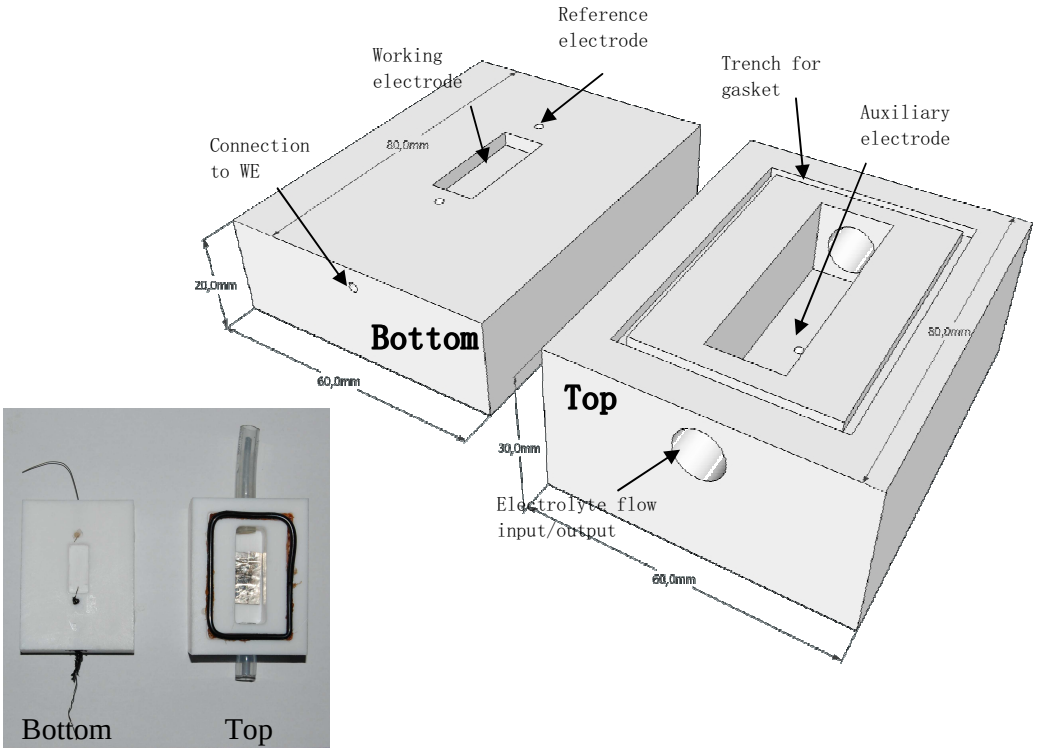

Figure 2.1: Graphic design of electrochemical flow cell and photograph of actual cell (left corner).

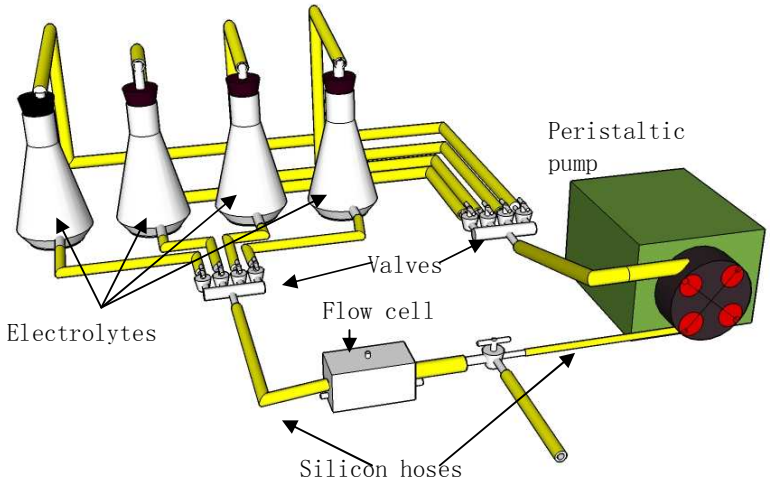

Figure 2.2: Electrochemical deposition setup with flow cell for sequential electrodeposition of Cu, Sn and Zn layers.

Appropriate dimensions were chosen to mimic channel-shape chamber and to produce laminar flow of electrolyte. The full working flow cell is achieved by joining bottom part with upside-down top part and tightening them with screws. Rubber gaskets insure there is no electrolyte leakage. Electrolyte flow cycle is organized using silicon hoses and peristaltic pump. Schematic diagram of overall flow cell system is depicted in Fig. 2.2. Three modified flasks are used for electrodeposition of Cu, Sn and Zn, whereas fourth one is used for rising with deionized water.

Particular electrochemical deposition system using flow cell in comparison to classical one has several advantages:

- Uniform and laminar electrolyte flow can be achieved near working electrode surface as a consequence more uniform in thickness and composition layers can be deposited.
- Minimum exposure of the deposited layers to the air.
- Easily scalable on large substrates and deposition process can be fully automated.

Among tested electrolytes the most suitable solutions used for stacked layer deposition with flow cell were as follows:

Cu: 0.075 M $CuSO_4 \cdot 5H_2O$ + 0.25 M $Na_3C_6H_5O_7 \cdot 2H_2O$, pH – 5.6

Sn: 0.05 M $SnSO_4$ + 1 M CH_3SO_3H (MSA) + 0.8 ml TritonX-100, pH ~1

Zn (Commercial): $ZnCl_2$ + KCl + H_3BO_3 + additives, pH – 5.5

Other electrolytes for Sn and Zn were also tested and are described in §4.3.2 and §4.3.3. Layers were deposited both potentiostatically and galvanostatically and summary of deposition parameters are listed in the table 2.1.

Table 2.1: Deposition parameters for stacked layer deposition.

Layer	E *, V	j, mA/cm^2	Flow rate, ml/min	Time, s
Cu	-0.94 -1.0	-	200-400	45-90
Sn	-0.93-0.95	-	250-420	20-40
Zn	-	2.5-30	200-400	15-150

* potentials are given vs Pt wire reference electrode.

2.4 Preliminary annealing and selenization

Preliminary annealing and selenization were performed in three-zone tube furnace, equipped with diffusion and turbo pumps. The maximum base vacuum was 10^{-4} mbar. Temperature was controlled via computer software. Temperature ramp rate was fixed at 20 °C/min unless stated otherwise. Before selenization CZT precursors were preliminary annealed in vacuum, Ar, H_2 or Ar+H_2 atmospheres at 200 – 350 °C for 10 – 120 min. Semi insulating graphite box with total volume of ~23 cm^3 was used for selenization of CZT precursors. Elemental Se and Sn powders, present in the graphite box, acted as Se and Sn sources. Selenization temperature was in a range of 450 – 560 °C and annealing took from 10 to 30 min. All selenizations were performed under Ar atmosphere either in flow or static regimes. Flux of 1 mbar was achieved by adjusting inlet of Ar gas and opening pump valves in flow regime, whereas in other case static atmospheric pressure of Ar was introduced in the furnace tube.

2.5 Solar cell fabrication

Solar cell structure was as follows: Mo/CZTSe/CdS/i-ZnO/ITO. After the selenization of CZT precursors etching was performed in order to remove

ZnSe secondary phase, as it is the most probable secondary phase in CZTSe with Zn-rich and Cu-poor composition. Etching consisted of two steps: i) films were immersed in $KMnO_4$ + H_2SO_4 solution for 30 s to oxidize ZnSe ii) samples were rinsed with deionized water and then dipped in Na_2S solution for 60 s to remove elemental Se. Finally, samples were rinsed with miliQ water and dried out under nitrogen flow. For depositing CdS buffer layer chemical bath deposition method was implemented. Firstly four solutions were prepared separately i.e. $CdCl_2$, NH_4Cl, NH_4OH, CH_4N_2S (thiourea). Then they were heated up to 70 °C and added up in the following order: $CdCl_2$, NH_4Cl, NH_4OH and lastly several drops of thiourea. Deposition took around 400-500 s to achieve 50-60 nm thick CdS layer. After CdS deposition residues on the surface of the samples were cleaned, then rinsed with miliQ water and dried under nitrogen flow. Window layer was formed by sputtering 50 nm thick intrinsic zinc oxide (i-ZnO) and 300-400 nm thick indium tin oxide (ITO). Both oxides were sputtered with CT100 Alliance Concepts magnetron in separate chambers. Sputtering conditions for i-ZnO were 120 W, 10^{-4} mbar Ar pressure, substrate kept at RT, meanwhile ITO was sputtered at 120 W power, 10^{-3} mbar Ar pressure and substrate kept at 200 °C.

Fabricated CZTSe(S) solar cells were cut into 3x3 mm^2 size subcells with micro-diamond scriber MR200 OEG. After solar cell's parameters were determined, some samples were etched in 10 % HCl solution for 5 – 15 min. By doing so, the CdS, ZnO and ITO layers are removed therefore CZTSe surface morphology can be directly investigated by SEM.

2.6 Characterization methods

CZT and CZTSe thin films were characterized using traditional structural characterization techniques:

- **XRD**. Phase composition was measured by x-ray diffractometer D8 Advance (Burker AXS) with Cu K_α radiation (wavelength 0.154183 nm). The XRD patterns were measured in grazing incidence (GID) step scan mode with a step size of 0.04° (in 2Θ scale) and counting time of 5–10 s. An incidence angle of the primary beam was 0.5°. Phase identification was performed using the powder diffraction data-base PDF-2 (2003 release). XRD *in situ* high temperature and high resolution measurements were conducted using x-ray diffractometer SmartLab (Rigaku) with 9 kW rotating Cu anode. The primary x-ray beam was conditioned by multilayer Ni/graphite monochromator CBO (cross beam optics) and two bounce Ge (220) monochromator. However, if conventional slit optics were used for a diffracted x-ray beam the intensity of the latter would be too low. That is why CALSA analyzer along with D/tex Ultra linear detector was used. The CALSA analyzer contains eleven specially arranged Ge (111) mono-crystal plates and that results in much higher intensity of Cu $K_{\alpha 1}$ (0.15406 nm) radiation compared with other monocrystalline analyzers. Preliminary annealing of CZT precursor was studied using XRD high temperature stage DHS 1100 (Anton Paar). For these studies conventional Bragg-Brentano optics with a graphite monochromator on the diffracted beam was used. The CZT precursors were examined in the temperature range from +200 up to +350 °C under helium atmosphere.
- **SEM**. Scanning electron microscopy studies were carried out in HELIOS Nanolab 650 (FEI) scanning electron microscope with field emission electron source and imbedded focus ion beam (FIB) system. Elemental analysis was measured with an X-ray energy dispersive spectrometer (EDX) from Oxford Instruments calibrated with Cu plate at 20 kV accelerating voltage. Cross-sections of CZTSe samples were prepared by two methods: i) using 30 keV energy focused Ga ions beam a trench

was cut in the sample ii) samples were cut with diamond cutter from glass side, then mechanically cleaved. It should be mentioned that to protect the investigated sample surface layer when cross-section is prepared by FIB method, before cutting thin (~100 nm) platinum layer was deposited on top of the sample. Therefore in all SEM images of FIB prepared cross-section the observed top granular layer is Pt.

- **Raman**. Raman measurements were performed with 632.8 (diode laser) and 442 nm (He-Cd) excitations by using the Raman microscope inVia (Renishaw) equipped with a gratings containing 1200, 1800, and 2400 grooves/mm. Laser power at the sample was 0.2 and 0.8 mW for 632.8 and 442 nm excitation wavelengths, respectively. Raman spectra were taken using a 50× objective lens. Integration time was 100 s. Parameters of the peaks were determined by fitting the experimental contour by Gausian-Lorentzian form components using Grams386 software.
- **XPS**. Atomic concentration depth profiles as well as element oxidation states were analyzed using ESCALAB 250 MK-II, equipped with dual Mg/Al anode. Measurements were performed at ultra-high vacuum (10^{-9} mbar), without monochromator, using 20 eV pass energy. Charge correction was calibrated by shifting adventitious C-C peak to 284.8 eV.

Solar cell characterization was performed using an AAA class solar simulator (SUN 3000 Abet Technologies) with uniform illumination over 15x15 cm^2 area, equipped with an AM1.5 filter. IMAC software was used to calculate solar cell parameters from I-V curves. External quantum efficiency was measured using a PVE300 Bentham system (wavelength range: 300-1600 nm). Prior to measurements the EQE was calibrated with Si and Ge photodiodes in the wavelength range of 300 -1600 nm.

Room temperature photoluminescence measurements were carried out using diode-pumped solid-state (DPSS) laser (532 nm) as an excitation source.

Laser power varied from 3 mW to 190 mW, and beam was focused into ~0.4 mm^2 spot. Photoluminescence was dispersed through 0.4 m monochromator, and detected by liquid-nitrogen- and thermoelectrically-cooled InGaAs detectors.

3 Theory

The theory of electrochemistry briefly described in following chapter was adapted from [104, 105, 106].

3.1 Electrode reaction

When electrodes are immersed in the solution with dissolved chemical species which possesses two different oxidation states, oxidized (Ox) and reduced ($\mathrm{Re}\,d$) and external power supply is connected to the electrodes, a non-spontaneous reaction occurs at the electrode/solution interface. This electrochemical reaction is the basis of electrodeposition.

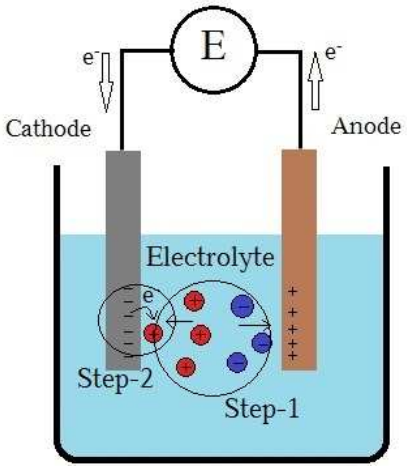

Figure 3.1: Diagram of electrochemical cell under potential with two immersed electrodes in the solution containing electroactive species.

When external voltage is applied current flows through electrodes and solution. At the interfaces of cathode/solution and anode/solution reduction

and oxidation reactions take place, respectively (Fig. 3.1) which can be written as:

$$Ox + ze^{-} \Leftrightarrow \mathrm{Re}\,d\,, \qquad (3.1)$$

where Ox - oxidized specie, z – number of electrons transferred per specie, $\mathrm{Re}\,d$ – reduced specie.

In order to maintain continuous flow of electrons oxidized species must be supplied to the electrode surface (mass transport, Fig. 3.1 step-1), then heterogeneous electron transfer process from the solid electrode to oxidized species must take place (electron transfer, Fig. 3.1, step-2). Depending on the nature of reduced species following processes after electron transfer at the electrode surface can take place: coupled chemical reaction, adsorption or formation of phases. In this study the latter process is most important, because electrodeposition of metals is occurring during this particular process. It is a multi step process where firstly starts nucleation, then crystal growth by atom diffusion to the appropriate site of the crystal lattice. On the other hand, in electrochemistry the reduction of electroactive species often occurs via several stages. For example, if complexing agent is present in the solution and forms metal complexes with negative overall charge, the reduction of metal at cathode will occur via several stages: diffusion and absorption of complexed species, the dissociation of complexed species via chemical or electron transfer reaction and depending on the final product either the reduction of metal ions occurs or adsorption of neutral particle.

To reduce certain amount of oxidized species in the solution *n* electrons must be released from the electrode (cathode) and supplied to the species. Thus the current passing through the cell is directly proportional to the amount of Ox species reduced. This is known as first Faraday's law of electrolysis:

$$Q = z \cdot F \cdot n\,, \qquad (3.2)$$

where Q – electrical charge, F – Faraday constant (96485 C mol^{-1}), n – mole of species reduced.

If we take into account the charge variation with time which is current one can arrive to equation (3.3) as follows:

$$\frac{dQ}{dt} = i = z \cdot F \cdot \frac{dn}{dt} \qquad (3.3)$$

Variation of the mole number with time dn/dt reflects variation of concentration per unit time which is the reaction rate ν (mol·s^{-1}). Rearranging equation (3.3) one can arrive at the following:

$$i = z \cdot F \cdot \nu \qquad (3.4)$$

This expression shows that current flowing in the external circuit of the cell is proportional to the rate of electrode reaction.

First Faraday law of electrolysis could also be used for calculating the amount of material deposited on the electrode. However in the thin film electrochemical deposition often the thickness of deposited layer is important. Thus taking equation (3.2), replacing $n = m/M$, $m = \rho \cdot V$, $V = d \cdot A$ and presumably current is not constant per unit time one can arrive at the equation for calculating deposited layer thickness:

$$d = \frac{\int_0^t I(t)dt \cdot M}{z \cdot F \cdot \rho \cdot A} \ , \qquad (3.5)$$

where, ρ is the density of deposited layer, M – is the molar mass of reduced specie, A – is the active electrode area where deposition takes place.

3.2 Potential and electrochemical cells

According to the band theory in the metal all electrons are populated below Fermi level. If we apply potential to the electrode (metal) Fermi level is shifted

from equilibrium value depending on magnitude and polarity of applied voltage (Fig.3.2). When electroactive species are present at the electrode

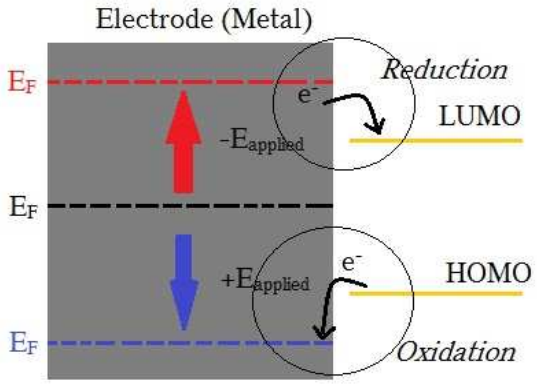

Figure 3.2: Fermi-level within metal and orbital energies of species present in solution.

surface an electron transfer can take place. If Fermi level of electrode is higher than lowest unoccupied molecular orbital (LUMO) of specie electrons start to flow from electrode into empty orbitals. Thus the reduction process of species takes place. If Fermi level is lower than highest occupied molecular orbital (HOMO) of specie, electrons flow from specie to electrode – oxidation process activates. The critical potential at which electron transfer processes occur is named as standard potential, E^0. However it is not possible to measure rigorously the absolute potential on electrode. Instead, in electrochemistry potential difference is measured. In the two-electrode cell, potential difference between electrodes is the sum of a series of potential differences: potential drop on each of electrode/solution interfaces and potential drop on R_s (solution intrinsic resistance). In order to accurately measure the potential difference on working electrode the third reference electrode is introduced. Nowadays all electrochemical cells comprise of three electrodes: working electrode, auxiliary electrode and reference electrode. Reference electrode's potential remains constant in the wide range of temperature, is independent on electrolyte nature and usually is located as

close as possible to the working electrode to make the $i \cdot R_s$ potential drop negligible. In this manner one can accurately control and measure potential difference on working electrode.

In order to calculate equilibrium potential for certain electrochemical cell system Nernst equation is used:

$$E = E^{0`} + \frac{RT}{zF} \ln \frac{C_O^*}{C_R^*} \text{ or } E = E^0 + \frac{RT}{zF} \ln \frac{a_O}{a_R}, \qquad (3.6)$$

where $E^{0`}$ is the formal potential, E^0 is the standard potential, C_O^* is the bulk concentration of the oxidized specie, C_R^* is the bulk concentration of the reduced specie, a is the activity.

The standard potential is measured in the following way: a metal electrode of consideration is immersed in the solution with 1 M concentration of dissolved same metal salt and given versus normal hydrogen electrode (NHE) reference electrode. The metals of consideration in this work are copper, tin, zinc and their standard potentials are +0.34, -0.13,-0.76 V vs NHE, respectively. In order to exploit co-deposition method of these three metals, their equilibrium potentials should be as close as possible. In electrochemical deposition complexing agents are used to overcome particular problem. By introducing complexing agent into the solution it forms complexes with dissolved specie:

$$M^{z+} + \alpha L \Leftrightarrow ML_\alpha \qquad (3.7)$$

Where M^{z+} is metal ion, α - coordination number, L is ligand

And their equilibrium constant β_α is expressed as:

$$\beta_\alpha = \frac{[ML_\alpha]}{[M^{z+}][L]^\alpha} \qquad (3.8)$$

Now the equilibrium potential for such system with metal complexes will be:

$$E = E^{0`} - \frac{RT}{zF} \beta_\alpha + \frac{RT}{zF} \ln \frac{[ML_\alpha]}{[M][L]^\alpha} \qquad (3.9)$$

It follows from equation (3.9) that if we form stable (large value of β_α) metal complexes, potential can shift negatively by significant value. Therefore using appropriate complexing agents one is able to equalize equilibrium potentials of different metals.

3.3 Cyclic voltammetry

Cyclic voltammetry is a powerful technique to identify electrochemical reaction mechanisms as well as to determine kinetic parameters and rate constants. In electrodeposition cyclic voltammetry is used to determine reduction potentials for electroactive species present in the solution.

Method is based on applying continuously time–varying potential to the working electrode. The time varying profile of applied potential is depicted in Fig. 3.3 A and current response to applied voltage in Fig. 3.3 B.

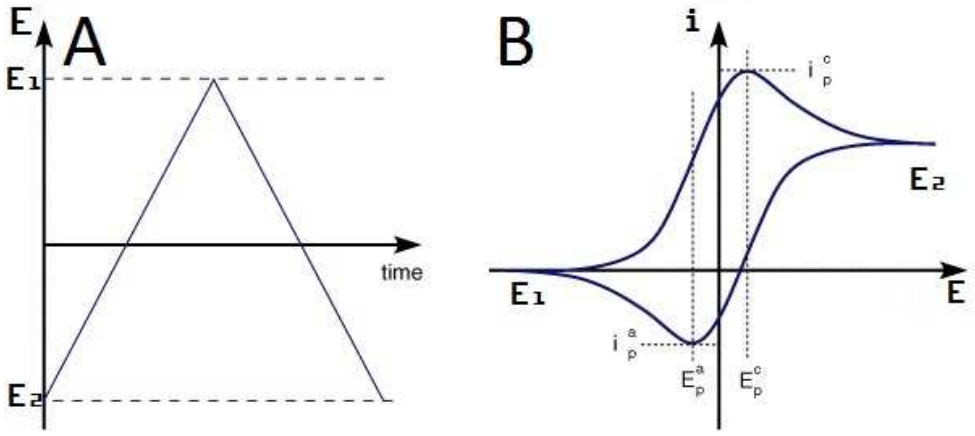

Figure 3.3: Typical time-varying potential profile in cyclic voltammetry (A) and j-E curve (B).

When potential is gradually increased it reaches the vicinity of E^0 of electroactive specie, the current starts to flow. As the potential grows, the surface concentration of oxidized specie drops; hence the flux to the surface

(and the current) increases until it reaches maximum. Further growth of potential results in depletion effect and the current starts to decrease. As a consequence a wave form curve is obtained in the j-E graph (see Fig. 3.3 B). At certain point potential sweep direction is reversed and the same phenomenon occurs resulting in the similar current shape like that of the forward peak. If there are several electroactive species with different E^0 one will obtain several wave form peaks.

In electrodeposition, the cyclic voltammetry is used to determine the optimum deposition potential. Because the electrodeposition is usually performed under hydrodynamic conditions instead of the wave form j-E curve one will obtain cliff-like curve, see Fig. 3.4.

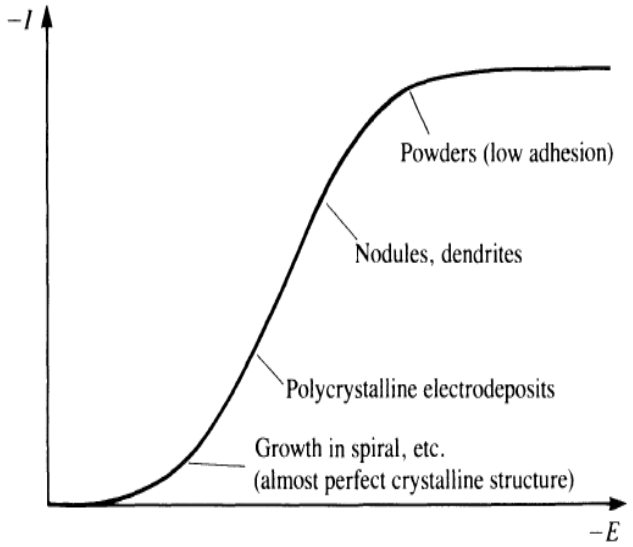

Figure 3.4: A fragment of typical j-E curve of electrochemical system under hydrodynamic conditions.

The applied potential governs the rate of deposition thence the structure of deposits. Variation of electrodeposit structure with applied potential is depicted in Fig. 3.4. At very low deposition rates one can obtain perfect crystalline structure, however prolonged times are required to deposit layer. As the deposition rate is increased polycrystalline layer is deposited and at the

highest possible rate dendritic and powder-like growth occurs. Hence, it is important to know deposition rate and to control deposition potential as they directly affect the structure of deposited layer.

3.4 Working mechanism of solar cell

Typical solar cell performance is based on photovoltaic effect in p-n junction. Band diagram of two semiconductors in contact at equilibrium is depicted in Fig. 3.5. When photons with energy equal or greater than that of the semiconductor E_g strike p-n junction, they are absorbed by valance electrons and carrier pairs (hole and electron) are generated. Intrinsic p-n junction electric field separates carrier pairs: electrons are swept to n type semiconductor, whereas holes to the p-type. The charge equilibrium is disrupted by light-generated carriers; therefore electric field opposite in direction to p-n junction electric field generates. The new equilibrium is reached and voltage exits across a p-n junction and is called an open-circuit voltage (V_{OC}). Now the diffusion and drift current are balanced out and the net current is zero. If we short-circuit the p-n junction the light-generated

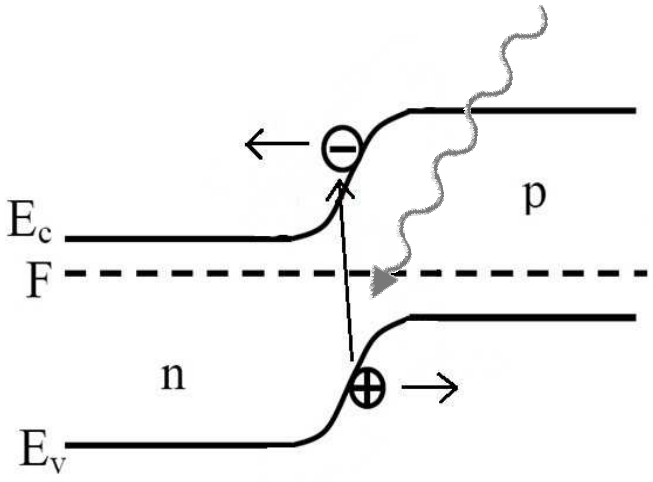

Figure 3.5: Band diagram of p-type and n-type semiconductor in contact under illumination.

carriers are allowed to flow through external circuit thus there is no build up of charge thence no generation of voltage across p-n junction. The current which is measured under these condition is called short-circuit current (I_{SC}).

3.5 Solar cell parameters

In order to obtain solar cell parameters such as V_{OC}, η, I_{SC} *etc.* the I-V curve of solar cell is measured under dark and illuminated conditions. The light has effect that it shifts an I-V curve into the 4th quadrant where power of diode can be extracted (Fig. 3.6). The relationship between current and voltage in the solar cell under illumination is described by standard diode equation:

$$I = I_0[\exp(\frac{qV}{nkT}) - 1] - I_L, \qquad (3.10)$$

where I_0 – dark current, q – elementary charge (1.602·10^{-19} C), V -applied voltage, n – diode ideality factor, k – Boltzman constant (1.38·10^{-23} J/K), T – temperature, I_L – light generated current.

The simulated I-V curve of solar cell is depicted in Fig. 3.6. Dark current (I_0) is very important parameter as it is a measure of the recombination in a device. Low values of I_0 imply large recombination exits in the solar cell. I_0 value is extracted from I-V curve measured under dark conditions. Short-circuit current (I_{SC}) is a measure of maximum current that can be extract from solar cell and is defined when no voltage exists in solar cell. The open-circuit voltage (V_{OC}) is the maximum voltage generated by photovoltaic effect when there is no current flow.

Under ideal conditions the maximum power of the solar cell would be the product of $V_{OC} \cdot I_{SC}$, however due to carrier recombination, parasitic resistance and optical losses the solar cell I-V curve is not square and the

$P_{\max}$ is obtained at so called diode operating point and is the product of $V_{MP} \cdot I_{MP}$ (see Fig. 3.6). The ratio between $V_{MP} \cdot I_{MP}$ and $V_{OC} \cdot I_{SC}$ is called

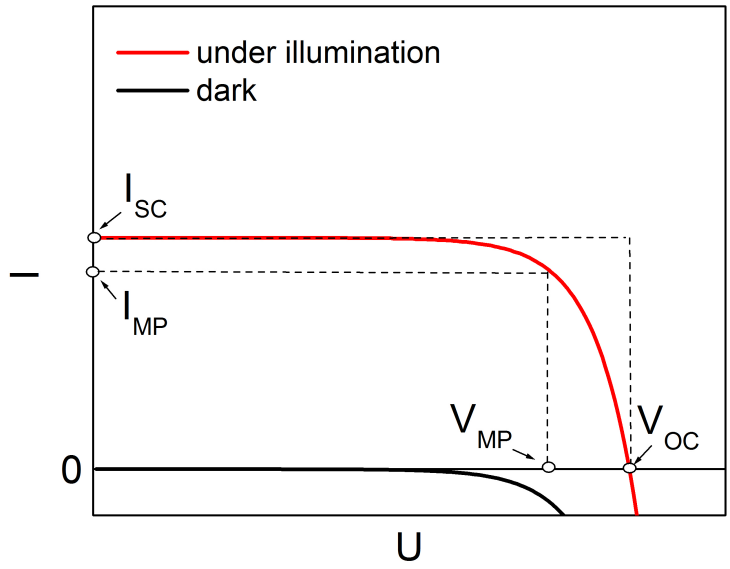

Figure.3.6: Simulated I-V curve of solar cell under dark and illuminated conditions.

the fill factor (FF). It shows how much of power solar cell generates in comparison to ideal case. The most important parameter of solar cell is the power conversion efficiency (η). It is the ratio of solar cell generated power with incident light power and is describe as:

$$\eta = \frac{P_{solacell}}{P_{light}} = \frac{FF \cdot V_{OC} \cdot I_{SC}}{P_{Light}}, \qquad (3.11)$$

where P_{light} is incident light power density and by default is assumed to be 1000 W/m^2.

Due to fundamentals of solar spectrum and semiconductor properties the maximum obtainable efficiency of solar cell depends on semiconductor band gap. According to Shockley and Queisser studies the optimum band gap of absorber should fall in the range of 1.0 – 1.5 eV [107]. In this case maximum the theoretical solar cell efficiency is 30-34%.

4 Results and discussion

4.1 Sputtered molybdenum substrates

4.1.1 Molybdenum resistance and adherence

As has been mentioned in the literature review, Mo microstructure strongly depends on the sputtering conditions, which in turn determines its physical properties. The main sputtering parameters that have been investigated in this study were substrate temperature (RT – 200 °C), sputtering power (200 – 400 W) and working Ar pressure (2 – 20 mTorr). The latter one is the most crucial because it significantly affected Mo microstructure. Specific resistance of Mo films was measured by two points probe method. The thickness of the Mo layers was evaluated from the FIB made Mo/glass cross-sections images. The dependence of Mo film resistance on working Ar pressure during sputtering is depicted in Fig. 4.1. It can be clearly seen that specific resistance of Mo films increases as Ar pressure is increased (black line with empty circles). Crystallite size (D) was calculated from XRD data and as can be seen it increases as pressure is decreased. It is expected result, because using lower working Ar pressure sputtered Mo atoms have higher kinetic energy and tend to grow into larger crystallites. Naturally, the larger the crystallites the higher mobility of the carriers and therefore higher film conductivity. When substrate heating was introduced the tendency of specific resistance remained the same, it increased as Ar pressure was increased, but the effect was not so pronounced (Fig. 4.1 red curve).

In general films deposited at pressure lower than 10 mTorr tended to peel-off during selenization of electrodeposited CZT precursor. On the other hand, films sputtered at higher than 10 mTorr Ar pressure were relatively

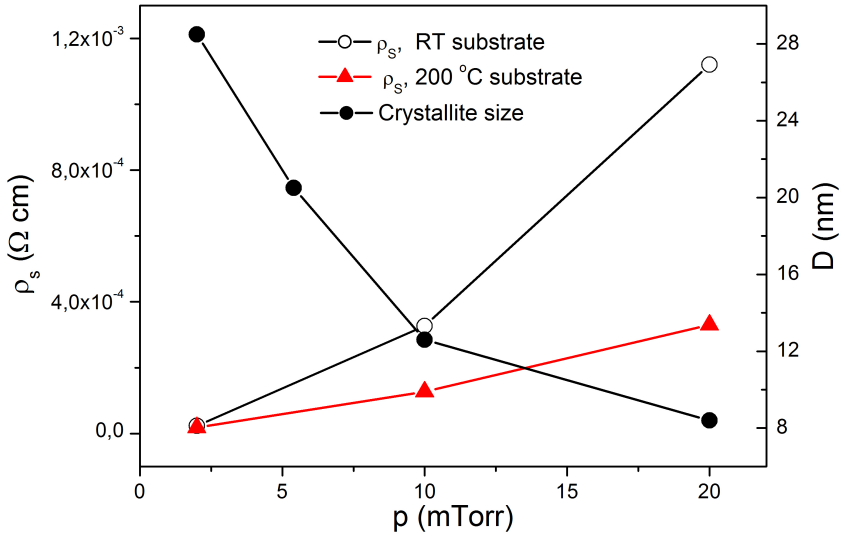

Figure 4.1: Dependence of specific resistance and crystallite size of Mo films on sputtering pressure. Films were sputtered at 300 W power and substrate temperatures 25 °C (black line) and 200 °C (red line).

resistive (ρ_s >3.3·10^{-4} Ω·cm). In comparison the resistivity of bulk Mo is ρ_s= 5.4·10^{-6} Ω·cm. Thus as a compromise double layered Mo films were deposited. Based on XRD, SEM results and measurements of Mo specific resistance the optimal sputtering parameters for top layer were 300 W, room temperature substrate and 2 mTorr of Ar pressure, whereas bottom layer was deposited at the same conditions except Ar pressure was varied. FIB made cross-sections of Mo double layers are depicted in Fig. 4.2. Thicknesses of top and bottom layers were ~550 and ~200 nm, respectively. It can be clearly seen that porosity of bottom Mo layer increased as pressure was increased from 7.5 to 15 mTorr. The goal was to find at which lowest pressure, sputtered bottom Mo film is well-adherent to the glass. After numerous electrodeposition steps and annealings, empirically the bottom Mo layer deposited at 12.5 mTorr proved to be the optimum pressure. The specific resistance of all four samples did not vary significantly and was in the range of 1.1 – 1.9 10^{-5} Ω·cm, which is expected because the top Mo layer is the same

for all samples and mostly contributes to the overall layer conductivity. Thus particular double layered Mo films were highly conductive and well adherent to the glass.

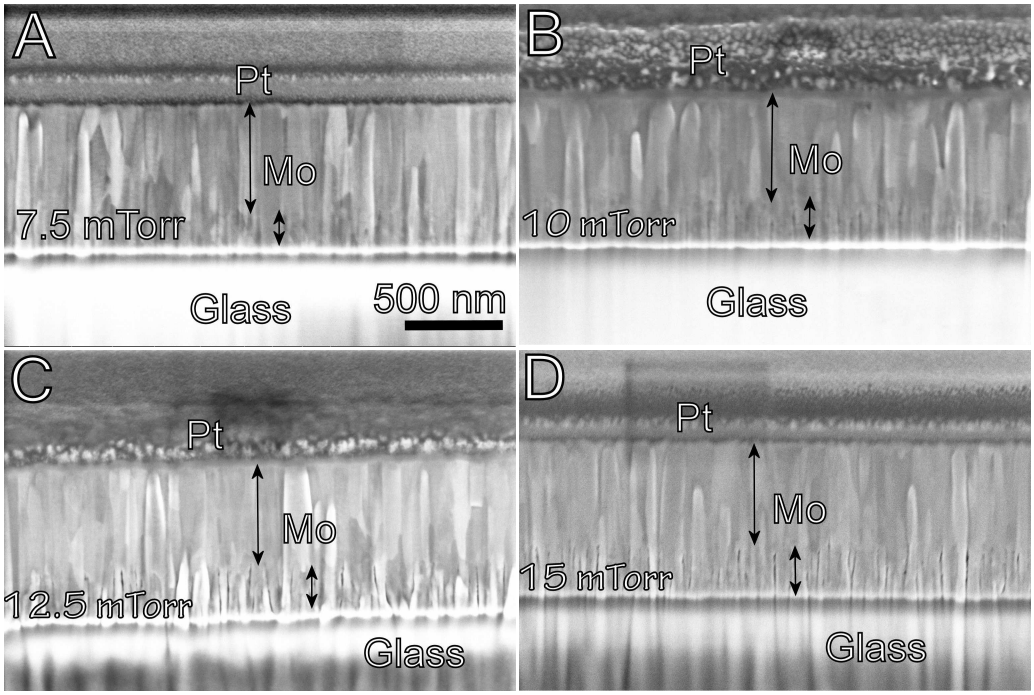

Figure 4.2: SEM micrographs of double layered Mo cross-sections with bottom layer deposited at different Ar pressure. Sputtering power – 300 W, substrate temperature –RT. Scale bar applies to all images.

4.1.2 Molybdenum selenization

Selenization of Mo depends on annealing conditions i.e. temperature, time, Se pressure [108], but it also depends on Mo microstructure as has been reported in [76]. In order to clearly identify the relationship of $MoSe_2$ formation and Mo microstructure, we have annealed three Mo samples which were deposited at different Ar pressures, but selenized under the same conditions. Selenization was performed in tube furnace at 550 °C for 30 min with 5 mg of Se powder inside a container. The thickness of $MoSe_2$ was

determined by EDX elemental profile analysis and SEM cross-section images, which are presented in Fig. 4.3. As can be seen, films sputtered at 2 mTorr are readily selenized and the measured thickness of $MoSe_2$ was 1730 nm. Mo layers deposited at 5.5 and 10 mTorr were selenized to much less extent; the thickness of $MoSe_2$ was 390 and 300 nm, respectively. The relationship between $MoSe_2$ thickness and Ar pressure is not linear, indicating that a certain pressure value exits, from which sputtered Mo layers are not readily selenized. Yoon also have found pressure regions, where dependence of physical and structural properties of Mo films were inversed or constant [69]. Although several assumptions were proposed explaining different selenization properties of Mo films deposited at different Ar pressure [76, 77], it is not yet clear why porous Mo films are less selenized than compact one.

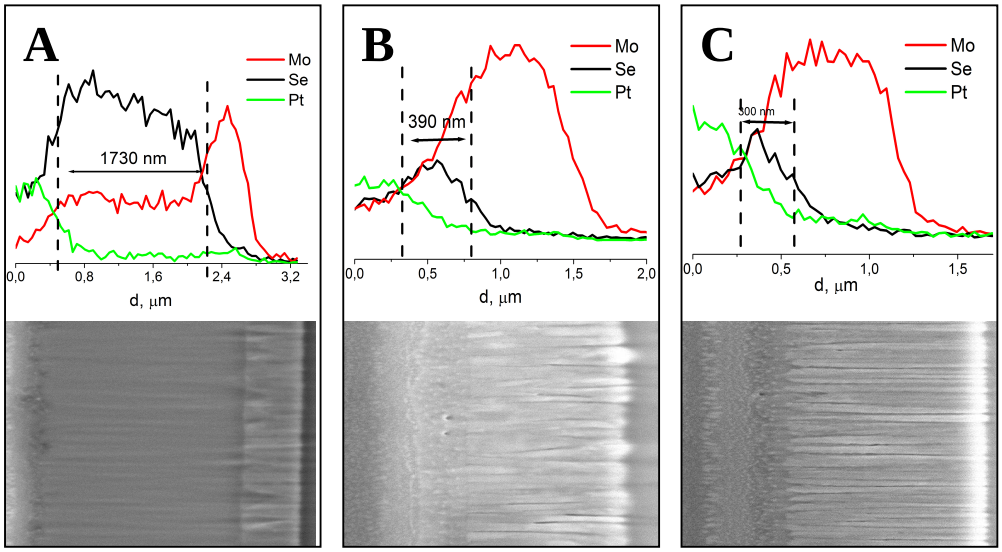

Figure 4.3: Elemental profile measured by EDX and corresponding SEM images of selenized Mo layers sputtered at (A) 2 mTorr, (B) 5.5 mTorr, (C) 10 mTorr.

As we can see compact Mo films tend to form thick $MoSe_2$ layer during selenization. Too thick $MoSe_2$ can be the reason of the poor CZTSe morphology and even cause the layer to peel-off, furthermore in solar cell device it can increase series resistance, so the control of $MoSe_2$ is important.

Top layer of Mo samples discussed in §4.1.1 was deposited at low Ar pressure (2 mTorr), therefore a very thick $MoSe_2$ will form during selenization. In order to avoid too thick $MoSe_2$ layer, the thicknesses of each Mo layers was adjusted. The optimal sputtering conditions of Mo back contact for Cu-Zn-Sn selenization was found to be: sputtering power 300 W, substrate at room temperature, 2 mTorr Ar pressure, 200 nm thickness for top Mo layer and 12.5 mTorr, 600 nm thickness for bottom Mo layer.

4.2 Electrochemical co-deposition of Cu-Sn-Zn precursor

4.2.1 Molybdenum surface preparations

Adherence to the Mo substrate is a challenging issue. In general Cu, Sn or Zn do not well adhere to Mo [109]. In order to improve cohesion of CZT films and substrate, four different Mo surface preparations were investigated. The summary of different preparations is presented in table 4.1.

Table 4.1: Recipes of Mo surface preparation.

Name	Material	Comments
Sol1	$K_3[Fe(CN)_6]$+NaOH	Mild oxidizing agent
Sol2	$K_4[Fe(CN)_6]$+NaOH	Intended to remove surface oxide layer
Strike Ni	$NiCl_2$+HCl	Electrochemical deposition of thin Ni layer for improving adherence
Sol3	25% NH_4-OH	Intended to remove Mo surface oxide layer

After numerous electrodepositions of CZT it was noticed that after immersing in solution Sol1 CZT films always adhere to Mo, whereas after immersing in solution Sol2 it tented to peel-of. In order to find out the effect of different Mo surface treatments, XPS investigation of differently treated

Mo surface was carried out. In Fig. 4.4 the Mo and O atomic concentration profiles are depicted. The solutions Sol1 and Sol2 affect Mo surface differently, as expected. After immersion in solution Sol1 which is slightly oxidizing agent we observed the substantial increase of O content (red line with empty circles) on the surface. Whereas after dipping in Sol2 we observed the

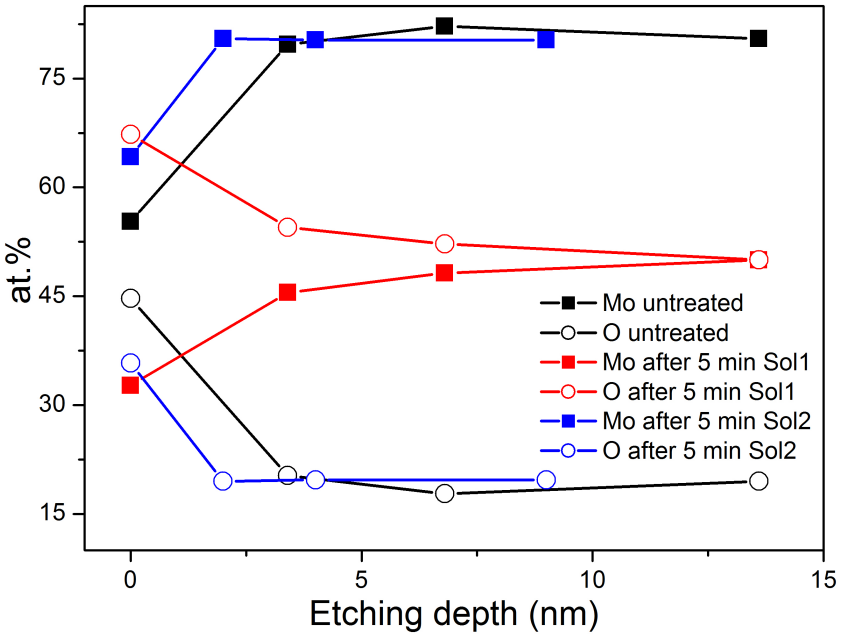

Figure 4.4: XPS depth profile of untreated Mo films and after chemical treatments in Sol1 and Sol2 for 5 min.

decrease of O most probably because of the removal of native Mo oxide layer. After etching ~4 nm the atomic concentration of Mo and O of reference sample and the one treated in solution Sol2 equalizes (blue and black lines), meaning solution Sol2 removes Mo oxide only from surface (or native MoO_x is formed only on the surface). On contrary, solution Sol1 affected deeper layers of Mo because even after etching ~14 nm the content of O was much greater than in reference sample (black line).

Morphology of Mo samples after treating in solution Sol1 and solution Sol2 is presented in Fig. 4.5. Mo surface after treating in solution Sol1 was modified: Mo oxide layer with a lot of pinholes, comb-like structure and increased surface roughness was observed, whereas after treatment in solution Sol2 no difference to reference Mo surface (Fig. 4.5 B inset) was visible. XPS data (not shown here) revealed that MoO_x is formed on the very

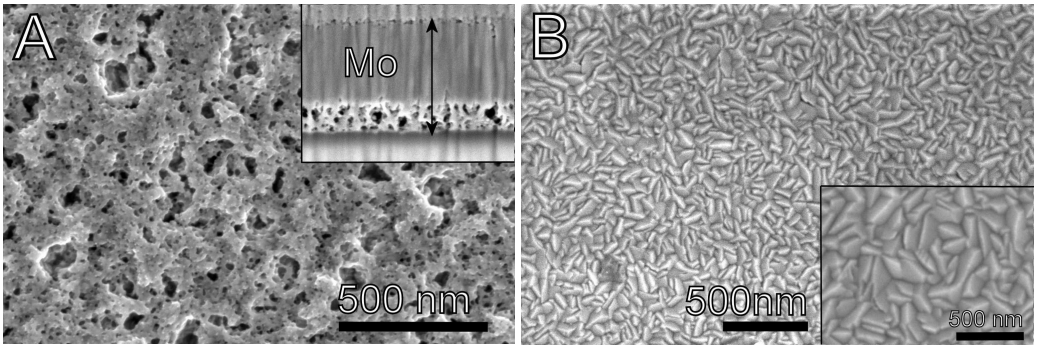

Figure 4.5: SEM micrographs of Mo surface morphology after immersion for 5 min in (A) Sol1, (B) Sol2. Inset (A) FIB prepared cross-section of Mo layer after immersion in Sol1, (B) surface morphology of untreated Mo.

surface after chemical treatment in solution Sol1. The better adherence between Mo and CZT after treating in solution Sol1 can be related to two phenomenon: i) after etching Mo morphology contains high density of pinholes and trenches, therefore because of the increased surrounding area, CZT grains in the early stage of electrocrystallization adhere better than on the smooth surface ii) because other metals do not well-adhere to Mo, the intermediate layer of MoO_x facilitates better cohesion of CZT and Mo. On the other hand, after chemical treatment in solution Sol1, microstructure of Mo is strongly affected (Fig. 4.5 A inset). We observed the increase in porosity and as has been demonstrated the increase in O content in the bulk of Mo. Taking into account that Mo has to serve as a back contact the treatment in solution Sol1 can strongly change long-term physical properties of Mo, such as

conductivity, therefore the surface preparation in solution Sol1 was disregarded.

In the Hansen [109] work it has been shown that in order to increase adherence of electrodeposited metal to Mo a thin layer of Ni can be exploited. For this purpose so called strike Ni (table 4.1) was electrodeposited on Mo by applying current density of j = 20 mA/cm^2 for a short period of time.

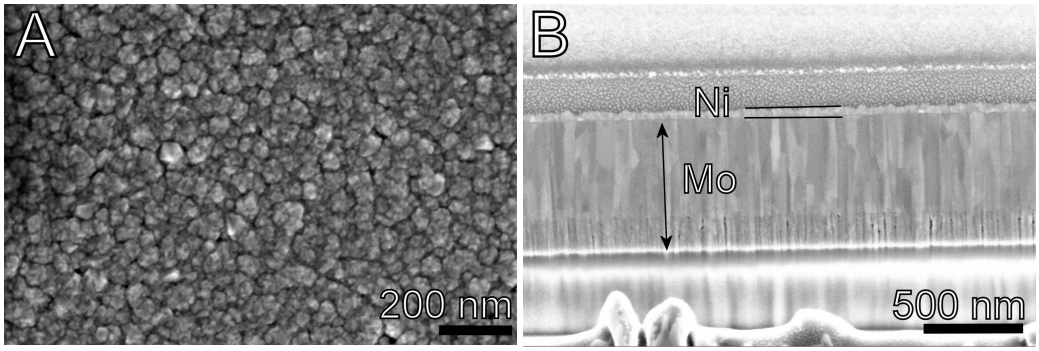

Figure 4.6: SEM micrographs (A) surface morphology and (B) cross-section of Ni film electrodeposited on Mo from $NiCl_2$ + HCl solution for 30 s at j = 20 mA/cm^2.

The morphology and cross section of Mo/strike Ni are depicted in Fig. 4.6. From Ni surface morphology (Fig. 4.6 A) it can be seen that grains were coalesced and formed continuous layer. In the SEM image of Mo/Ni cross-section (Fig. 4.6 B) we see that interface of Mo and Ni was uniform, without gaps or voids. Thus under mentioned conditions electroplated thin (~50 nm) Ni film is of high quality, well adherent and uniform.

Combining strike Ni deposition and chemical treatment in solution Sol2 a good adhesion of CZT to Mo was achieved, none of the films peeled off. Albeit good adhesion was achieved, it required an additional surface preparation step i.e. Ni deposition. From industrial perspective less processes to achieve the same result is more favourable, thus the commonly applied Mo surface

treatment in NH_4-OH was also tested. Mo films were immersed in the NH_4OH solution for 10 min, and then ultrasonically cleaned in the mixture of alcohol, isopropyl and acetone. The adherence of Cu-Zn-Sn films was similar when using intermediate strike Ni layer therefore this approach this approach was chosen for Mo surface preparation

4.2.2 Deposition potential and Cu-Zn-Sn composition

Firstly, in order to investigate Cu-Sn-Zn electrochemical co-deposition, polarization curve was recorded and is presented in Fig. 4.7. j-E curve in the range of -0.1 to -1.7 V vs Ag/AgCl/$KCl_{sat.}$ reference electrode was recorded in electrolyte containing 20 mM of $CuSO_4$, 14 mM of $ZnSO_4$, 10 mM of $SnSO_4$ and 100 mM of Na_3Cit at temperature of 20 °C and pH of 5.75, without stirring.

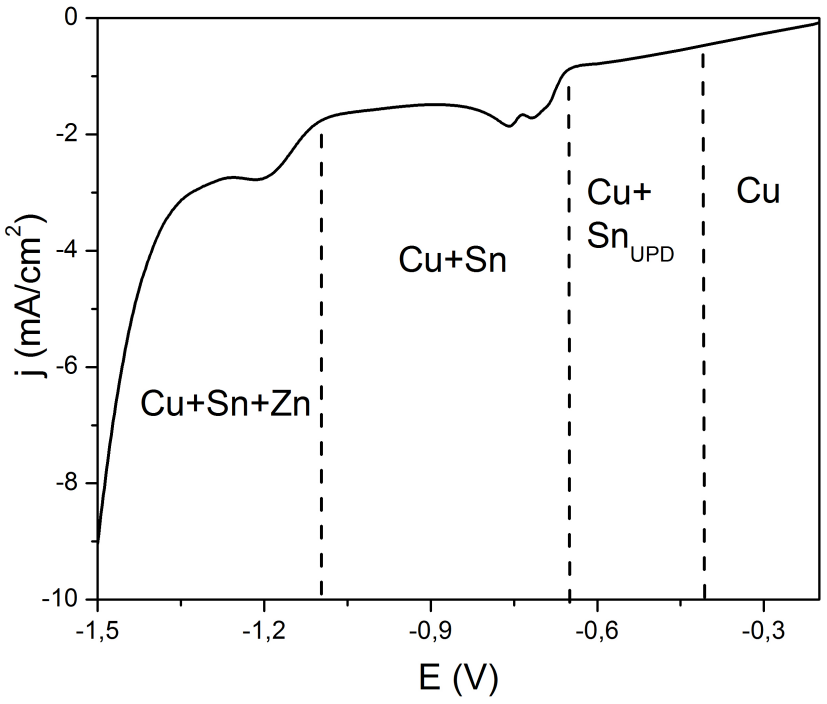

Figure 4.7: Voltammogram (scan rate 5 mV/s) of the Mo electrode in electrolyte solution with optimal composition (20 mM $CuSO_4$ + 14 mM $ZnSO_4$ +10 mM $SnSO_4$ + 100 mM Na_3Cit) without stirring.

In general polarization curves enable to identify metal deposition potentials and determine what reactions are under process. Based on the EDX data of the deposited films the recorded j-E curve (Fig. 4.7) can be divided mainly into four regions. In the first region only Cu deposition occurred at potentials from -0.2 V up to -0.4 V. Sn reduction started at lower than equilibrium potential (E^0_{Sn} =-0.65 V vs Ag/AgCl/$KCl_{sat.}$ [88]) and is indicated as Cu-Sn underpotential deposition. In this region yellow bronze that is tin solid solution in the copper was electroplated. In the potential range from -0.65 V to -1.15, reduction of Sn^{2+} ions along with those of Cu^{2+} took place and so called grey bronze was deposited. Further increasing negative potential, the reduction of Zn^{2+} ions at -1.1 V was observed and ternary Cu-Zn-Sn alloy started depositing. As potential reached even more negative values, the current increased because of more intensive hydrogen evolution reaction. The latter reaction caused tiny bubbles to appear at the electrode surface, which blocked the active area, increased porosity of the films and resulted in lateral inhomogeneity of CZT layer thickness and chemical composition. Therefore, the deposition potential must be carefully chosen and controlled. From these observations we know that to deposit ternary Cu-Sn-Zn alloy deposition potential must be in the range -1.1 – -1.4 V. Note that deposition rate of CZT films at -1.3 V was found to be ~0.05 μm/min. Composition of CZT precursor can be controlled by varying deposition potential: the more negative deposition potential the higher Zn quantity will be in CZT. On the other hand, potential window for CZT precursor is fairly narrow: -1.2 to -1.4 V because at the more negative deposition potential than -1.4 V intensive hydrogen evolution occurs which causes films to peel-of and other above mentioned problems.

The thickness of CZT films, deposited without stirring was very inhomogeneous, therefore solution agitation with magnetic stirrer was included. However, the optimal deposition potential under hydrodynamic

conditions slightly changed (Fig. 4.8). As can be seen the current density increased 2-3 times under hydrodynamic conditions. The polarization curve shifted about 0.2 V to the negative direction in comparison to the one without stirring (Fig. 4.7). The partial polarization curves are indicated for each metal and for H_2. The hydrogen evolution (grey curve) started at -0.8 V and reaction rate slowly increased as potential became more negative, but from -1.4 V it started significantly to rise. The reduction of Zn occurred at approx. -1.3 V and

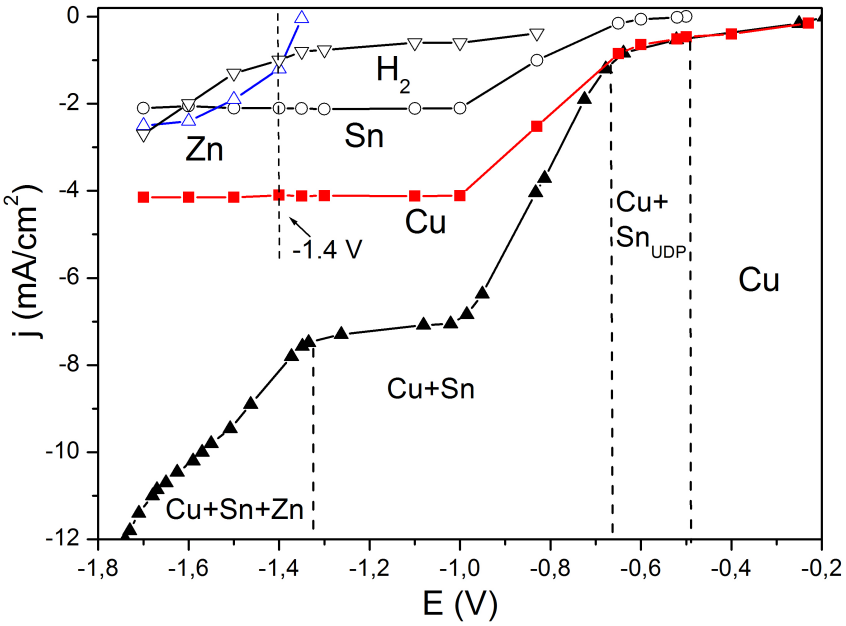

Figure 4.8: Potentiostatic polarization curve of the Mo electrode in electrolyte solution (20 mM $CuSO_4$ + 18 mM $ZnSO_4$ + 10 mM $SnSO_4$ + 100 mM Na_3Cit) under hydrodynamic conditions. Potentials referred to $Ag/AgCl/KCl_{sat}$.

its rate increased as potential became more negative, whereas the reduction rates of Cu and Sn kept constant. Therefore the deposition potential, at which intensive hydrogen evolution have not yet started, but appropriate content of Zn (25-30 at%) was deposited was found to be -1.4 V. The estimated deposition rate of CZT film at particular deposition potential was ~0.24

μm/min. It means that CZT films deposition rate was increased by a factor of 4.8 when solution stirring was introduced.

The typical surface morphology and cross-sectional view of CZT layer co-electrodeposited in stirred solution are depicted in Fig. 4.9. Visually deposited CZT films appeared grey colour, had mirror reflectivity and were uniform. From Fig. 4.9 A one can see that CZT layer comprised of small nanometer-size grains, which were coalesced into different size round shape clusters. Morphology of the films did not depend significantly on the deposition potential in the range of -1.3 – -1.4 V. From SEM image of cross-section we can see that films were porous due to hydrogen evolution, however well adherent to the Mo substrate and uniform in thickness. Note that porosity of

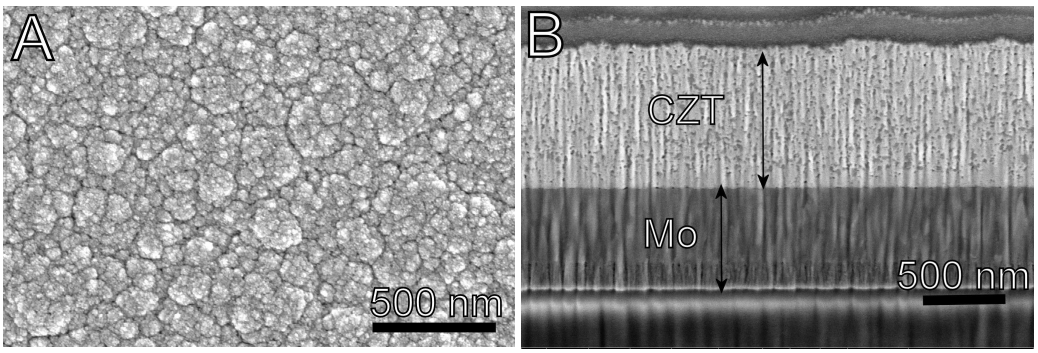

Figure 4.9: SEM images of surface morphology (A) and cross-section prepared by FIB (B) of the CZT layer deposited at E = -1.4 V vs Ag/AgCl/$KCl_{sat.}$ in stirred solution.

the films can be reduced by applying preheating treatment, but this will be discussed in the section 4.4.

To obtain better quality films i.e. with lower porosity and better adherence deposition potential should be as less negative as possible. In order to keep the required CZT composition, but to deposit at the less negative potential, concentration of Zn^{2+} ions in the solution have to be increased. The CZT composition dependence on the Zn^{2+} ions concentration in

the electrolyte is depicted in Fig. 4.10. The basic electrolyte contained 20 mM of $CuSO_4$, 10 mM of $SnSO_4$, 100 mM of Na_3Cit and $ZnSO_4$ concentration was varied from 10 to 20 mM. Films were deposited for 16 min at E of -1.3 V, pH was adjusted to 5.75, in unstirred solution. In Fig. 4.10 we can see the linear relationship between Zn quantity in the CZT films and Zn^{2+} concentration in the electrolyte. By using this dependence one can determine the necessary Zn concentration for targeted CZT film composition.

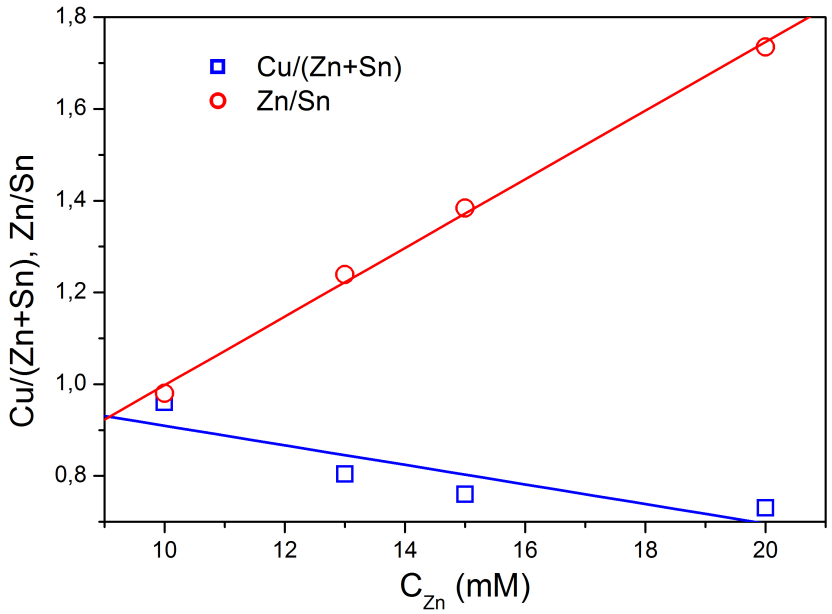

Figure 4.10: Dependence of Cu/(Zn+Sn) and Zn/Sn ratios in CZT precursor on zinc ion concentration in electrolyte solution. Atomic concentrations of metals were determined by EDX.

4.3 Stacked Cu, Sn, Zn layer electrodeposition with flow cell

Because of the peculiarities of flow cell construction, the Pt wire was used as a reference electrode and all given potentials in the following chapter will be referred to Pt wire. What is more, all following experiments were performed at room temperature.

4.3.1 Cu layer

For the deposition of Cu layer citrate electrolyte solution was chosen. The detail composition was as follows: 0.075 M $CuSO_4 \cdot 5H_2O$ + 0.25 M $Na_3C_6H_5O_7$ (Na_3Cit) pH – 5.6, which was adapted from [110]. Particular citrate electrolyte is relatively simple, non toxic and does not require additional organic additives. Furthermore, Cu forms complexes with citrate and at 5.6 pH the main dominating specie in the solution is $Cu_2(HCit_2)^{3-}$ [88, 111].

The deposition of Cu was investigated under galvanostatic as well as under potentiostatic conditions. The morphology of Cu did not depend strongly on the applied current density in the tested range of 1.5 – 5 mA/cm^2. In Fig. 4.11 SEM surface morphology and FIB made cross-section of typical electroplated Cu thin films are depicted. A, B images represent films deposited at constant current density of 3.2 mA/cm^2, flow rate – 400 ml/min

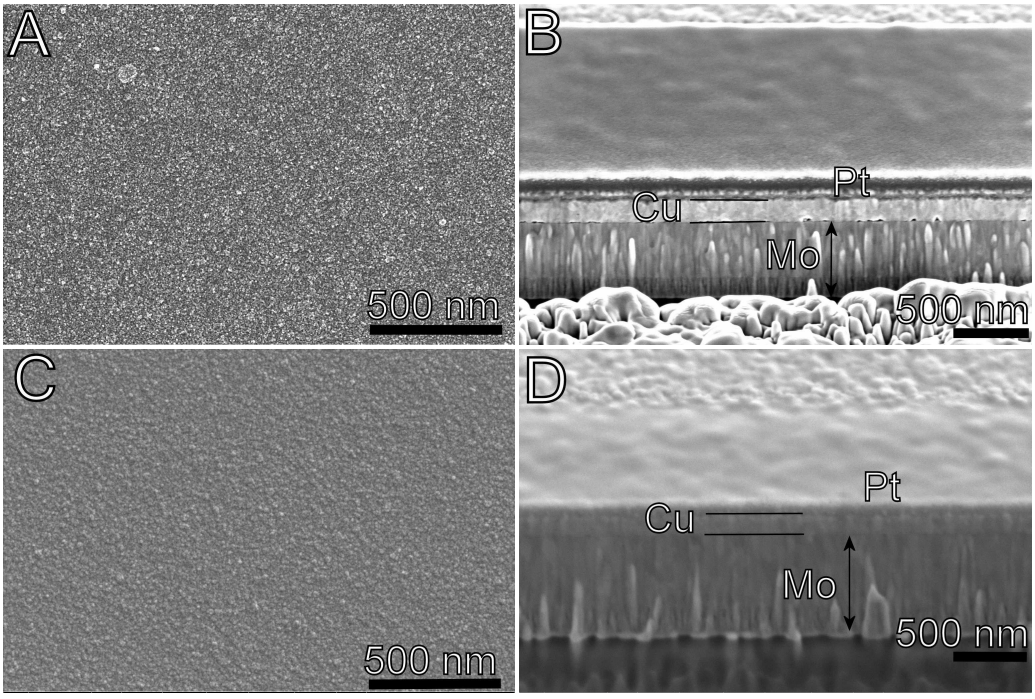

Figure 4.11: SEM micrographs of electrodeposited Cu thin films: (A, B) j =3.2 mA/cm^2, flow rate=400 ml/min, (C, D) E= -1.0 V, flow rate=400 ml/min.

and deposition time 205 s, whereas in C, D Cu was deposited at potential -1.0 V vs Pt wire reference electrode, flow rate – 400 ml/min and deposition time 180 s. Firstly, films deposited either way were smooth, uniform and had a mirror reflectivity. As can be seen from morphology galvanostatically deposited Cu layer comprised larger and finer grains than under potentiostatic conditions.The cross-section images revealed that films were uniform in thickness and in the case of galvanostatically deposited films 15-20 nm pores were visible at the interface between Mo and Cu films. Larger grains of galvanostatically deposited films can be related to the lower current density. During potentiostatic deposition average current density was 4.4 mA/cm^2. The smaller current density is, the larger and more perfect grains starts to grow as has been discussed in §3.3. Smaller grains are favourable because in order to obtain more homogenous in composition and in thickness Cu/Sn/Zn precursor, each layer has to be as uniform as possible. Another advantage of depositing under potentiostatic conditions is the initial nucleation step. By applying overpotential a lot of nucleation sites were generated on Mo substrate, which was observed by huge increase in initial current density (up to 13 mA/cm^2). Then small Cu grains started to grow until they coalesced and whole electrode surface was uniformly covered. Meanwhile, under galvanostatic conditions potential increased gradually during first 2-5 s. This could be related to the progressively increasing diffusion-limited electrochemical processes. As a consequence, the generated Cu nuclei at the initial moment grew unevenly and various size Cu grains have formed, this is what we observed in Fig. 4.11 A.

The influence of flow rate on a quality of Cu deposits was not significant and was investigated visually (colour uniformity, layer peel-off, etc.). Howerver, it was noticed that when the same potential was applied, the average current density during deposition was depended on the flow rate. Naturally, the higher the flow rate, the higher current density. As it was

shown above, high current density (j > 4 mA/cm^2) leads to more smooth Cu films. Therefore the flow rate we used for Cu deposition was in the range of 350-400 ml/min.

Based on SEM results, the most suitable depositions conditions for electrodeposition of Cu using flow cell were: deposition potential in the range of -0.94 – -1.0 V vs Pt wire reference electrode, flow rate 350 – 400 ml/min and electrolyte composition – 0.075 M $CuSO_4 \cdot 5H_2O$ + 0.25 M $Na_3C_6H_5O_7$.

4.3.2 Sn layer

For the deposition of Sn layer two electrolytes were tested in this work. Their composition is summarized in table 4.2. The citrate based solution was adjusted from electrochemical co-deposition solution and methanesulfonic acid (MSA) based solution was adapted from [68, 90]. Mo covered with electrodeposited Cu (80 – 100 nm) layer was used as a substrate.

Table 4.2: The composition of Sn electroplating solutions.

Solution name	Complexing agent	Source of Sn^{2+}	Additives
Sn-Citrate	0.3 M $Na_3C_6H_5O_7$	0.22 M $SnCl_2$	Hydrochinon
Sn-MSA	1 M CH_3SO_3H	0.05 M $SnSO_4$	Hydrochinon, TrintonX-100

To begin with, Sn was deposited under galvanostatic conditions. The surface morphology of Sn layers electrodeposited at 6 mA/cm^2 but with different flow rates are depicted in Fig. 4.12. As can be seen from Sn surface morphology the flow rate does not have considerable impact on Sn layer morphology. In both cases films were composed of large 0.5 – 1.5 µm size grains, compact and formed continuous layer. However, from visual inspection it was noticed that Sn layer was not uniform over all electrode

surface on centimetres scale. In general the appearance of films were white opaque colour, but films, deposited using 320 ml/min flow rate were more uniform (in visual appearance) than the ones, deposited at 400 ml/min. The middle of the electrode was usually more opaque than edges and corners when 400 ml/min flow rate was used. This could be related to the velocity of solution flow, which is expected to be highest in the middle of the electrode because the solution flow in the cell presumably is not perfectly laminar. Naturally, areas that appear more opaque are either composed of larger grains or is rougher and often indicates thicker layer.

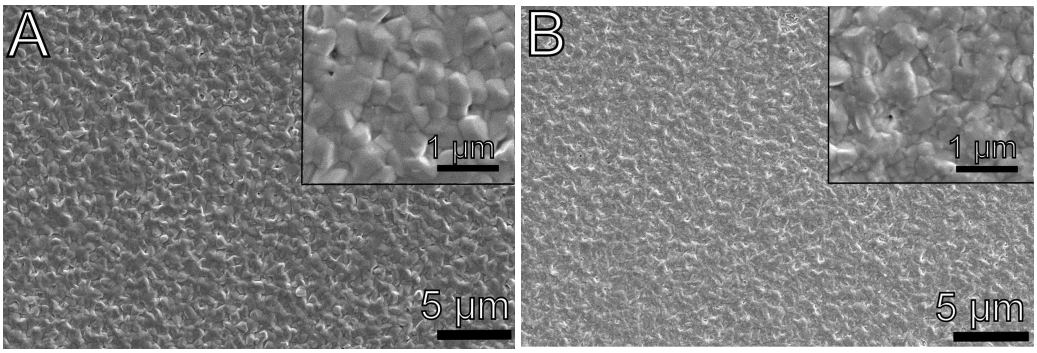

Figure 4.12: SEM micrographs of Sn layer deposited from citrate based solution at 6 mA/cm^2 with different flow rates: (A) 320 ml/min, (B) 400 ml/min. Inset – at higher magnification.

In order to obtain uniform films, another Sn plating solution, which was implemented in other authors' studies, was tested [68, 90, 94]. It is methanesulfonic acid based solution, which is often used for industrial Sn electroplating [112]. Firstly, deposition was carried out under galvanostatic conditions. Morphology of Sn deposited at 4.5 mA/cm^2 from MSA solution is presented in Fig. 4.13. Layer comprised of various fine grains which size was in the range of 0.2 – 0.8 µm, was compact, continuous, however little holes between the grains were observed. From the visual appearance layers were more reflective, white bright and more uniform than deposits from citrate

solution. Specular appearance of Sn films is related to smaller grain size and in turn smoother surface or/and reduced roughness. It should be mentioned, that tritonX-100 ($C_{14}H_{22}O(C_2H_4O)_n$) was unavoidably necessary for Sn deposition. It acts as a surfactant and greatly improves Sn layer morphology. Surface morphology of deposited Sn films without tritonX-100 is depicted in Fig. 4.13 A inset. It can be clearly seen, that without tritonX-100 Sn grew into large separate grains of various sizes and did not form a continuous layer, whereas for the films deposited at the same conditions, but with particular surfactant grains were smaller and coalesced (Fig. 4.13 B). The smoother

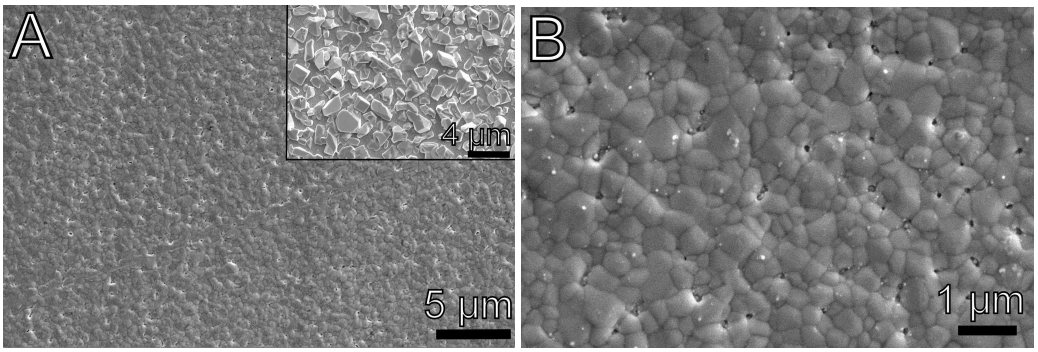

Figure 4.13: SEM micrographs of Sn surface morphology (A) large view and (B) small scale. Sn electroplated at j=4.5 mA/cm^2, flow rate=450 ml/min, electrolyte solution – MSA. Inset-Sn deposited at the same conditions without tritonX-100.

surface of Sn deposited from MSA electrolyte was also observed in the FIB made cross-section of Mo/Cu/Sn, which is depicted in Fig. 4.14. Note that Cu layer has fewer pores and is better adhered to Mo in the sample, where Sn was deposited from MSA solution (Fig. 4.14 B). It should be noted that we can not clearly distinguish bottom copper layer, indicating that interdiffusion occurred during deposition as well as after. It has been already proved that alloying of Cu and Sn starts during sequential deposition of Cu and Sn layers as well as it proceeds after deposition at room temperature [113, 114]. Because

using the MSA based solution it was possible to obtain more uniform and smoother Sn films, further in this work only particular electrolyte was used for Sn deposition in stacked layer precursor. Statistically, films deposited under potentiostatic conditions gave more reproducible results, therefore a

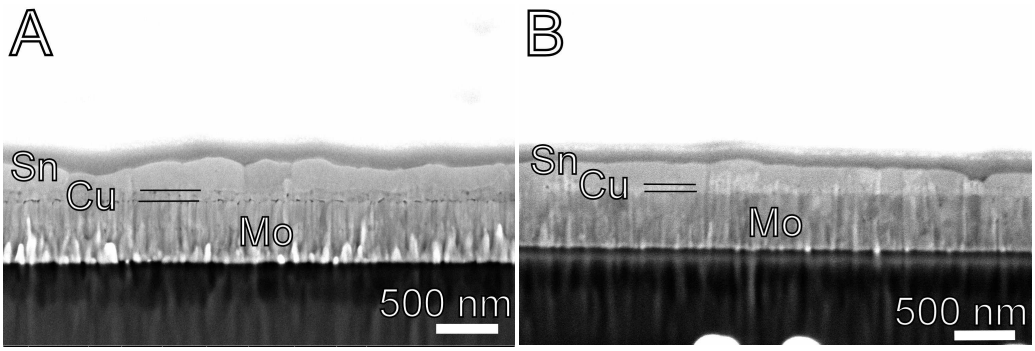

Figure 4.14: SEM images of FIB made cross-sections of Mo/Cu/Sn samples (A) Sn deposited from citrate based solution, (B) Sn deposited from MSA solution.

constant potential was applied to deposit Sn layer instead of constant current. In summary the optimal conditions for Sn deposition were as follows: MSA-based electrolyte, deposition potential in the range of -0.93 – 0.95 V vs Pt wire reference electrode and flow rate of 320-350 ml/min.

4.3.3 Zn layer

The deposition of Zn layer was the most difficult and time-consuming research step of sequential CZT electrodeposition. Overall three electrolytes were tested in this study, which are summarized in table 4.3.

Following the same procedures as for Cu and Sn deposition firstly, citrate based solution was tested. The substrate for Zn deposition was the same as for Sn i.e. Mo covered with thin (80 – 100 nm) electrochemically deposited Cu layer. Deposition of Zn from citrate solution was greatly sensitive to the solution flow rate and other deposition parameters, therefore it was difficult

Table 4.3: The composition of Zn electroplating electrolytes.

Solution name	Complexing agent	Source of Zn^{2+}	Additives
Zn-citrate	0.25 M $Na_3C_6H_5O_7$	0.034 M $ZnSO_4$	-
Zn-MSA	0.5 M CH_3SO_3H	0.2 M $ZnSO_4$	-
Commercial	Unknown	$ZnCl_2$	H_3BO_3, additives

to obtain reproducible results. The surface morphology and FIB made cross-section of Zn layer deposited at 2.3 mA/cm^2 with flow rate of 120 ml/min are depicted in the Fig. 4.15. As can be seen from Fig. 4.15 A Zn layer was composed of hexagonal plate shape grains, which is very typical for the electrochemically deposited Zn [115]. The size of the grains was less than 200 nm and coalesced forming continuous and compact film. On the other hand

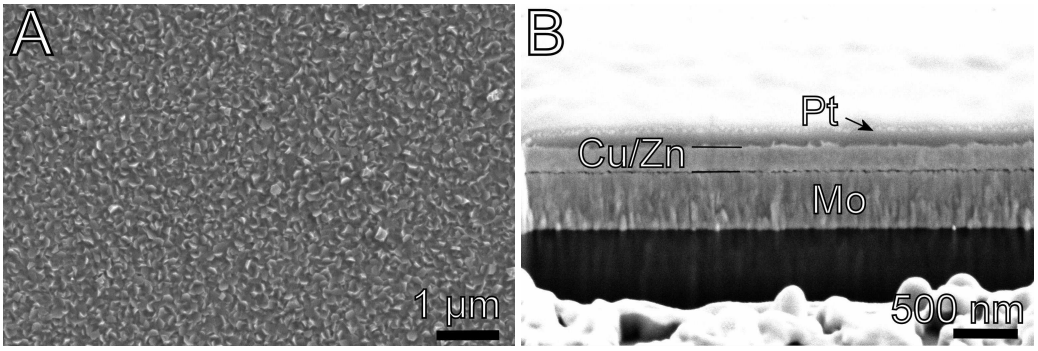

Figure 4.15: SEM micrographs of surface morphology and FIB made cross-section of Zn layer deposited from citrate solution, j =2.3 mA/cm^2, flow rate= 120 ml/min.

from Fig. 4.15 B we can conclude that Cu/Zn layer was not well adhered to the Mo substrate as we can see gap between the Mo and Cu/Zn layers. In addition, at the particular areas of electrode Cu/Zn layer completely peeled off after rising with deionized water.

Because of the great sensitivity to deposition parameters and poor reproducibility another Zn electroplating solution was tested, which was

adapted from [92]. It was MSA based solution, similar to the Sn plating but without tritonX-100. The morphology of Zn films deposited at $j = 5$ mA/cm^2 with different electrolyte flow rates is depicted in the Fig. 4.16. Morphology

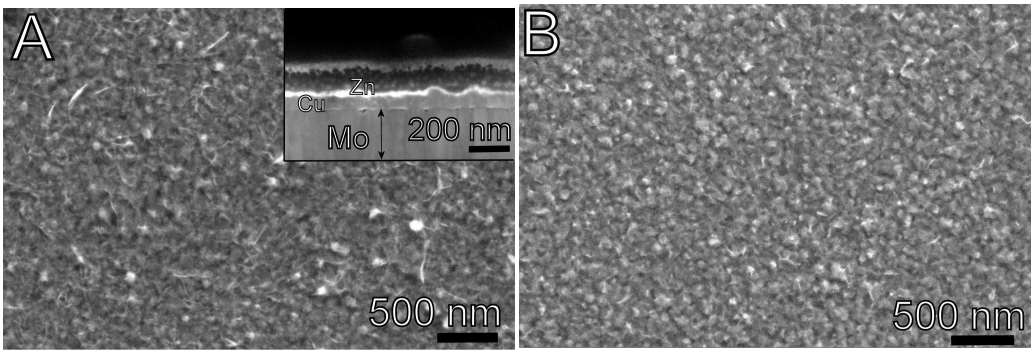

Figure 4.16: SEM images of Zn layer morphology deposited from MSA electrolyte at $j = 5$ mA/cm^2 with different flow rates: (A) 320 ml/min, (B) 40 ml/min. Inset: FIB made cross-section of Cu/Zn layer.

of deposited Zn layers was similar in both cases. The grains were closely packed and their size was uniform ~110 nm, however samples deposited with lower flow rate were more smooth (Fig. 4.16 B). Deposition was carried out for 60 s which, which would result in ~140 nm thick Zn layer, but from the FIB prepared cross-section of Mo/Cu/Zn sample (Fig. 4.16 A inset) the thickness of Zn film (inset: thin bright layer) was around 15-30 nm thick. It means that the efficiency of the deposition was only ~17%. This observation implies that intensive hydrogen evolution occurred during deposition and also was the cause of the layer peel off at the corners of the electrode. These results do not coincide with the ones obtained in [93] probably because of the different experimental setup (much larger electrolytic cell volume and usage of pedal stirring) and/or not all composition details are given, for example additives. After successive Zn electrodepositions from MSA solution it was found out that in order to obtain layers of uniform morphology, low flow rates had to be

used (20-40 ml/min) which would simulate classical electrodeposition without stirring though in small volume.

Because of the unsatisfactory reproducibility and particular optimal deposition condition third Zn plating solution was tested. The Zn plating solution, specially designed for thin film deposition was purchased from "Chromtech" company. The exact composition of the solution was not disclosed. It was stated that under galvanostatic deposition of Zn film occurs in the range of current densities 2-40 mA/cm^2 without major change in morphology, though their experiments were performed on stainless steel. The morphology of Zn films deposited from commercial electrolyte at different current densities using flow cell is presented in Fig. 4.17. Flow rate of electrolyte was 320 ml/min and the passed charge quantity for both samples was kept the same. Visually both samples appeared similar, grey-silver colour with mirror reflectivity, however from Fig. 4.17 it is evident that larger grains were in the film, deposited at 3 mA/cm^2 current density. This tendency

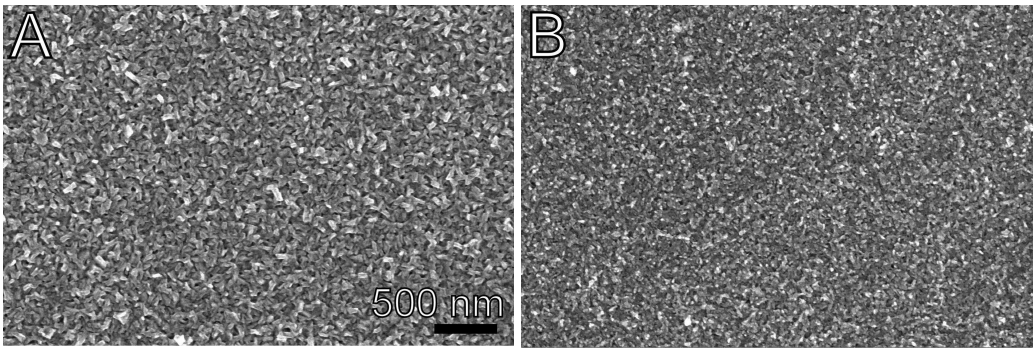

Figure 4.17: SEM micrographs of Zn layer deposited from commercial electrolyte (A) at 3 mA/cm^2 and (B) 30 mA/cm^2, flow rate 320 ml/min.

coincides with the one, observed during Cu deposition and was explained in the subsection 3.3. In Fig. 4.17 A layer comprised small (~100 nm) elongated grains and was compact, however small gaps between the grains were observed, whereas in Fig. 4.17 B zinc film composed of nanometer-scale

grains (~50 nm) was more compact and less voids were observed. It should be noted that the coverage of the electrode was excellent and no layer peel off occurred. The higher current density was used, the shorter was duration of electrochemical deposition and more uniform in chemical composition layers were achieved. However, films deposited at j > 20 mA/cm^2 were porous because of the intensive hydrogen evolution, therefore as an optimal current density for Zn deposition 20 mA/cm^2 was chosen.

In summary, the most suitable conditions for Zn electrodeposition were: commercial electrolyte, current density of 20 mA/cm^2, flow rate of 300-350 ml/min.

4.3.4 Stacked layer deposition

The order of the sequential deposition of metal layers is important for forming high quality Cu-Zn-Sn precursor. Firstly, the electrodeposited Cu layer forms best cohesion to the Mo among other precursor metals and is always deposited as a first layer [68, 90, 92, 94,]. Secondly, metals should be deposited in such order that metal with most negative deposition potential would be on top i.e. Cu (E^0 =+0.34 V) / Sn (E^0 =-0.13 V)/ Zn (E^0 =-0.76 V). In this case during deposition of successive layers the oxidation of already deposited metals is avoided. Thus, theoretically the best deposition order for electrochemically deposited metals would be Cu/Sn/Zn. There are many reported publications, where particular deposition order was implemented in forming Cu-Zn-Sn precursor [68, 92-94].

Generally, keeping in mind that Cu has to be deposited as a first layer overall there are two possible deposition sequences: Cu/Sn/Zn and Cu/Zn/Sn which were both tested in this work. In order to achieve better adherence between each of the layers, Cu/Sn/Cu/Zn precursor sequence was also tested.

Surface morphology and FIB made cross-section of electrodeposited Cu/Sn/Zn precursor is depicted in Fig. 4.18. As can be seen in Fig. 4.18 A in the case of Cu/Sn/Zn the coverage of Zn layer is very poor. Bright spots and areas, which represent Zn aggregates, are non-uniformly distributed and do not form a continuous layer. This effect has also been observed by Scragg [91]. Presumably, it is related to the nature of Sn electroplating solution, because using other than MSA based solutions, this effect was not observed. In the

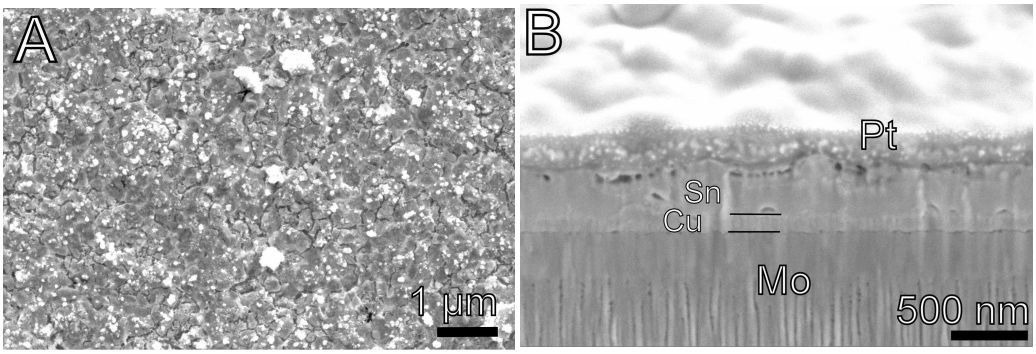

Figure 4.18: SEM micrographs of Cu/Sn/Zn sample (A) surface morphology, (B) FIB made cross-section. Cu and Sn deposited from optimal electrolytes (table 2.1) at 5 mA/cm^2 flow rate 400 ml/min, Zn from MSA (table 4.3) solution at 2.5 mA/cm^2, flow rate 300 ml/min.

cross-section view (Fig. 4.18 B) we can observe bottom Cu layer and rough Sn layer, whereas Zn layer is not clearly seen. The EDX analysis also showed very uneven distribution of Zn content and the absolute value in at.% was 10 times less than expected. Because of the reasons indicated above, particular deposition sequence was disregarded.

Another possible deposition sequence Cu/Zn/Sn was tested as well. Similar approach was also used in several works, for example Lehner et al. obtained good results by depositing Cu-Zn layer and pure Sn on the top [116]. Furthermore, Ahmed et al. stated that they have achieved high efficiency CZTSe solar cells prepared from either precursor Cu/Sn/Zn or Cu/Zn/Sn [92].

Two cases were investigated for the formation of Cu/Zn/Sn precursor. Cu and Sn were deposited under optimal conditions, whereas Zn layer was deposited firstly from MSA solution and in other case from commercial electrolyte. The surface morphology and FIB prepared cross-section of both samples are depicted in Fig. 4.19. The sample, where Zn was deposited from MSA solution is presented in Fig. 4.19 A, C and from commercial electrolyte in Fig. 4.19 B, D. Firstly, we can clearly see the difference in Sn morphology: in the case where Zn was deposited from MSA solution, Sn film is not perfectly continuous, in some areas grains are not fully coalesced (Fig. 4.19 A) meanwhile in the case where Zn was deposited from commercial electrolyte top Sn layer is very compact, comprised of various size refine grains (Fig. 4.19 B). The EDX analysis revealed that Zn content in the films (where Zn deposited

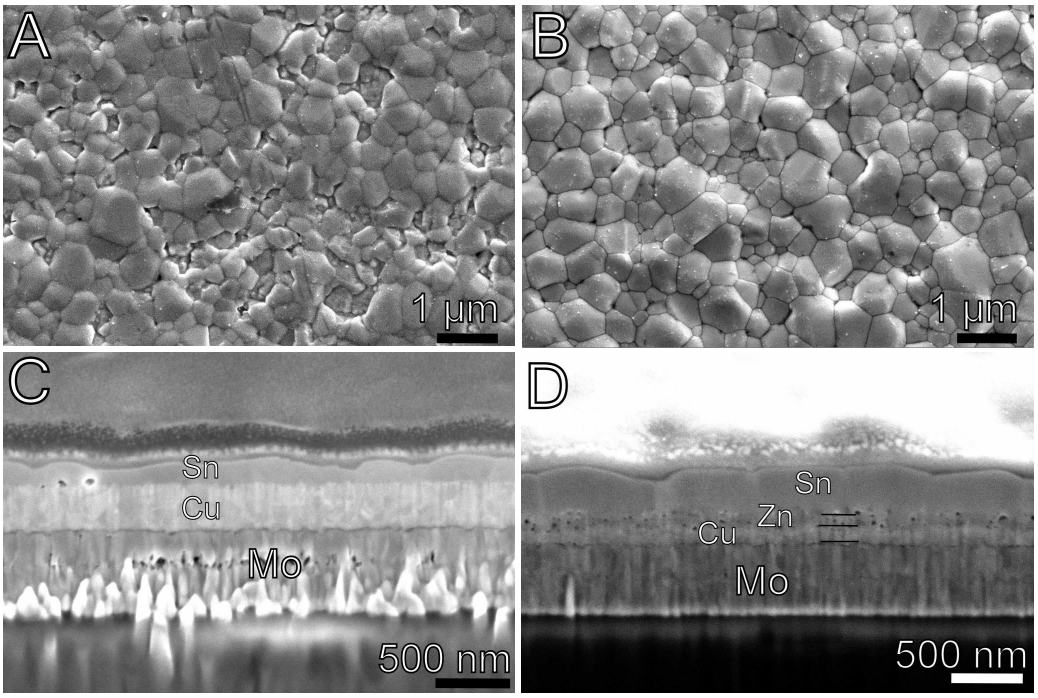

Figure 4.19: SEM micrographs of Cu/Zn/Sn surface morphology and FIB prepared cross-section (A) Zn deposited from MSA solution (B) Zn deposited from commercial electrolyte. Cu and Sn deposited at 5 mA/cm^2, flow rate 400 ml/min.

from commercial solution) was only about 5 at.%, i.e. five times less than expected. To identify the reason of such low Zn content, cross-sections of Cu/Zn/Sn layers have been investigated. In the sample, where Zn was deposited from MSA solution, no Zn layer was observed (Fig. 4.19 C), whereas in Fig.4.19 D we can observe small pores between Cu and Sn layers. The latter is result of the hydrogen evolution during Zn deposition. The expected concentration value of Zn in the particular film was 38 at.%, meanwhile measured one was only 5 at.%. Albeit deposition time of Zn was increased the desired composition of film was not achieved. Eventually, it was concluded that dissolution of Zn layer occured during Sn deposition. The pH of Sn MSA solution was ~1.0 indicating strong acidic environment. The fine-grained Zn films are active and quickly dissolve in the acid solution, therefore, certain sequence of deposition was disregarded as well.

4.3.5 Deposition of Cu/Sn/Cu/Zn

As has been demonstrated above, using suitable Cu, Sn, Zn electroplating solutions and electrodeposition system with a flow cell, compact, uniform with targeted composition Cu/Sn/Zn or Cu/Zn/Sn precursors could not be achieved. As it has been already shown, the deposition of Zn directly on top of Sn layer is difficult, therefore the order of precursor metals was changed to Cu/Sn/Cu/Zn. This solution was firstly suggested by Scragg [91] and was tested in this study as well. To begin with, the Cu/Sn/Cu films were investigated. The morphology and FIB made cross-section of Cu/Sn/Cu are depicted in Fig. 4.20. The deposition conditions were optimal for both metals, except for depositing second Cu layer initial overvoltage of -1.25 V was applied in order to obtain better coverage. As can be seen from Fig. 4.20 A the morphology of top Cu layer replicates Sn layer. Using in this study presented conditions, electrodeposited Cu is composed of much smaller grains than that

of Sn, naturally, thin Cu layer reflects more rough Sn layer. From visual inspection layers appeared uniform, bright brown colour with mirror reflectivity (Fig. 4.21). In the cross-section view (Fig. 4.20 B) we can distinguish thin (~40 nm) Cu top layer, however bottom Cu layer was already merged

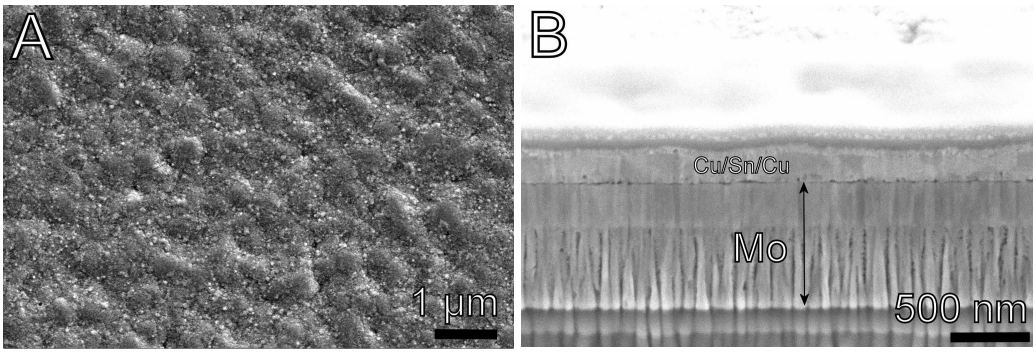

Figure 4.20: SEM micrographs of Cu/Sn/Cu sample (A) surface morphology (B) FIB prepared cross-section. First Cu layer deposited at 5 mA/cm^2, flow rate 400, Sn deposited at -0.9 V, flow rate 330 ml/min, second Cu layer at -0.94 V, flow rate 400 ml/min with initial pulse at -1.25 V for 2s.

with Sn. This indicates a fast interdiffusion of Cu and Sn layer during electrodeposition as has been observed in Cu/Sn stacked layer deposition.

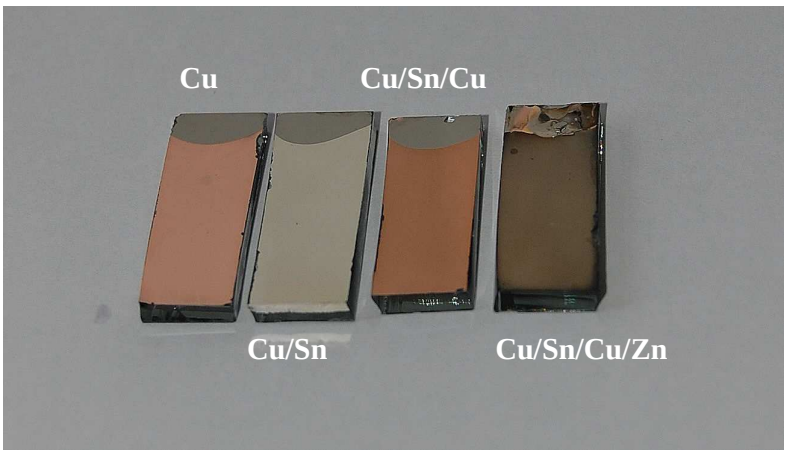

Figure 4.21: Photograph of Cu/Sn/Cu/Zn precursor after each layer deposition. Electrode dimensions were 1x2.5 cm^2.

Darker and brighter areas in the SEM image of Cu/Sn/Cu cross-section were also observed which were associated presumably with pure Sn and Cu-Sn phases, respectively.

Zn was deposited on top of Cu/Sn/Cu layers from the commercial electrolyte. The coverage was excellent and at the end films appeared bright-grey colour had mirror reflectivity. The optical images of the Cu/Sn/Cu/Zn precursor after each layer deposition are depicted in Fig. 4.21.

The SEM images of surface morphology and FIB made cross-section view of typical Cu/Sn/Cu/Zn precursors are depicted in Fig. 4.22. Surface morphology (Fig. 4.22 A) was very similar to the one in Fig. 4.17 B, which was expected result, because deposition of Zn on Mo/Cu and Mo/Cu/Sn/Cu should be the same. Note that Sn layer morphology features are no more observable, as it was in Cu/Sn/Cu case albeit Zn layer is also composed of small grains. The reason could be associated to the additives (brighteners, levellers) which are present in the commercial Zn electrolyte and tend to level Zn film. In Fig. 4.22 B we can clearly distinguish Zn top layer, it is well adhered to the Cu/Sn/Cu, however it is more porous than other layers because of the hydrogen

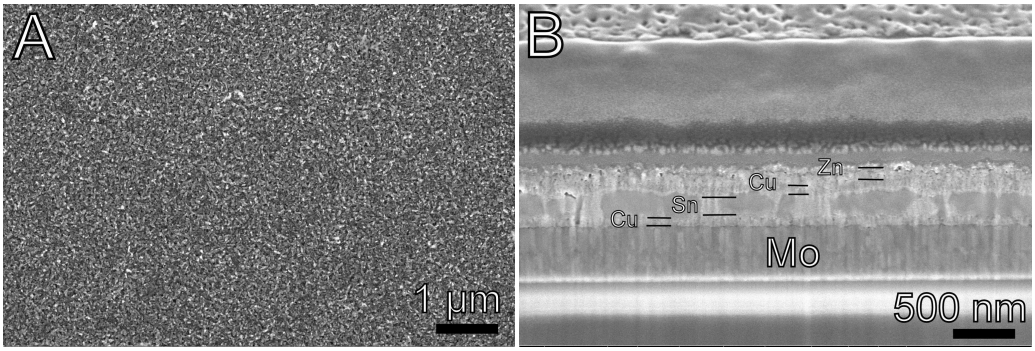

Figure 4.22: SEM micrographs of Cu/Sn/Cu/Zn precursor (A) surface morphology (B) cross-section view. First Cu layer deposited at -0.97 V, flow rate 400 ml/min, Sn at -0.94 V, flow rate 350 ml/min, second Cu at -0.97 V with initial pulse at -1.25 V for 5s, flow rate 400 ml/min and Zn deposited at j =20 mA/cm^2, flow rate 320 ml/min.

evolution reaction during Zn deposition. In general, as can be seen in SEM images, Cu/Sn/Cu/Zn films are uniform in thickness, compact and well adhered to the Mo substrate.

In summary, implementing Cu/Sn/Cu/Zn deposition sequence high quality Cu-Sn-Zn precursor has been obtained using in this study presented new electrochemical deposition setup with flow cell and optimized deposition parameters. Thus, further in this work, for the stacked layer approach only Cu/Sn/Cu/Zn precursors were used for selenization.

4.3.6 The uniformity of Cu/Sn/Cu/Zn films

In order to achieve perfect uniformity of the Cu/Sn/Cu/Zn layers deposition conditions especially flow velocity of solution have to be the same at all points of the electrode. The driving force of electrolyte flow in electrochemical flow cell is peristaltic pump. It allows precise control of solution flow rate and what is very important to avoid direct pump contact with electrolyte. Because of the working design of peristaltic pump, flow is not continuous but rather impulsive; this of course causes inhomogeneous solution velocity over electrode surface. In order to avoid the latter effect, buffer volume was used between peristaltic pump and flow cell. Principally, solution was transported to buffer volume, which was held higher than cell, and then led to freely flow into the electrochemical cell. In this manner, impulsive flow was directed to the buffer volume from where a constant and continuous flow was provided to the cell. On the other hand, cell chamber is not exactly channel-like. The dimensions of cell chamber are 5 x 1.5 x 1.5 cm^3, thus firstly solution fills up all chamber volume and then flows out. In this case flow velocity at the inlet and outlet of electrochemical cell is not exactly the same and could contribute to the deposition rate of Cu, Sn or Zn. The cell design as well as experimental

setup was constantly improved in order to achieve as homogenous flow as possible.

The uniformity of composition and thickness was estimated by EDX spectroscopy. All EDX measurements were done under exactly the same configuration i.e. magnification, accelerating voltage, beam current and sample distance from EDX detector. Thickness was evaluated indirectly assuming lower Mo intensity in thicker sample places, whereas composition was measured in weight and atomic %. To get correct results for the each element contribution to the composition, normalization function was omitted. In this manner we can clearly identify distribution of each element independently. When concentration is measured in atomic percentage and normalized to 100%, supposing that one element is constant over all measured points and another is not, the results would show that both elements are not equally distributed.

From previous results (not shown here) we assumed that Cu deposits rather uniformly, thus the deposition conditions of Zn and Sn was varied. The composition of two samples deposited under different conditions is presented in the table 4.4. All layers were deposited under the optimal

Table 4.4: Composition of Cu/Sn/Cu/Zn precursor metals in weight% and atomic%.

CSCZ18 S_{Sn} = 350 ml/min; j_{Zn} = 2 mA/cm^2				CSCZ19 S_{Sn} = 420 ml/min; j_{Zn} = 4 mA/cm^2		
Element	Top	Middle	Bottom	Top	Middle	Bottom
Cu	29 (48)	29 (46)	27 (39)	27 (44)	27 (44)	27 (41)
Zn	17 (26)	18 (28)	29 (40)	19 (30)	20 (31)	25 (37)
Sn	30 (26)	32 (27)	28 (21)	31 (27)	30 (25)	28 (23)
Mo	13	11	7	12	12	10

conditions, except that flow rate for Sn deposition and current density for Zn deposition was 350 ml/min, 2 mA/cm^2 and 420 ml/min, 4 mA/cm^2 for CSCZ18 and CSCZ19, respectively. The top, middle and bottom locations represent the measured points on the sample. Top is located at inlet of flow cell and bottom closer to the outlet. Firstly, Cu layer as was expected is deposited uniformly over all electrode area. Although Cu layers were deposited at the same conditions, a slight variation in Cu concentration can be seen in sample CSCZ18, which could be associated with slightly different experimental conditions (room temperature, age of electrolyte and etc.) Content of Sn depends on the position of electrode. It is a bit lower at the bottom and higher at the top. In the sample, deposited at higher flow rate (450 ml/min) Sn content steadily increases from bottom to top most likely because of gradual increase of flow velocity. The Zn content as can bee seen in table 4.4 greatly depends on the electrode position. Between top and middle positions the concentration of Zn varies very slightly ~1 wt. %, whereas at the bottom Zn content is much higher. Zn content decreases from bottom to top and this tendency is observed in both samples. However, it should be noted that magnitude of Zn content difference at bottom and top positions is different for each sample. In the sample, where Zn was deposited at lower current density (2 mA/cm^2), the difference in Zn content from bottom and top position is higher, than in sample deposited at 4 mA/cm^2. Naturally, the time required to deposit appropriate amount of Zn for CSCZ19 is twice as shorter as for CSCZ18. Thus, we can conclude, that increasing Zn deposition current density (decreasing deposition duration) we can obtain more uniform Zn layers. Considering film thickness, we would expect layer to be thicker at the bottom as higher content of Zn was observed at the bottom and approximately the same at the middle and top positions. From the amount of Mo this tendency was validated as can be seen in table 4.4 Mo row.

The targeted composition of Cu-Zn-Sn precursor is Cu-poor and Zn-rich with a Cu/(Zn+Sn) ratio 0.8 – 0.9 and Zn/Sn ratio 1.2. That would be 44-46 at.% of Cu, 28-30 at.% of Zn and 23-25 at% of Sn. In the table 4.4 concentration of Cu, Zn and Sn in at.% are presented in brackets and coloured in red. The targeted composition was achieved in the sample CSCZ19 at the top and middle positions, however because of the preferable deposition of Zn, composition was strongly deviated at the bottom.

Further investigation of Zn content distribution revealed that the higher the current density was used, the smaller Zn content difference between top and bottom positions was observed. 20 mA/cm^2 was chosen as an optimal current density, because higher current density led to higher deposition potential as a consequence more intensive hydrogen evolution. Sn deposition parameters were adjusted as well and optimal flow rate was found to be 400 ml/min. Schematic 9 point EDX mapping of Cu/Sn/Cu/Zn precursor deposited under optimal conditions is presented in table 4.5. As can be seen Cu and Sn

Table 4.5: The atomic concentration and corresponding Cu/(Zn+Sn), Zn/Sn ratios of Cu/Sn/Cu/Zn precursor at 9 positions, which are schematically indicated on the right of table. Composition was measured by EDX and arrows indicate the direction of the electrolyte flow.

Position	Cu, wt%	Zn, wt%	Sn, wt%	Cu/(Zn+Sn)	Zn/Sn
1	33	24	32	0.83	1.41
2	32	21	32	0.88	1.26
3	31	24	31	0.80	1.47
4	33	23	32	0.83	1.38
5	32	20	31	0.91	1.22
6	30	22	31	0.82	1.37
7	31	25	32	0.77	1.46
8	29	19	30	0.87	1.29
9	31	26	31	0.77	1.61

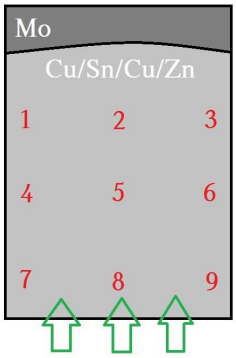

was deposited uniformly over all electrode area 31.3±1.32 wt% and 31.3±0.7 wt%, respectively. In the centre of the sample a slightly increasing content of all metals was observed from top to bottom. This reveals that solution velocity gradient was highest in the centre of the sample rather than at the edges. Note, that Zn is most unevenly deposited among other metals (22.7±2.35 wt%). The difference of Zn content in the centre and at the edges of the sample is the highest one. This could be related to the edge effects at the electrode. It is well-known that between two similar size and shape plates electric field density is the highest at the edges of the plates and consequently the potential. The deposition of Zn occurs at the region, where small changes in potential results in significant changes in current. Therefore, the deposited Zn content was sensitive to the potential distribution over electrode and more Zn was deposited at the edges than in the centre of the sample, as can be seen in table 4.5. The calculated Cu/(Zn+Sn) and Zn/Sn ratios indicate that uniformity along (in the flow direction) the Mo electrode is fairly good, however the ratios strongly fluctuate in the direction perpendicular to flow direction. As we can see the targeted optimal Cu/Sn/Cu/Zn composition (Cu/(Zn+Sn)=0.8-0.9, Zn/Sn=1.2-1.3) is achieved in the centre of electrode, but because of preferable Zn deposition it is more Zn-rich at the electrode edges.

In summary, we have found out that uniformity of Sn is little sensitive to flow rate in the region of 350 – 420 ml/min. It was shown that all metal content decreases from bottom to top because of the flow velocity gradient. The uniformity of Zn depends on the current density and flow rate. The higher current density was applied the more uniform Zn layer was deposited. However, edge effects had a significant effect on Zn content and enhanced content of Zn was found at the edges of Cu/Sn/Cu/Zn precursor.

4.4 Preliminary annealing of Cu-Zn-Sn precursor

Preliminary annealing (soft-annealing) of Cu-Zn-Sn precursor is usually applied before selenization. The role of soft-annealing has not been unambiguously explained, though it is commonly applied in CZTSe(S) technology, especially for sequentially deposited precursor [68, 91-94]. According to our results, which will be described in section 4.5, the elimination of pure Sn phase in preliminary annealed CZT precursor improves CZTSe morphology and consequently solar cell performance.

In the literature the preliminary annealing temperature varies in the range of 210 – 375 °C and duration from 20 to 150 min. It is evident that in this temperature range films are homogenized and the alloying of metals is intensified. All reported studies on soft-annealing effect on selenization unanimously stated that this step has improved the final CZTSe(S) solar cell performance. What is more, in this study preliminary annealing was performed under H_2+Ar atmosphere, therefore the organic compounds that could have been incorporated during electrochemical deposition presumably were reduced to volatile compounds and removed from CZT precursor.

Thus, we have investigated the effect of soft-annealing on CZT precursor phase composition and morphology. The formation of intermetallic phases and morphology of co-electroplated and sequentially deposited CZT precursors were examined and will be presented in the following subsections.

4.4.1 Preliminary annealing of co-deposited Cu-Zn-Sn precursor

Firstly, the examination of as-deposited CZT precursor was carried out. The XRD pattern of co-deposited Cu-poor and Zn-rich CZT precursor is depicted in Fig. 4.23. CALSA analyzer was used in the measurements in order to accurately identify phases with similar lattice constants. The co-electroplated

precursor contained at least four metallic phases: hexagonal η-$Cu_{6.26}Sn_5$ (# 00-047-1575), tetragonal Sn (# 00-004-0673), cubic γ-Cu_5Zn_8 (# 00-025-1228), and cubic δ- $Cu_{40,5}Sn_{11}$ phase (# 01-071-0121). These results slightly differ from the ones reported in the studies of electrochemically co-deposited CZT films [81, 82, 85]. Because it is very difficult in certain cases even impossible to distinguish diffraction peaks of different intermetallic phases, they were predefined ambiguously. For example, monoclinic η´-Cu_6Sn_5 was reported [117], because most intensive XRD peaks of η-$Cu_{6.26}Sn_5$ and η´-Cu_6Sn_5 overlaps and very precise measurements are required to separate them. On the other hand, according to the equilibrium phase diagram of Cu-Sn system namely the hexagonal η phase is more characteristic at Sn concentrations > 25.3 at.% and the monoclinic η´-Cu_6Sn_5 exists only when the amount of tin in the Cu-Sn alloy is in range from 43.4 to 44.3 at.% [118]. Furthermore, our precise measurements indicated the existence of η-$Cu_{6.26}Sn_5$ phase only. Therefore, the formation of η´-Cu_6Sn_5 phase was disregarded in the as-deposited CZT precursor. Phase composition of as-deposited CZT precursor depended on the

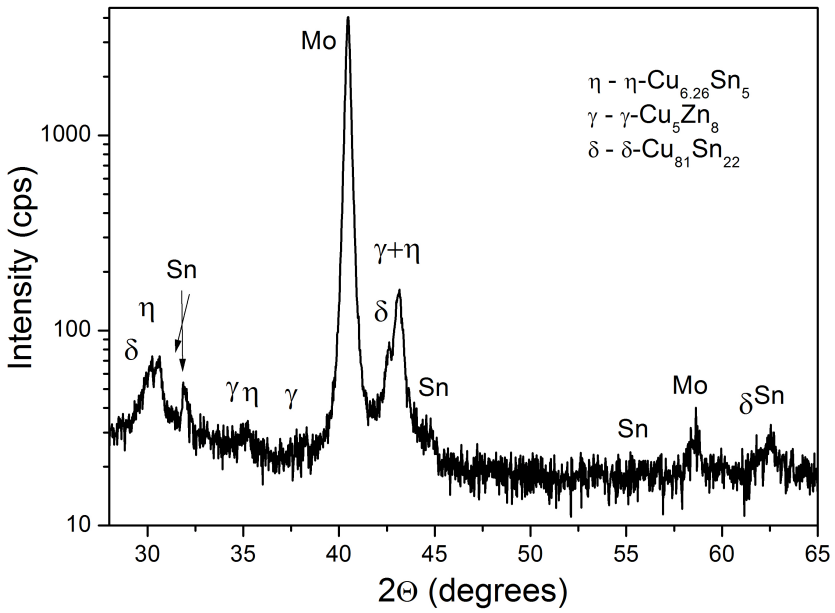

Figure 4.23: XRD pattern of as-deposited CZT precursor with Cu/(Zn+Sn)=0.89 and Zn/Sn=1.16.

Sn concentration in the films. Samples, in which Zn/Sn ratio was < 1.0 contained all aforementioned intermetallic phases and in addition hexagonal ε-Cu_3Sn phase (a = 2.76, c = 4.316 Å) was present. It should be mentioned that in Zn-rich films diffraction peaks of γ-Cu_5Zn_8 and pure Sn were more intensive than in Zn-poor. Latter indicates that in the Zn-rich films larger quantity of Cu was used up for the formation of γ-Cu_5Zn_8 phase than for those of Cu-Sn.

The kinetics of intermetallic phases was investigated in the temperature range from 200 °C to 230 °C under He atmosphere. The fragment of XRD pattern of Cu-poor and Zn-rich CZT precursor heated from 200 °C to 230 °C is depicted in Fig. 4.24. Sample was maintained for 30 min at each temperature step before XRD measurements started. In general, there was no change in phase composition from 200 °C to 220 °C, only the sharpness of XRD peaks of already existing intermetallic phases increased. As can be seen in Fig. 4.24 the XRD peak of pure Sn decreased as temperature was increased and at 230 °C it disappeared indicating that all Sn has melted. After sample was quenched to

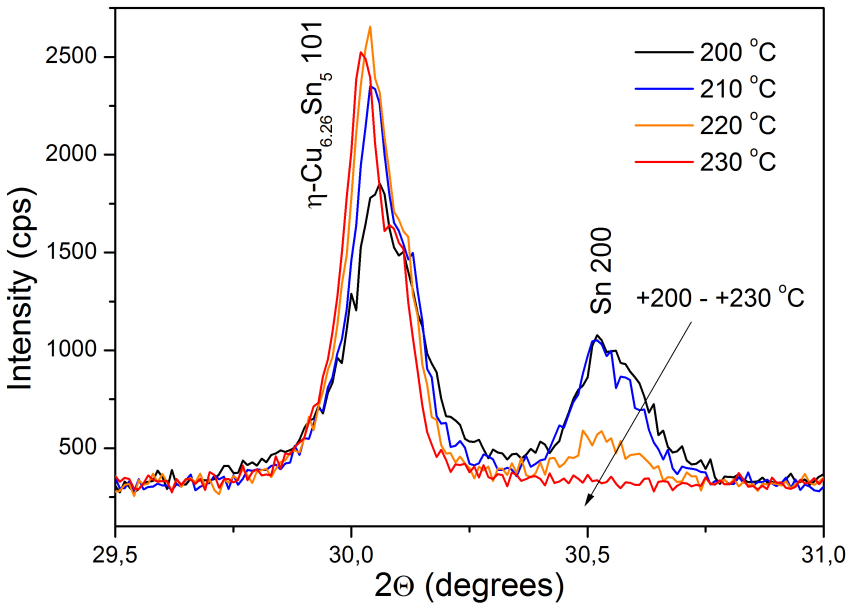

Figure 4.24: Fragments of XRD patterns measured during preliminary annealing of CZT precursor at temperatures of: 200, 210, 220, and 230 °C. The arrow shows direction of increase in temperature. Bragg-Brentano geometry.

26 °C, XRD pattern was recorded again and is depicted in Fig. 4.25. XRD peaks of pure Sn were observed, implying that melted Sn crystallised into pure Sn phase during quenching. After detailed calculations a slight expansion and shrink of γ-Cu_5Zn_8 and η-$Cu_{6.26}Sn_5$ lattice constants were observed, respectively. Expansion was associated with the formation of substitution solid solution of tin in the γ-Cu_5Zn_8, whereas shrinkage of η-$Cu_{6.26}Sn_5$ lattice constants was related to the partial replacement of Sn atoms by those of Zn or Cu.

After preliminary annealing at T < 300 °C, full alloying of metals was not achieved, therefore samples were preheated at more elevated temperature. The XRD pattern of CZT layer annealed at 350 °C under He atmosphere for 30 min is depicted in Fig. 4.26. The increase in sharpness of γ-Cu_5Zn_8 and η-$Cu_{6.26}Sn_5$ XRD peaks was observed and pure Sn phase was no more present. The calculated lattice parameters of two remaining intermetallic phases were

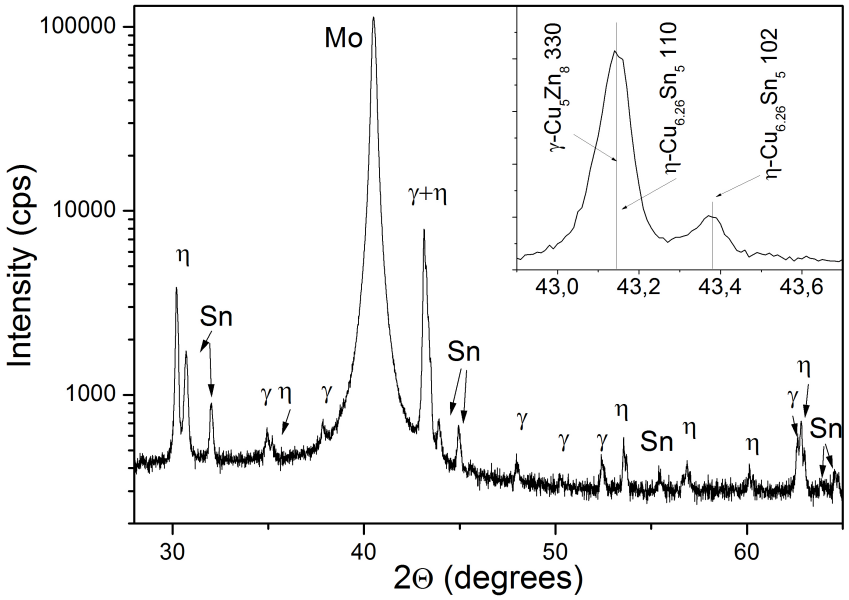

Figure 4.25: The XRD pattern of CZT precursor film with Cu/(Zn+Sn) = 0.77 and Zn/Sn = 1.21 after the preliminary annealing at temperature of 230 °C (Bragg-Brentano geometry). The inset shows the fragment of the pattern of the same specimen measured with CALSA analyzer.

significantly increased. This was associated with the formation of Sn solid solution in both of γ-Cu_5Zn_8 and η-$Cu_{6.26}Sn_5$ phases. Albeit homogenization of CZT precursor was achieved after soft-annealing at 350 °C, after two days repeated XRD measurements of the same sample revealed that pure Sn phase has emerged. This was caused by a segregation of Sn, which took place during decomposition of saturated solid solutions.

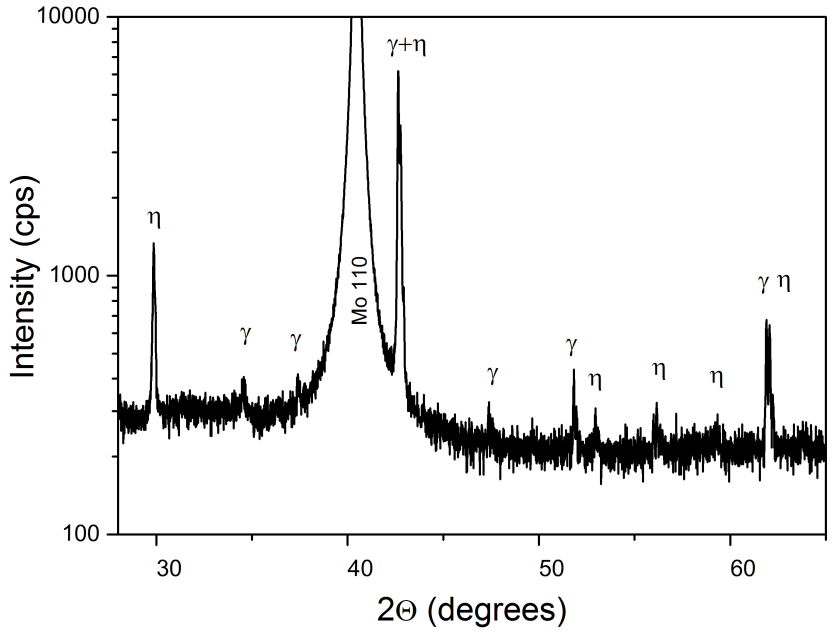

Figure 4.26: The XRD pattern of CZT precursor film with Cu/(Zn+Sn) = 0.82 and Zn/Sn = 0.89 after the preliminary annealing at temperature of 350 °C. Bragg-Brentano geometry.

In summary, these results show that it is important to minimize time between soft-annealing and selenization steps, because of the Sn segregation. Higher than 300 °C temperature is required in order to alloy Sn with other intermetallic phases.

4.4.2 Preliminary annealing of stacked layer precursor

Soft-annealing for sequentially deposited Cu-Zn-Sn precursor is even more crucial than for co-deposited. XRD pattern of as-deposited stacked Cu/Sn/Cu/Zn precursor is presented in Fig. 4.27. Sample contained 3 phases: hexagonal η-$Cu_{6.26}Sn_5$ (# 00-047-1575), tetragonal Sn (# 00-004-0673) and hexagonal ε-$CuZn_5$ (a=2.758, c=4.294 Å) phase. The later intermetallic compound is characteristic in electrochemically deposited Zn films on Cu substrate [119]. During sequential deposition each metal is deposited in the metallic form, however we do observe neither Cu nor Zn XRD peaks of pure metallic phase. Instead, Cu-Sn and Cu-Zn alloys were detected, meaning all Cu and Zn was consumed to form intermetallic compounds. These results reveal that fast interdiffusion between layers occurs during and after the deposition, as has been already assumed from SEM cross-section images (Fig. 4.20).

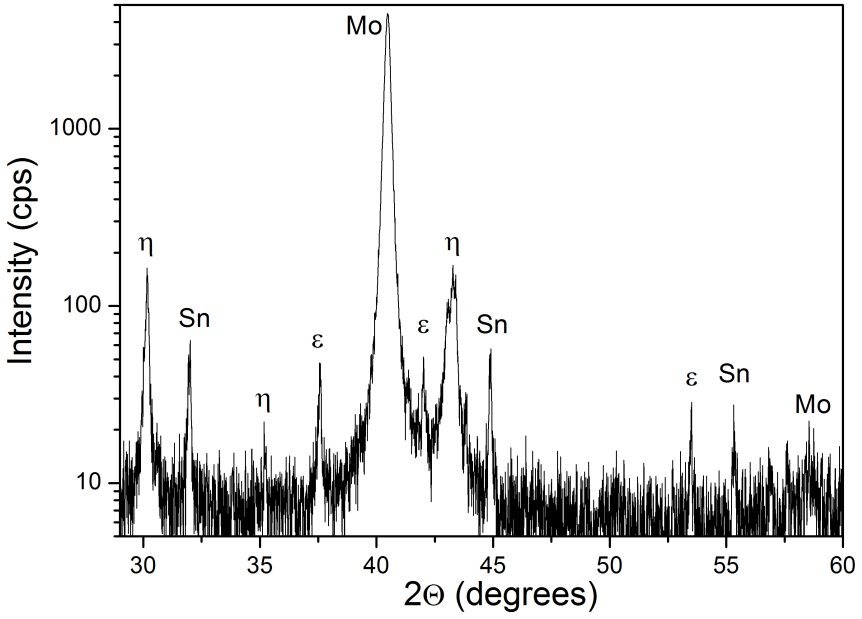

Figure 4.27: XRD pattern of as-deposited Cu/Sn/Cu/Zn precursor with Cu/(Zn+Sn)=0.78 and Zn/Sn=1.33.

Cu/Sn/Cu/Zn precursors were soft-annealed in the temperature range from 230 to 350 °C. The formation of hemisphere shape structures (see Fig. 4.30 A inset) and peeling off of the film were observed in samples preheated at 350 °C for 30 min with a heating rate of 20 °C/min. Latter may have been caused by stresses in the film due to fast grain growth and different thermal expansion coefficients of the metals. Thus, precursors were preheated at lower temperature and with slower heating rate. The fragments of XRD pattern of Cu/Sn/Cu/Zn precursor preheated at 250 °C and 310 °C are presented in Fig. 4.28. It should be mentioned that albeit γ-Cu_5Zn_8 phase was not observed in as-deposited Cu/Sn/Cu/Zn films, it was detected after soft annealing. As temperature and process time were increased the sharpness of

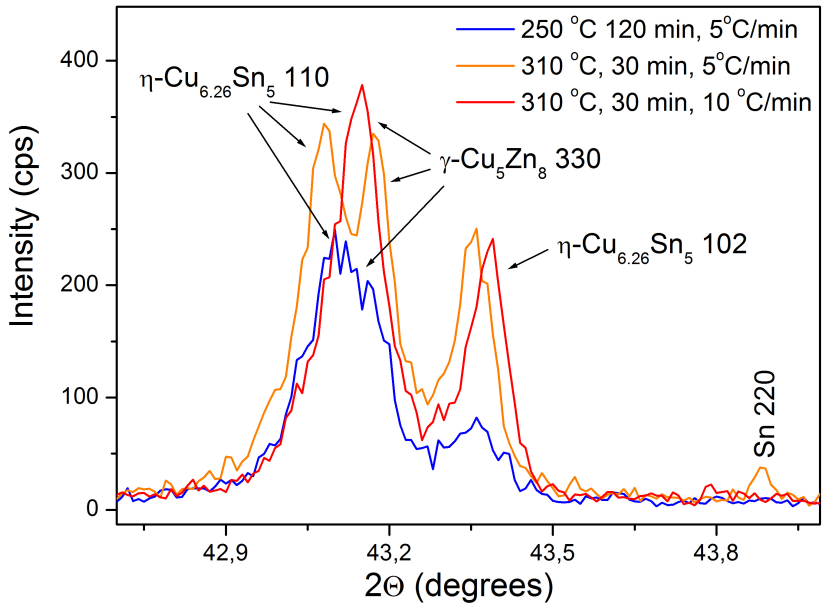

Figure 4.28: Fragment of XRD pattern of Cu/Sn/Cu/Zn precursor pre-heated at different temperatures.

XRD peaks of γ-Cu_5Zn_8 and η-$Cu_{6.26}Sn_5$ phases increased, indicating progressive grain growth. It should be noted that defining factor for large grains was heating temperature rather than duration. At all heating temperatures calculated lattice constant of γ-Cu_5Zn_8 was larger than that of

equilibrium (# 00-025-1228) indicating lattice expansion, whereas for η-$Cu_{6.26}Sn_5$ smaller than (# 00-047-1575) implying lattice has shrunk. The least discrepancy in lattice constants between annealed and equilibrium γ-Cu_5Zn_8 and η-$Cu_{6.26}Sn_5$ phases were observed in the sample, heated at 310 °C with 5 °C/min ramping rate. The expansion of γ-Cu_5Zn_8 lattice could be related to the formation of substitution solid solution of tin in γ-Cu_5Zn_8 as in co-electroplated precursor. The shrinkage of η-$Cu_{6.26}Sn_5$ lattice is associated with partial replacement of Sn atoms by those of Cu or Zn. In contrast to co-deposited precursor, where lattice constants of both γ-Cu_5Zn_8 and η-$Cu_{6.26}Sn_5$ have significantly increased after annealing at temperatures above 300 °C indicating the formation of Sn solid solution in both phases.

Pure Sn phase was detected in the sample annealed at 310 °C with 5 °C/min rate, meaning Sn has segregated, meanwhile no pure Sn was present after annealing at the same temperature, but with higher heating rate. As has been observed for co-deposited CZT precursor, where right after soft-annealing pure Sn phase was not detected, but in couple days it has emerged does not account for particular case. The time difference between preheating and XRD measurements of sample annealed at 310 °C with 10 °C/min heating rate was 14 days. Composition of both samples was very similar i.e. Cu/(Zn+Sn) ~0.85 and Zn/Sn ~1.35 so it does not have an impact of Sn segregation. The possible explanation of observed discrepancy could be related to the heating rate and the formation of tin solid solution. The largest expansion of γ-Cu_5Zn_8 lattice of samples considered in this section was in the sample annealed at 310 °C with heating rate of 10 °C/min, meaning high amount of tin was dissolved in γ phase. As for the sample preheated at 310 °C with 5 °C/min heating rate, expansion of γ-Cu_5Zn_8 lattice was the smallest one, meaning little amount of tin was present in γ phase. Longer preheating duration could have led to the formation of saturated tin solid solution in γ-

Cu_5Zn_8 phase. At room temperature, the decomposition of unstable saturated Sn solid solution occurred and segregated in the form of whiskers. Therefore, we detected the pure Sn phase and the calculated lattice constant of γ was least expanded.

4.4.3 The morphology of preliminary annealed Cu-Zn-Sn films

After preheating of CZT precursor surface morphology was dependent on heating temperature. SEM micrographs of soft-annealed Cu-Zn-Sn and Cu/Sn/Cu/Zn surface morphology are depicted in Fig. 4.29.At low temperature

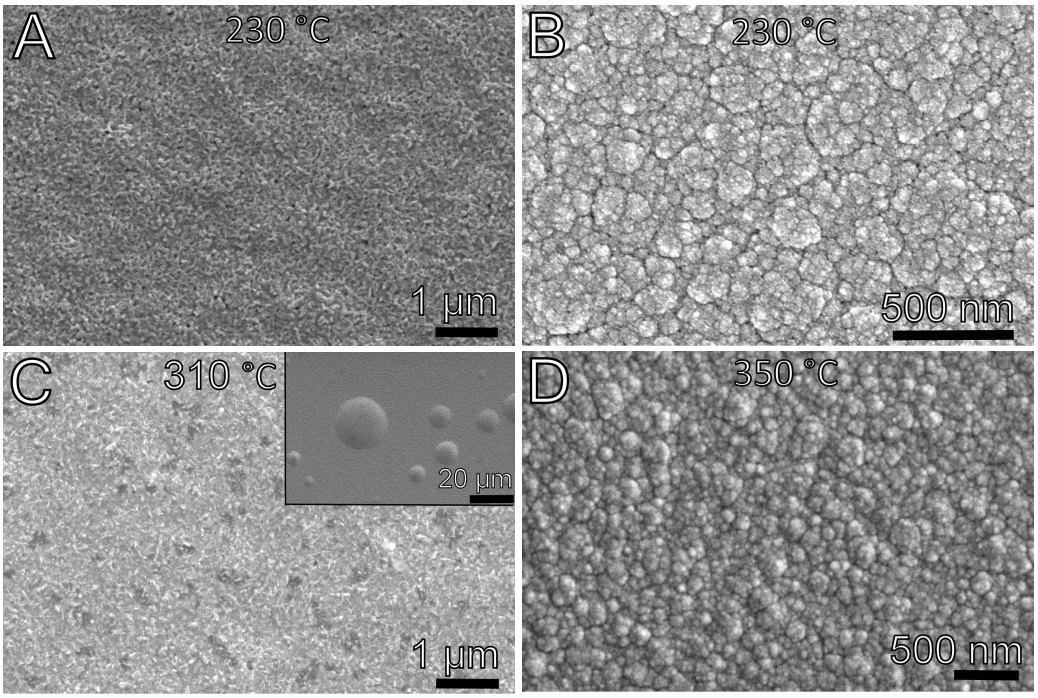

Figure 4.29: SEM micrographs of soft-annealed stacked layers (A, C) and co-deposited (B, D) precursor surface morphology. C inset – SEM micrograph of stacked layer annealed at 350 °C for 30 min.

(230 °C, Fig. 4.29 A, B) grains are not fully coalesced, small voids were visible, whereas at 310 °C for stacked CZT precursor and at 350 °C for co-deposited,

grains were fully merged leaving no gaps in the film. Annealing at higher temperature promotes coalescence of grains and presumably leads to smoother films.

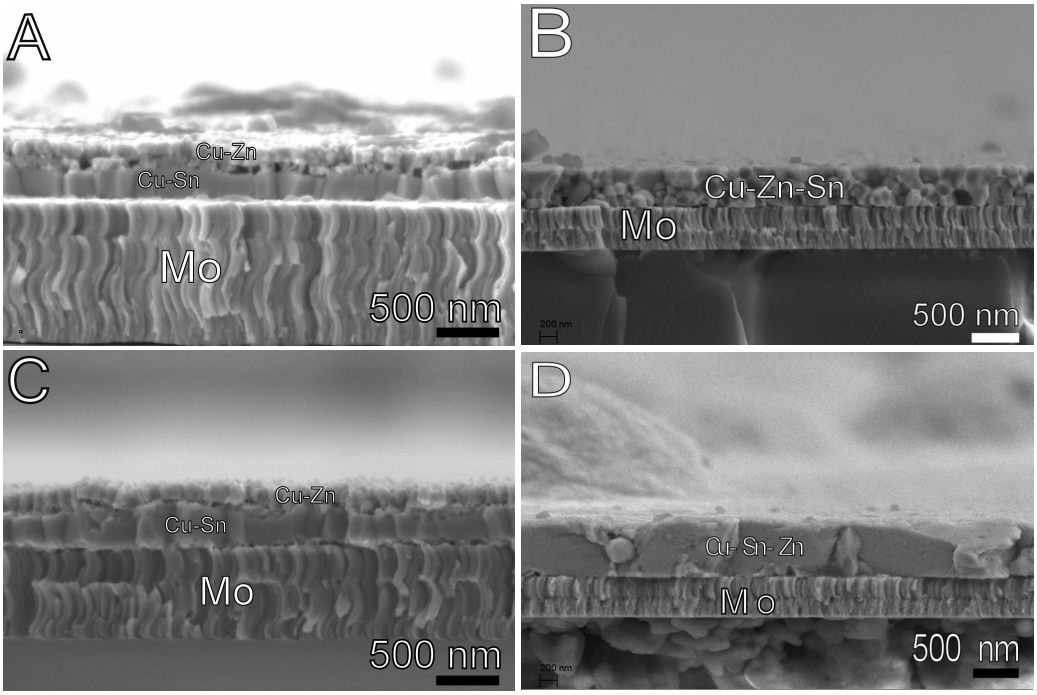

Figure 4.30: SEM micrographs of cleaved cross-sections of Cu/Sn/Cu/Zn (A, C) and Cu-Zn-Sn (B, D) precursors, preliminary annealed at 230 °C (A, B), at 310 °C (C) and at 350 °C (D).

SEM images of cleaved cross-section of CZT precursor are presented in Fig. 4.30. As can be expected, the structure of preheated CZT precursor for sequentially deposited and co-deposited strongly differs. For sequentially deposited precursor, two different layers can be clearly distinguished. Top layer was composed of small grains, presumably Cu-Zn phase, as Zn was deposited on top, whereas bottom layer was made of large grains, which are attributed to Cu-Sn phase. However, voids and gaps were visible between the layers. As the soft-annealing temperature was increased, the Cu-Zn grains grew larger and fewer and smaller voids were observed between Cu-Zn and

Cu-Sn layers. No significant temperature effect was observed on Cu-Sn grains. Large gaps between two layers could be related to the diffusion of copper during annealing. In the as-deposited Cu/Sn/Cu/Zn precursor copper layer is located between Sn and Zn layers and copper diffusion coefficient compared to Zn and Sn is the highest one, especially Cu diffusion into Sn occurs at very high rate [91]. Therefore, during annealing copper diffuses to Zn and Sn layers to form intermetallic compounds, leaving vacancies in the copper layer, which later sum up and voids are formed. At T > 300 °C grains of Cu-Sn and Cu-Zn grow larger and gradually started to merge therefore gaps between Cu-Zn and Cu-Sn layers were reduced.

The effect of soft-annealing for co-deposited precursor is much different. Films annealed for 120 min at 230 °C (Fig. 4.30 B) is comprised of relatively small Cu-Zn and Cu-Sn grains which appeared to be distributed evenly over film thickness. After heating at 350 °C for 10 min, CZT film is composed of large extending whole film thickness grains. Large grains are either Cu-Zn or Cu-Sn, thus locally (in the volume of grain diameter) one of component is not present (either Zn or Sn) and presumably during selenization could lead to inhomogeneous formation of CZTSe. Furthermore, it was noticed that annealing at 350 °C circular shape hillocks occurred in the CZT films (Fig. 4.30 D out of focus). This could be related to the stresses that are caused by fast growth of grains, as was observed for the sequentially deposited CZT precursor.

Note that large grains of Cu-Zn are observed in preheated co-deposited precursor, whereas in sequentially deposited films it is not so clearly seen. Because of the low formation energy of Cu-Zn phase, which is almost two times lower than that of Cu-Sn [120], we would expect large grains of Cu-Zn to form as well. The reason of small Cu-Zn grains in the sequentially deposited precursor could be related to the peculiarities of Zn electrodeposition. Because Zn is deposited at negative potential at which hydrogen evolution

reaction already occurs and pH changes in the vicinity of working electrode, Zn can react with OH^- to form $Zn(OH)_2$ and/or ZnO. In fact, during EDX measurements of Cu/Sn/Cu/Zn we detected up to 20 at.% of O. Naturally, formation of Cu-Zn phase is inhibited by oxygen containing Zn compounds.

In summary, in this section the formation of intermetallic compounds during preliminary annealing was investigated by XRD and XRD *in situ* methods. It was shown that after preliminary annealing CZT precursor contained pure metallic Sn, γ-Cu_5Zn_8 and η-$Cu_{6.26}Sn_5$ phases, which are in strong agreement with a phase diagrams of Cu-Sn and Cu-Zn systems [118, 121]. XRD results confirmed that $T > 300$ °C was necessary to fully alloy pure Sn and to reduce gaps and voids between Cu-Sn and Cu-Zn layers in sequentially deposited precursor.

4.5 Selenization of Cu-Zn-Sn precursor

In this study the investigation of selenization can be categorized into three main parts. In the first part the influence of CZT composition on CZTSe morphology, absorber crystal structure, formation of defects and solar cell performance was examined. In this case, all CZT precursors were co-electroplated on home-made sputtered Mo substrates. In the second part, the influence of selenization conditions on the structure and morphology of CZTSe layers as well as performance of CZTSe solar cells was investigated. In this instance, all CZT precursors were co-deposited on commercial Mo substrate and before selenization preheating was applied to all CZT films. The third part discusses the selenization of sequentially deposited CZT precursor.

4.5.1 Cu-Zn-Sn precursor composition influence on CZTSe and solar cell performance

CZT samples were co-electroplated with three different compositions. All were Cu-poor, that is Cu/(Zn+Sn) ratio was 0.8 – 0.9, whereas ratio of Zn/Sn was varied. Zn/Sn ratio in the Zn-rich samples was in the range of 1.2 – 1.3, in the Sn-rich, ratio varied from 0.75 – 0.85 and in stoichiometric samples Zn/Sn ratio was 1±0.07. Firstly, annealing conditions were chosen according to the "non-aggressive" standard conditions for sequentially sputtered CZT precursor. Selenization was performed at 450 °C, under 1 mbar Ar pressure for 30 min with 50 mg of Se powder inside a graphite box (volume ~23 cm^3). In general, pinholes, burst bubbles and hillocks were observed in all CZTSe solar cell surface morphology, but the density of these features depended on the initial CZT composition. Because of the compositional and thickness uniformity issues of electrodeposited CZT precursor, it is rather difficult to quantitatively asses the quality of CZTSe layers. However based on SEM surface images of CZTSe solar cells we have distinguished two types of morphologic defects (see Fig. 4.31) and have approximately estimated their density. The obtained results are presented in table 4.6. As can be seen in the

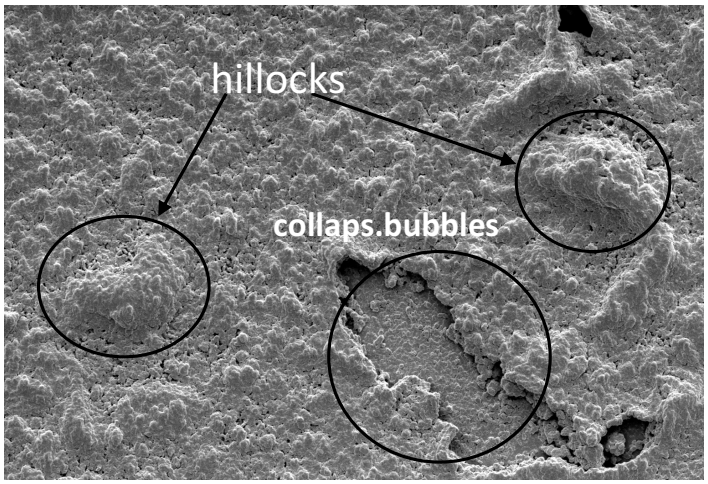

Figure 4.31: SEM micrograph of CZTSe solar cell surface morphology.

Table 4.6: CZT precursor composition, selenization conditions and density of morphologic defects.

CZT precursor composition	Selenization conditions	*Number of collaps. bubbles per mm^2	*Number of hillocks per mm^2
Sn-rich (Zn/Sn=0.75)	450 °C, 1 mbar, 30 min	260	143
Stechiometric (Zn/Sn=1.05)	450 °C, 1 mbar, 30 min	54	340
Zn-rich (Zn/Sn=1.11)	450 °C, 1 mbar, 30 min	81	107
Stechiometric (Zn/Sn=1.05)	550 °C, 1 bar, 30 min	18	36

table the highest number (bubbles + hillocks ~400 per mm^2) of morphologic defects was found in the samples where CZTSe absorber was prepared from Sn-rich and stoichiometric CZT precursors selenized at 450 °C, under 1 mbar Ar pressure and for 30 min. Meanwhile sample prepared from Zn-rich CZT precursor contained less defects (~190 / mm^2) and film was more compact than films prepared from Sn-rich in overall. The influence of precursor composition on kesterite morphology was suggested by Scragg [91]. He proposed CZTSe growth model under Zn-rich and Zn-poor conditions and concluded that in the case of Zn-rich CZT precursor, compact and coalesced CZTSe layer forms, leaving excessive ZnSe at the top of CZTSe layer. In the Zn-poor case, all Zn is consumed to form CZTSe leaving partially unreacted Cu_2Se and Cu-Sn-Se. Latter phases are removed by chemical etching leaving pinholes and gaps in CZTSe layer. Although mentioned hypothesis could explain the dependence of observed morphology features on initial CZT composition, it is not exactly appropriate. The chemical etching which was used in this study intended to remove ZnSe, therefore the etching did not remove Cu-Se or Cu-Sn-Se phases and could not be the reason of observed high porosity of Zn-poor films.

One of the possible explanations could be related to the formation of gaseous phase of tin selenide during selenization. As was shown in section 4.4 metallic Sn is present in as-deposited CZT films. During selenization at temperature point where metal selenides starts to form, Sn is already in liquid form and because of the highest density among other selenides it “sinks” to the bottom (at Mo). When temperature is further increased the formation of tin selenide occurs and because it is a volatile compound at high temperatures (> 400 °C) and low background pressure, gases start to accumulate. Naturally, bubbles start to form and when critical pressure is reached they collapse leaving exposed Mo surface. The more Sn is present in the initial CZT films the more described effect will be pronounced. Therefore the high density of burst/collapsed bubbles and hillocks are observed in the Sn-rich samples and in samples with stoichiometric Zn/Sn ratio.

Note that mentioned samples were annealed under low pressure (1 mbar) conditions. The intensity of tin selenide evaporation of course is dependent on background pressure. The higher ambient pressure the less intensive is evaporation of tin selenide. Therefore, we would expect to see lower density of burst bubbles and hillocks in the samples, selenized at high ambient pressure. In fact, CZT precursor with stoichiometric Zn/Sn ratio was selenized under atmospheric pressure (1 bar) and the density of defect is presented in table 4.6 last row. As can be seen the number of defect was significantly reduced (54 / mm^2). Thus we can conclude that the appearance of burst bubbles and hillocks is related to the formation of volatile tin selenide and is more pronounced in Sn-rich samples and under low pressure annealing. As it was shown above, selenization under low pressure results in low quality CZTSe morphology and could be detrimental to the solar cell performance. Selenization under high ambient pressure reduces the formation of morphologic defects, however they are not completely avoided. As it was suggested the main cause of burst bubbles is the formation of volatile tin

selenide which occurs when Se vapour is in contact with liquid Sn. After preheating at T > 300 °C all metals are fully alloyed. The melting point of Sn-related intermetallic compounds is significantly higher (for instance η-$Cu_{6.25}Sn_5$ melting point is 415 °C compared to pure Sn – 232 °C). In this case there is no liquid Sn segregation at the Mo/CZT interface, therefore little or no burst bubbles should appear in CZTSe morphology when preheating step is applied to CZT before selenization. The morphology of samples annealed at 510 °C for 15 min with 10 mg of Se are depicted in Fig. 4.32. Before selenization both CZT samples were Cu-poor and Zn-rich in composition, but in Fig. 4.32 B CZT precursor was preheated at 350 °C for 10 min, whereas the one in Fig. 4.32 A was not. CZTSe film, which was formed from CZT without preheating contains bubble-shape formations, in particular areas exposed $MoSe_2$ was observed. As can be seen in Fig. 4.32 B CZTSe film was smooth, compact and no collapsed bubbles or hillocks were seen. Therefore, by applying preheating to CZT precursor it is possible to reduce the negative effect caused by formation of tin selenide and as a consequence to increase the quality of CZTSe morphology.

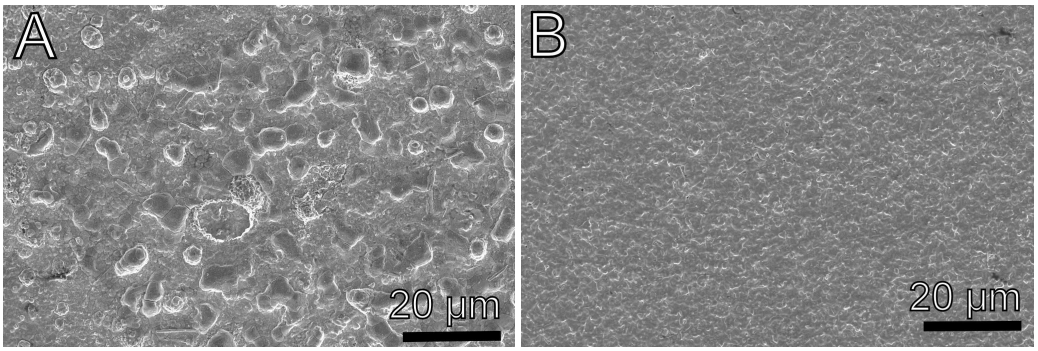

Figure 4.32: SEM micrographs of CZTSe morphology selenized at 510 °C for 15 min from Cu-poor and Zn-rich CZT precursor (A) without preheating (B) preheated at 350 °C for 10 min.

CZTSe solar cells were fabricated and solar cell's parameters were measured under illumination. However, none of the above mentioned samples showed considerable photo activity. SEM images of FIB prepared cross-section (not shown here) revealed that almost all metallic Mo was selenized and could be the reason of solar cell inactivity. This also indicates that optimal even low temperature selenization for sputtered CZT precursor is too "aggressive" for electrochemically deposited films. As it was shown in section 4.2 electrochemically co-deposited CZT films are porous and Se diffusion through film is much higher than in sputtered precursor. According to Shin et al. the rate of formation of $MoSe_2$ is strongly related to the Se diffusion through CZT/CZTSe layer [122], therefore Mo was significantly selenized in the case of electrodeposited CZT.

Selenization conditions were adjusted in order to minimize $MoSe_2$ thickness. The amount of Se was reduced, but annealing temperature was increased to 550 °C. Note that preheating under $Ar+H_2$ atmosphere at 250 °C for 120 min was applied before selenization. By changing selenization conditions the formation of $MoSe_2$ was considerably reduced. SEM micrographs of CZTSe solar cell morphology and FIB prepared cross-section are depicted in Fig. 4.33. As can be seen in Fig. 4.33, the characteristics of morphology followed similar trends as in the samples discussed before. In the Zn-rich sample CZTSe films were compact, relatively smooth and continuous, whereas in the Sn-rich and stoichiometric Zn/Sn ratio, CZTSe layers were porous, the formation of hillocks and gaps were observed. Considering the interface between CZTSe and Mo despite initial CZT composition large voids and local delamination were observed, as can be seen in Fig. 4.33 B, D, F. The formation of voids is not clearly understood though it is often observed in the literature [80-84, 90-95]. Scragg [91] suggested that it is related to the fast Cu diffusion. During selenization Cu diffuses to the surface to form copper selenide leaving vacancies and voids at the Mo/CZT interface. This explanation

is more characteristic for sequentially deposited CZT precursor although in our co-electroplated CZT initial thin layer was enriched with Cu as well. CZTSe film were composed of two layers with different structure, as can be seen from Fig. 4.33 D, F and Fig. 4.36 B. Layer at the Mo/CZTSe interface was

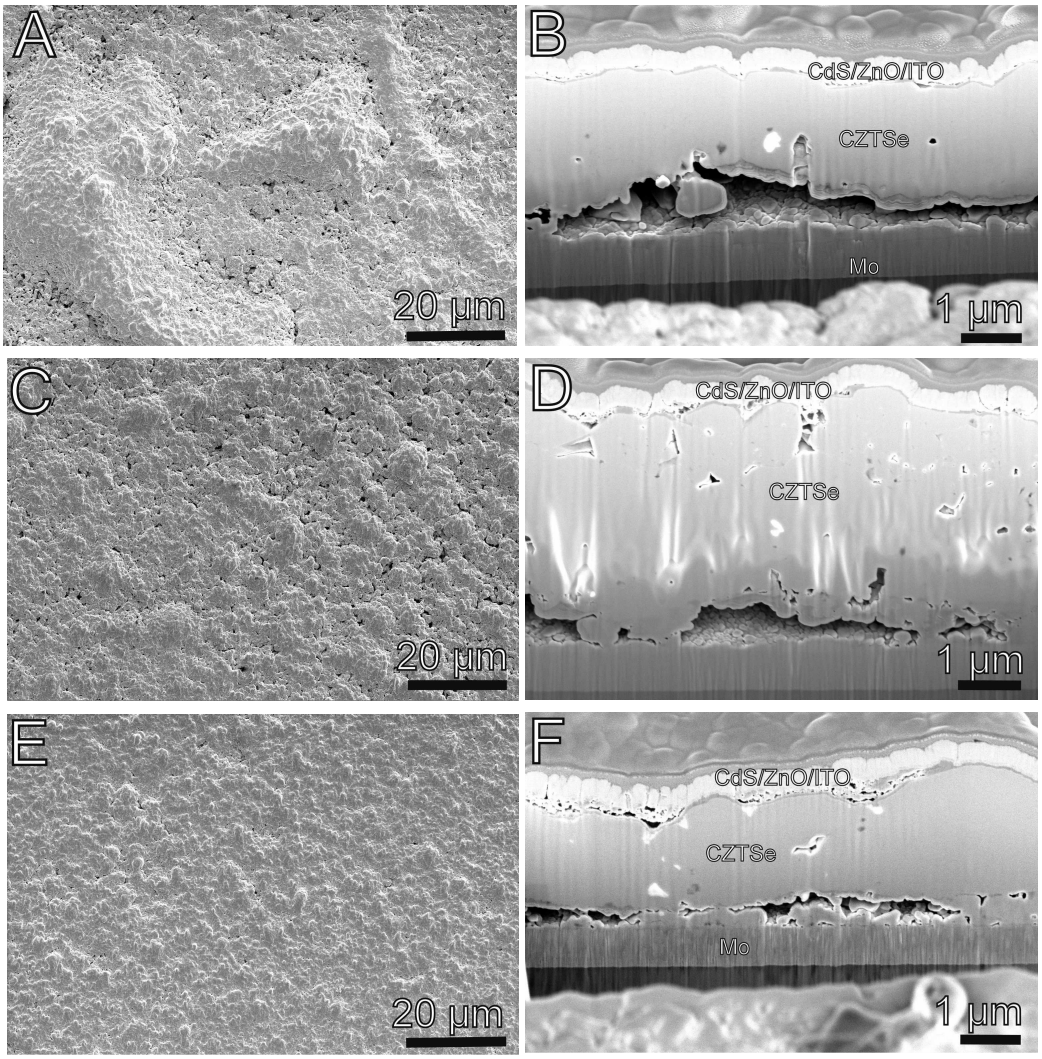

Figure 4.33: SEM micrographs of CZTSe solar cell surface morphology and FIB prepared cross-section in samples with (A, B) stoichiotmetric Zn/Sn ratio, (C, D) Sn-rich, (E, F) Zn-rich.

composed of irregular shape small grains which were unevenly distributed and were attributed to the formation of secondary phases. The second layer

was composed of fine CZTSe grains of various sizes: largest ones extended whole film thickness about 2-3 µm in diameter and as small as few hundreds nm. Particular dual-structure of CZTSe films was also observed in other studies [84]. One of the possible explanations of such phenomenon can be related to the CZTSe decomposition reaction when in contact with Mo [54, 55]. Scragg using strictly thermodynamic approach calculated that Mo/CZTSe interface is not stable at traditionally applied selenization temperatures and therefore decomposition of CZTSe occurs which results in the formation of binary selenides (SnSe, ZnSe Cu_2Se) and $MoSe_2$ [123]. Because the source of binary selenides is the decomposition reaction we would expect it to be of low crystalline quality and composed of small grains, which is what we observe at Mo/CZTSe interface.

It was noticed that aggregates which appear bright (enhanced secondary electron emission) in SEM images were related to ZnSe and this observation was validated by EDX mapping. Therefore, from SEM images of cross-section it is possible to evaluate weather CZTSe layer contains ZnSe and where it is located. As can be seen in Fig. 4.33 (B, D, F) ZnSe was detected in all samples. Naturally, the highest amount of ZnSe was in the Zn-rich sample (Fig. 4.33 F) and only traces were detected in Sn-rich and with stoichiometric Zn/Sn ratio.

Of course, FIB prepared cross-section is only ~10 µm wide as is not suitable technique to estimate the amount of ZnSe on macro scale. Traditionally, unknown phases are indentified by XRD method. However, most intensive XRD peaks of ZnSe and Cu_2SnSe_3 overlaps with those of $Cu_2SnZnSe_4$, thus it is impossible to clearly define the presence of particular secondary phases, at least with conventional XRD optics. Other phases, such as Cu_xSe and SnSe however can be detected. The XRD patterns of CZTSe solar cells formed from stoichiometric Zn/Sn, Sn-rich and Zn-rich precursors are depicted in Fig. 4.34. It contains $Cu_2SnZnSe_4$ (# 04-0101-6295), Mo, $MoSe_2$ (# 04-005-6604) and ITO (# 01-089-4597) phases, latter arises from front contact. Other

layers of front contact i.e. CdS and ZnO has a very low contribution to the diffraction pattern as only ~50 nm of each layer was deposited. Sharp XRD peaks of $Cu_2SnZnSe_4$ phase were observed indicating large crystallites (grains) have formed. Peak at ~31.7° was attributed to $MoSe_2$, though according to ICDD data CZTSe peak could also exist. Usually $MoSe_2$ is of low crystalline quality and its XRD peaks are broad in comparison to CZTSe. Therefore a broad peak at 31.7° was attributed to $MoSe_2$. Interestingly all XRD patterns are alike with no significant difference. Because all CZT precursors were Cu-poor we do not observe Cu-Se phases, as expected. Note that although CZT composition was Sn-rich neither SnSe nor $SnSe_2$ were detected. Because these samples were selenized under low pressure the excess of Sn could have been

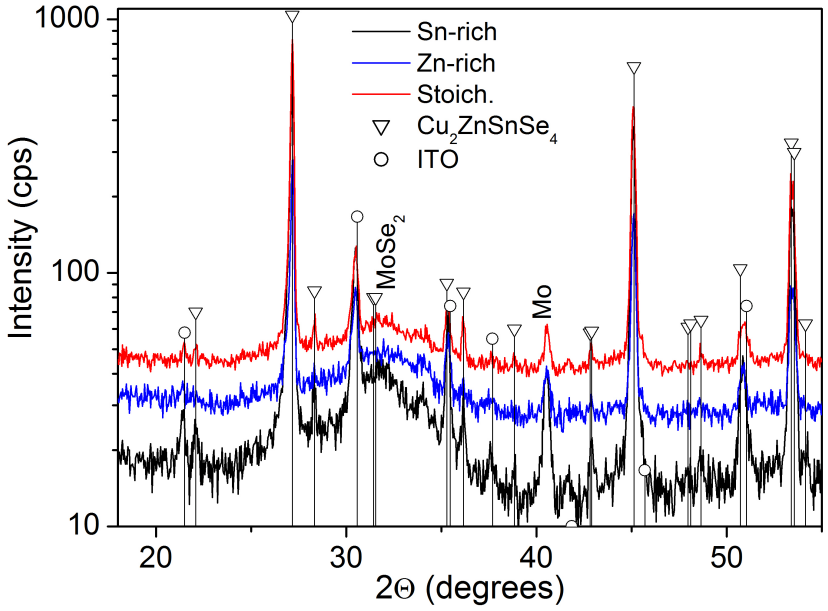

Figure 4.34: XRD pattern of CZTSe solar cells prepared from Zn-rich, Sn-rich and with stoichiometric Zn/Sn ratio precursor.

removed in the form of gaseous SnSe, therefore no tin binary selenides were observed. On the other hand, the most expected ZnSe secondary phase and Cu_2SnSe_3 can not be resolved with conventional XRD setup so are not discussed. The formation ZnSe will be described in the following section.

Solar cell's parameters were evaluated from J-V curves recorded under illumination. The J-V curves of CZTSe solar cells prepared from CZT precursors with different compositions are depicted in Fig. 4.35 A. The calculated electrical characteristics of solar cells are listed in table 4.5. The initial CZT

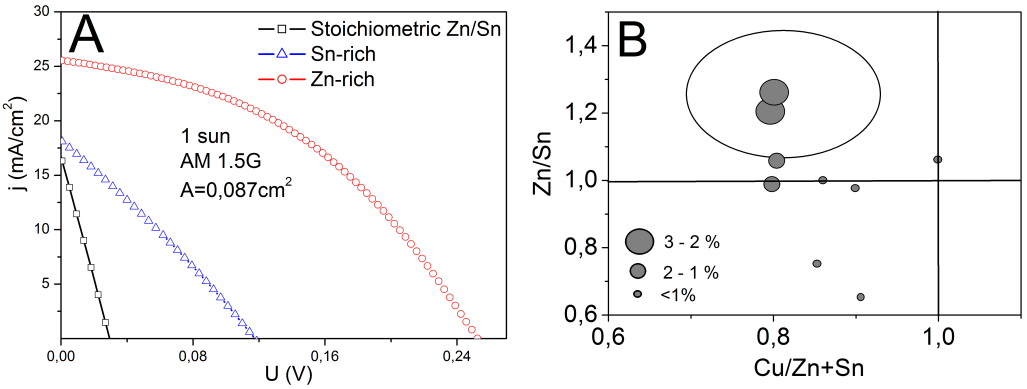

Figure 4.35: (A) J-V curves of CZTSe solar cells prepared from CZT precursor with different composition. (B) Dependence of solar cell efficiency on the CZT composition.

Table 4.7: Parameters of CZTSe solar cells fabricated from precursors with different composition.

Sample	j_{SC}, A/cm^2	V_{OC}, mV	FF, %	η, %	R_s, Ω·cm^2	R_{sh}, Ω·cm^2
Zn-rich	25.23	252	43	2.7	2.9	44.7
Sn-rich	17.63	117	28	0.6	0.72	7.64
Stoich.	16	29	26	0.12	0.26	1.7

composition had a great influence on CZTSe solar cell performance. As we can see in table 4.7 Zn-rich samples showed the best performance and had as high as 2.7% power conversion efficiency. All measured solar cell's parameters were found to diminish from samples with Zn-rich, Sn-rich to stoichiometric Zn/Sn ratio composition. These results coincide with SEM observation (Fig. 4.33), where least morphologic defects were observed for Zn-rich, then for

Sn-rich and most in the samples with stoichiometric Zn/Sn ratio. According to XRD results the crystalline quality of CZTSe absorber was similar for all samples, meaning morphology could be the defining factor for CZTSe solar cell performance. On the other hand, the formation of different type point defects in CZTSe can have a significant influence on solar cell performance as well. As it was discussed in introduction section, the Zn-rich and Cu-poor composition leads to favourable V_{Cu} defect formation. Particular acceptor defects are shallow and are ionized at room temperature resulting in p-type conductivity in CZTSe. In the stoichiometric CZTSe composition the formation of Cu_{Zn} antisite defects is favourable, which is a relatively deep defect and is only partially ionized at room temperature. The high resistance of CZTSe absorber results in high series resistance of CZTSe solar cell consequently significantly reducing fill factor, which is the case for solar cells, prepared from Sn-rich and stoichiometric Zn/Sn ratio (Fig. 4.35 A). The influence of composition on solar cell efficiency can be seen in Fig. 4.35 B. Highest efficiencies were achieved in the Cu-poor and Zn-rich composition region. Very similar diagram was reported in [44] showing that particular composition condition is necessary for high efficient solar cells.

The external quantum efficiency (EQE) curves of CZTSe solar cells fabricated from Zn-rich and Sn-rich precursors are depicted in Fig. 4.36 A. Because of very low electrical parameters of CZTSe solar cell prepared from precursor with stoichiometric Zn/Sn ratio latter was not included. Generally, EQE is the ratio of incident photon number to the carrier number extracted to contacts. It shows how much of photogenerated carriers reach contacts. What is more, EQE is measured as a function of wavelength, therefore we can roughly estimate in what part of solar cell current is lost.

Ideally EQE curve should be rectangular shape, however because of the absorption loss in window and buffer layers some part of current is already lost at the front contact, as indicated in Fig 4.36 A by dotted rectangular. For

Zn-rich case the EQE rose up to 70% reached plateau up to 800 nm, then gradually decreased up to 1500 nm. Short wavelengths are absorbed at the front of CZTSe solar cell, whereas long penetrates into the bulk and up to the Mo/CZTSe interface. As can be seen in Fig. 4.36 A the major portion of current is lost at the bottom part of CZTSe solar cell as significant drop in EQE is observed from 800 nm. It could be related to the poor quality of Mo/CZTSe interface and the formation of secondary phases as been observed in cross-sections (Fig. 4.33, Fig. 4.36 B). Depending on the secondary phase nature it can contribute to higher resistance or create shunt paths at Mo/CZTSe interface. For the Sn-rich sample EQE reaches maximum of only ~13% and then follow similar trend as in Zn-rich case, indicating that similar current loss mechanisms existed at the bottom of the CZTSe solar cell. Very low value of EQE could be related to the formation of different defect type than in Zn-rich case, as was discussed above. The bang gap (E_g) of CZTSe absorber was calculated from EQE curve and was found to be 0.94±0.02 eV (Fig. 4.36 inset). This value is in a strong agreement with E_g reported in the literature [58, 82, 87, 88].

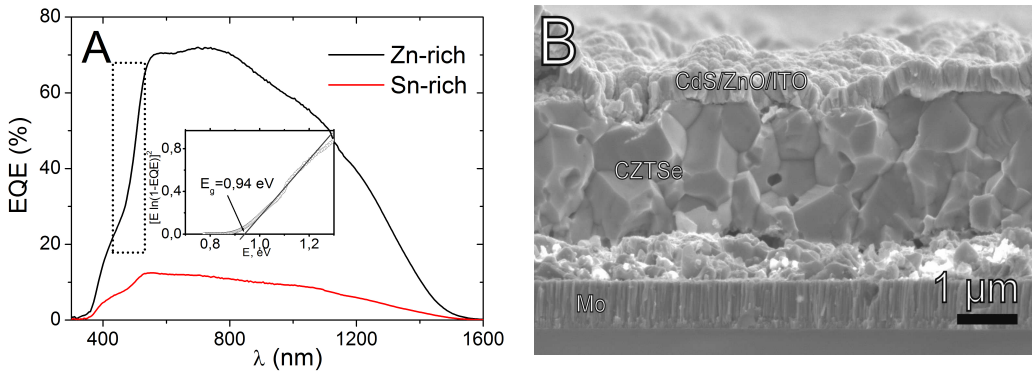

Figure 4.36: The external quantum efficiency curves of CZTSe solar cells fabricated from Zn-rich (black line) and Sn-rich (red line) CZT precursors (A). Inset – graphical estimation of CZTSe E_g via linear extrapolation of the EQE data. SEM micrograph of champion solar cell cross-section (B).

In conclusion the influence of initial CZT composition has a significant effect on CZTSe absorber and on final CZTSe solar cell performance. As has been demonstrated in many aspects, the best results in regard to morphology and solar cell performance was achieved with Zn-rich and Cu-poor CZT composition.

4.5.2 Photoluminescence

In order to understand recombination process and the formation of defects in CZTSe and latter dependence on composition, photoluminescence (PL) spectroscopy was applied. Firstly, the recombination type was investigated in CZTSe films, by measuring main CZTSe PL peak (located at 0.9 eV) intensity as a function of excitation power at room temperature. As can be seen in Fig. 4.37 the PL peak located at 0.9 eV gradually decreased as excitation power was decreased and no peak shift was observed. PL intensity is proportional to excitation power as $I \sim P_{ex}^{k}$, where I is the intensity of PL peak, P_{ex} - excitation power, k is exponent constant.

According to Schmitdh and Lischka theory when excitation photon energy is greater than semiconductor E_g, k for excitonic recombination is in the range of 1 to 2, whereas for free carrier to bound level or donor-acceptor pair recombination, $k \leq 1$ [124]. We have found out that the relationship between $\log P_{ex}$ and $\log I$ in our case was linear and the calculated value of k was equal to 1.03±0.03 (Fig. 4.37 inset). The excitonic recombination can be disregarded not only because k value does not fit in the appropriate interval but exitonic recombination is usually observed in pure and high-quality single crystal samples.

Other recombination types could be equally possible. However, CZTSe is naturally a p-type semiconductor and the formation of only acceptor defects, was reported [35, 36]. According to theoretical calculations, the formation

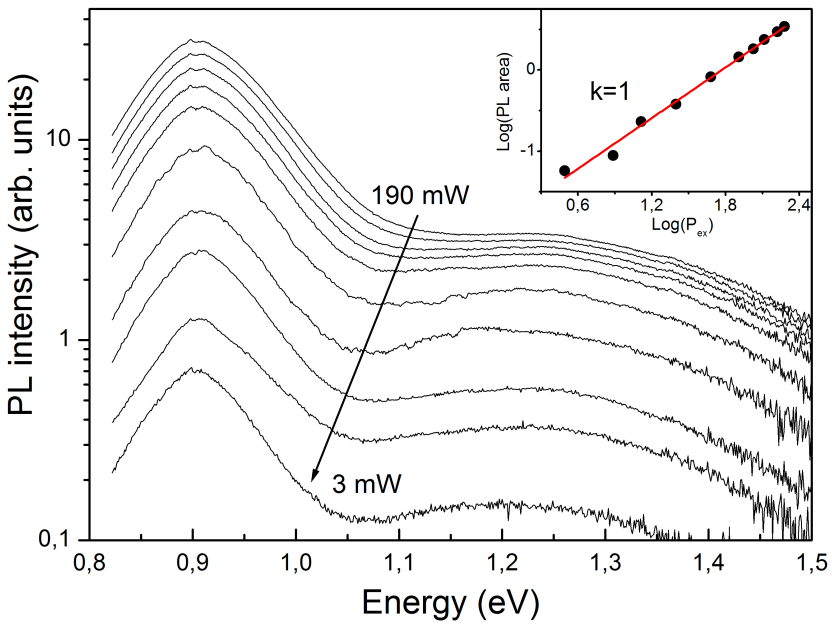

Figure 4.37 CZTSe PL spectra as a function of excitation power (decreasing power indicated with an arrow). Inset - the graphical estimation of coefficient *k*. Excitation wavelength is 533 nm.

energy of donor defects (Zn_{Cu}) in CZTSe is relatively high. What is more, it was predicted that high population of V_{Cu}+Zn_{Cu} defect clusters forms in CZTSe neutralizing if present Zn_{Cu} defects [45], so donor-acceptor pair recombination type is unlikely to occur in CZTSe. Furthermore, if donor-acceptor pair recombination would be dominating, PL peak should blue-shift as excitation power is increased [125]. Taking into account the above mentioned facts we can conclude that free carrier to acceptor is the most probable recombination type in CZTSe. Grossberg et al. have also attributed CZTSe PL peak emission to band to impurity recombination [126]. On the other hand, it was suggested that in heavily doped and strongly compensated semiconductors recombination involving band-tail states are also possible [127]. If latter recombination dominates, the PL peak of CZTSe should red-shift and blue-shift when temperature and excitation power is increased, respectively. Therefore sometime it is very difficult to distinguish donor-acceptor, free

carrier to acceptor or free carrier to band tail states recombination types. Temperature dependent PL measurements and determination of doping level in CZTSe should be performed in order to fully understand recombination mechanisms.

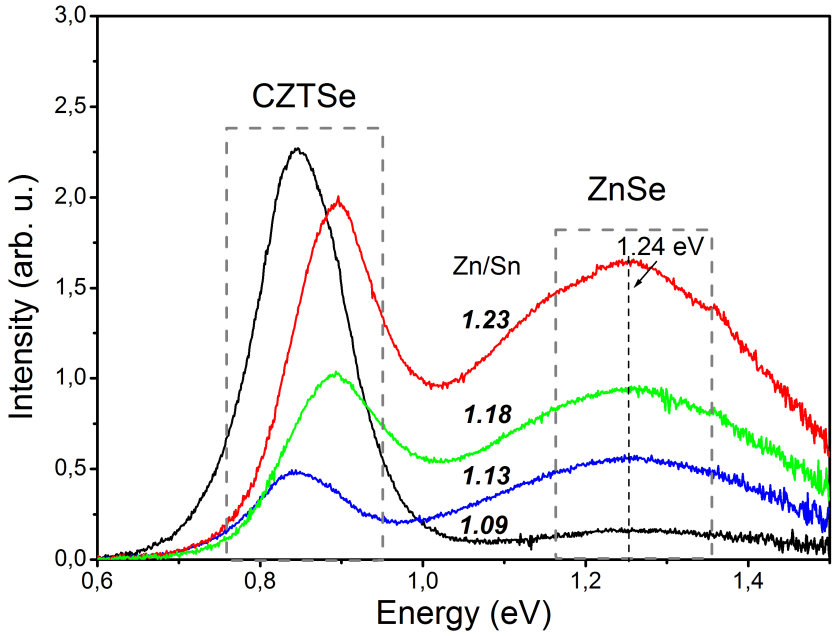

Figure 4.38: Photoluminescence spectra of CZTSe. Zn/Sn ratio measured with EDX is indicated in the graph. Excitation wavelength 533 nm.

Measured PL spectra of CZTSe samples often contained two separate PL peaks, see Fig. 4.38. PL peak at 0.85 – 0.9 eV was attributed to the recombination of free carriers to acceptor in CZTSe, whereas PL peak at 1.24 eV was associated with carrier recombination in ZnSe. It should be mentioned that the second PL peak was also observed by other authors [53, 128, 129]. They suggested that ZnSe contained defects in the band gap caused by inclusion of Cu or Sn. Hence, a PL peak at 1.24 eV is related to the radiative band to impurity or donor-acceptor pair recombination in ZnSe. Because ZnSe E_g is ~2.7 eV and PL emission is at 1.24 eV, the recombination in ZnSe occurs via deep defects. The deeper defect via which recombination occurs, the

broader is PL peak [130]. CZTSe defects are relatively shallow (up to 0.11 eV above valance band) therefore we observed relatively narrow CZTSe and broad ZnSe PL peaks. ZnSe PL peak intensity is proportional to the Zn/Sn ratio, as can be seen in Fig. 4.38. As the Zn/Sn ratio increases the intensity of ZnSe PL peak increases as well, therefore photoluminescence can be implemented to detect ZnSe secondary phase in CZTSe [128].

PL spectra of CZTSe samples selenized at 510 °C for 15 min with 10 mg of Se are depicted in Fig. 4.39. The intensity of main CZTSe PL peak is also related to the Zn/Sn ratio. As we have assumed that recombination in CZTSe is free carrier to acceptor thus the intensity of PL peak will be acceptor concentration dependent. Brammertz et al. have showed that acceptor defect

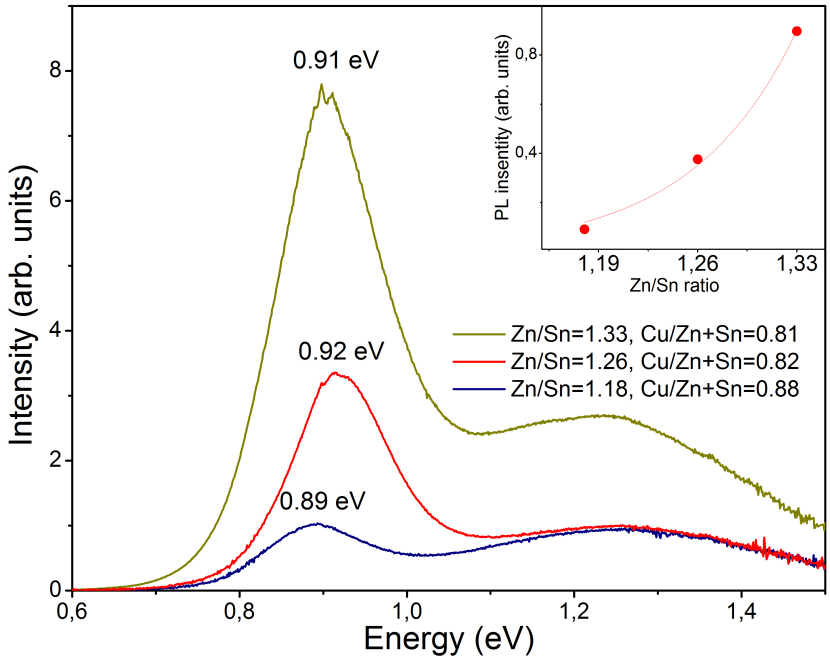

Figure 4.39 Photoluminescence spectra of CZTSe selenized at 510 °C for 15 min with 10 mg of Se. Inset – integrated PL peak area as a function of Zn/Sn ratio.

concentration exponentially depends on Zn/Sn ratio [131]. The PL intensity dependence on Zn/Sn ratio is depicted in the Fig. 4.39 inset. It can be seen that the PL intensity exponentially depends on Zn/Sn ratio.

The influence of Cu content on PL spectra of CZTSe is not clearly understood. On the other hand, it was noticed that when Cu/(Zn+Sn) ratio is greater than 0.88 and Zn/Sn ratio is less than 1.15 CZTSe PL peak was below 0.9 eV. In contrast for samples with more Cu-poor and Zn-rich compositions PL peak shifted closer to theoretical value of CZTSe E_g (1.0 eV). This tendency could be related to the formation of different type defect in CZTSe. Theoretically, under stoichiometric and Cu-rich compositions, Cu_{Zn} antisite defect has the lowest formation energy and therefore is the most dominant [35, 36, 45]. Under Zn-rich and Cu-poor composition, the formation energy of Cu_{Zn} defects increases, whereas for V_{Cu} decreases, therefore both defects can coexist. Under even more Cu-poor and Zn-rich conditions V_{Cu} becomes most dominant defect type in CZTSe. As it was mentioned in the introduction, Cu_{Zn} is relative deep defect with transition energy of 0.11 eV, whereas V_{Cu} is a shallow acceptor with transition energy of ~0.02 eV [45]. Because presumably recombination is a free carrier to acceptor, the centre of PL peak will be depended on dominant defects in CZTSe. Hence, the position of main CZTSe PL peak is depended on CZTSe composition: the more Cu-poor and Zn-rich composition, the closer centre of PL peak is to theoretical E_g value of CZTSe.

Here, we have taken into account only the PL dependence on CZTSe composition, however other facts like disorder [132] and selenization conditions [58] can also influence electronic structure of CZTSe and in turn the recombination processes.

4.5.3 The influence of selenization conditions on CZTSe and solar cell performance

The home made Mo, which was used as a substrate for CZT electrodeposition was not very stable in time and moderately sensitive to the chemical treatments. What is more, it required additional adjustments of electrolyte composition in order to obtain targeted CZT composition on Mo substrate of different series though sputtered at the same conditions. Therefore a commercial Mo purchased from Zentrum fur Sonnenenergie und Wasserstoff-Forschung (ZSW) was tested in this study as well. The reproducibility of electrodeposition of CZT increased and precise control of composition was achieved. Because structure and physical properties of commercial Mo is not the same as for the one used before, optimal selenization conditions were no longer valid. Furthermore, the thickness of the CZT precursor was decreased from 600-700 nm to 400-450 nm to obtain 1.0 – 1.5 µm thick CZTSe absorber. Because of the short carrier life time and in turn shorter carrier diffusion length in CZTSe [7, 93], the thinner absorber should result in the improved collection of generated carriers (higher j_{SC}).

Selenization conditions were varied as to obtain CZTSe layer with least thickness of $MoSe_2$. As it was mentioned in the introduction, the formed $MoSe_2$ thickness depends on the annealing temperature, duration and partial pressure of Se (which is related to the amount of elemental Se present in the annealing container). Selenization conditions are listed in the table 4.8. When composition is measured by XRF, information is extracted from whole sample volume down to the glass. In the stoichiometric $Cu_2ZnSnSe_4$ film Se would constitute 50 at%. When measured value of Se is greater than 50 at%, the content of $MoSe_2$ can be estimated. As results indicate selenization process of commercial Mo remarkably depends on the annealing conditions. By decreasing the quantity of Se in the annealing box, the annealing temperature

Table 4.8: Selenization conditions, Se quantity in at.% and $MoSe_2$ thickness.

Sample	Temperature, °C	Time, min	Se, mg	Se, at.%[1]	d_{MoSe2}, nm[2]
V5	550	30	20	76±1.7	2400
V7	550	30	10	68±3.5	2000
V8	530	15	10	63±5.2	1480
V12	510	15	10	53±1.9	50-60[3]

1-taken average value of 6 points for each sample, ± standard deviation

2-measured from FIB made cross-section

3-in the uniform region

and time, the amount of Se in the samples decreased from 76 at% to 53 at%. The calculated $MoSe_2$ thickness from cross-sections strongly correlates with excessive quantity of Se measured by XRF. By changing selenization parameters the formation $MoSe_2$ was reduced to the minimum.

The morphology and cleaved cross-section of samples considered in table 4.8 are depicted in Fig. 4.40 and Fig. 4.41. In Fig. 4.40 CZT precursor was annealed at the same temperature and duration except amount of Se was different (different partial Se pressure). As can be seen from surface morphology (Fig. 4.40 A, C) in both cases continuous and compact CZTSe layer formed. Little bright dots in the Fig. 4.40 C are attributed to the residues of ITO after etching in 10% HCl solution. Layers comprised various size fine CZTSe grains extending through whole film thickness. Note, that when 20 mg of Se was used all metallic Mo was selenized i.e. converted to $MoSe_2$, meanwhile in the case of 10 mg Se Mo was considerably selenized though little part of metallic Mo still remained. In Fig. 4.41 the morphology and cross-section of samples annealed at lower than 550 °C are presented. As can be seen in Fig. 4.41 films were composed of various size grains, raging from 500 to 5000 nm. Interestingly, after reducing annealing time and temperature still large (0.5 – 5 μm) CZTSe grains formed indicating that from co-electroplate precursor the

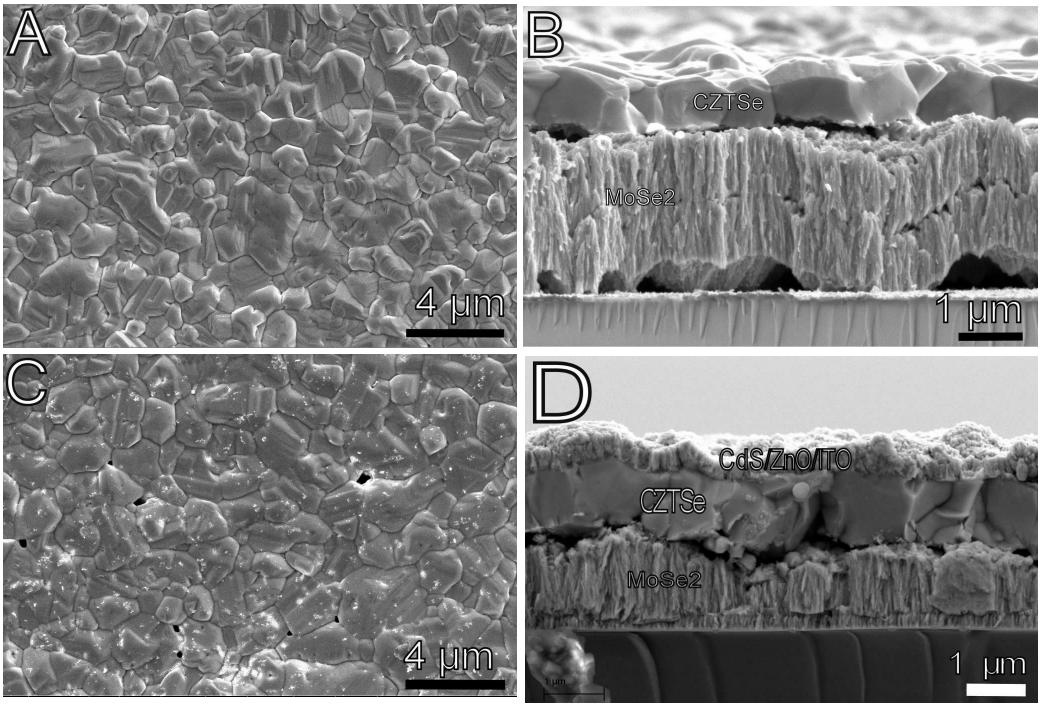

Figure 4.40: SEM micrographs of CZTSe absorber surface morphology and cross-section annealed at 550 °C for 30 min with (A, B) 20 mg of Se and (C, D) 10 mg of Se.

growth of CZTSe grains was relatively rapid. Commonly 550 °C and 30 min are used to form CZTSe layer comprising of 2-3 µm size grains [133]. From cross-section images (Fig. 4.41 C, D) we did not observe $MoSe_2$ though when measuring Se concentration with XRF it was 63 at.% for the sample depicted in Fig 4.41 B. The reason is the uneven CZT precursor thickness. The thicker part of CZT is less selenized, therefore if CZT precursor thickness is not homogenous it leads to the inhomogeneous formation of $MoSe_2$. In fact, as can be seen in table 4.8 the standard deviation of Se quantity of particular sample is the highest one validating the assumption of uneven thickness of CZT layer.

Despite annealing conditions, $MoSe_2$ thickness or initial CZT composition formation of large voids and gaps were observed at the Mo/CZTSe interface.

Note that in the samples V7 and V8 the formation of aggregates composed of small grains at Mo/CZTSe was observed (Fig. 4.40 D and Fig.4.41 B) similar to

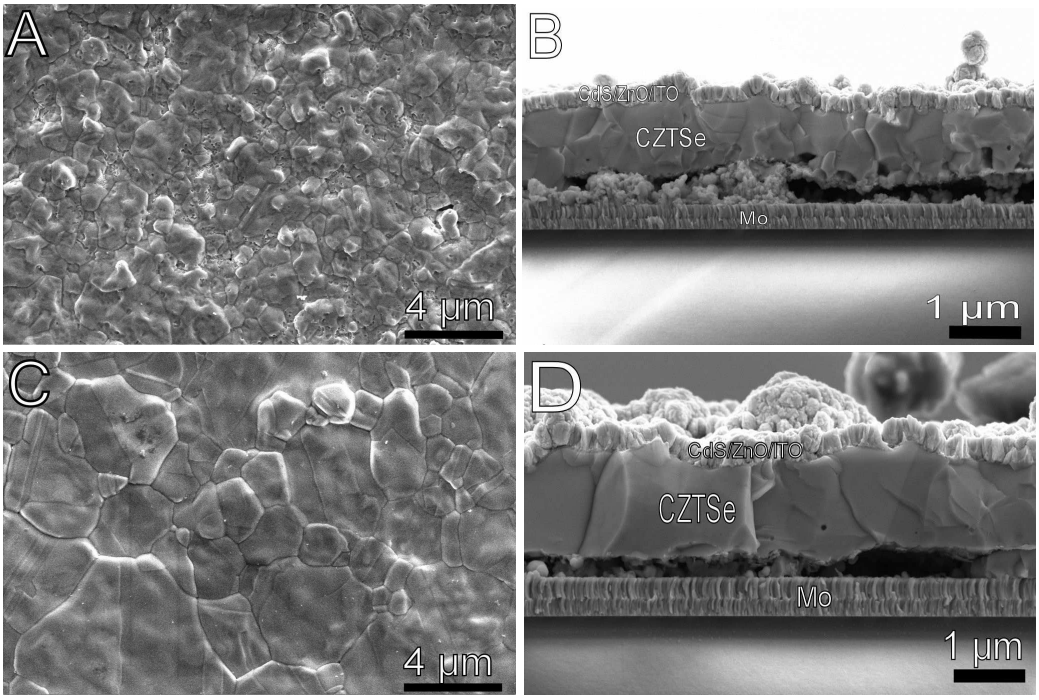

Figure 4.41: SEM micrographs of surface morphology and cross-section of samples annealed at (A, B) 530 °C and (C, D) 510 °C for 15 min with 10 mg of Se.

the ones, discussed in subsection 4.5.1 and were attributed to the secondary phases. What is more, the grains of CZTSe at Mo/CZTSe interface for particular samples were less refine, contained more voids and were smaller in general than those of samples V5 and V12. These discrepancies can be related to the selenization conditions. In table 4.9 partial and equilibrium Se pressure are presented for each selenization case. Partial pressure of Se was calculated according to the ideal gas equation and is dependent on the amount of elemental Se present in the container and annealing temperature, whereas equilibrium Se pressure means maximum pressure of Se possible at particular temperature. In order to avoid decomposition of CZTSe selenization should be

performed under saturated Se atmosphere as was suggested by several authors [52, 91, 129]. As can be seen in table 4.9 the saturated Se atmosphere is reached under 1 and 4 annealing conditions as the difference

Table 4.9: Equilibrium and partial pressure of Se of each selenization case.

No	Sample	Annealing conditions	p_{eq}[1], Pa	p_{Se}, Pa	$\Delta(p_{Se}-p_{eq})$
1	V5	550 °C, 20 mg Se	13740	15524	+1784
2	V7	550 °C, 10 mg Se	13740	7762	-5978
3	V8	530 °C, 10 mg Se	9660	7597	-2063
4	V12	510 °C, 10 mg Se	6760	7378	+618

1-Equilibrium Se pressure taken from [134].

between equilibrium and calculated partial Se pressures is positive. Of course, we have to take into account that Se vapour could exit annealing container because it is not perfectly sealed, however static ambient pressure of 1 bar should have prevented from rapid Se extraction. Under deficient Se atmosphere we would expect CZTSe grains to be smaller less refine structure and contain more crystallographic defects. Latter is difficult to measure, but high quality SEM images of CZTSe cross-section enable to roughly evaluate the quality of grains. As it was mentioned, better quality grains were obtained in samples V5 and V12, which were annealed under saturated Se atmosphere.

Because ZnSe and Cu_2SnSe_3 secondary phases can not be identified by XRD method with conventional optics, Raman spectroscopy was used. By choosing appropriate excitation wavelength, resonance conditions can be achieved for particular secondary phase and even small amounts can be detected. Raman spectra of V5 and V12 samples are depicted in Fig. 4.42. It can be seen that using red laser as an excitation source no other than CZTSe phase was identified indicating that single phase CZTSe has formed. On the other hand, ZnSe cannot be detected using red laser, therefore Raman

spectra was also recorded with excitation wavelengths in UV region and is presented in Fig. 4.42 B. As can be clearly seen ZnSe is detected in the V12

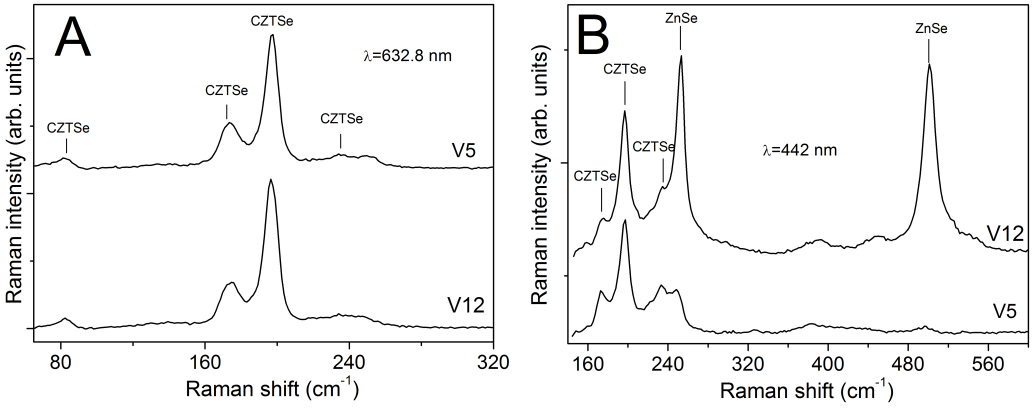

Figure 4.42: Raman spectra of V5 and V12 CZTSe samples with excitation wavelengths of 632.8 nm (A) and 422 nm (B).

sample, whereas in the sample V5, band at ~250 cm^{-1} could also be detected, though it was not attributed to ZnSe phase, because no overtone at ~ 500 cm^{-1} was observed. The Zn/Sn ratio in V5 and V12 samples were 1.1 and 1.15, respectively, therefore composition is not likely to be the reason of large amount of ZnSe in V12. In most of the studies of reaction path of CZTSe it was shown that last phase of solid state reaction to form CZTSe is Cu_2SnSe_3 alloying with ZnSe. However, the beginning of particular reaction was noticed to start at different temperatures [50, 51]. Our measurements showed that the amount of ZnSe decreases exponentially from 400 °C to 500 °C, completely vanishing at 560 °C indicating all ZnSe was consumed to form CZTSe. Therefore, relatively short annealing duration (15 min) at 510 °C could have resulted in not fully reacted ZnSe.

Solar cells were prepared from all CZT precursors discussed above, however neither of samples selenized at lower than 550 °C showed considerable efficiency. The reasons could be related to the incomplete formation of $Cu_2ZnSnSe_4$, as was assumed from Raman spectra or because of

too thin $MoSe_2$ layer. Because of low quality morphology of CZTSe layers we suspect that shunt paths exists in CZTSe solar cells and if semiconducting $MoSe_2$ layer is very thin, solar cells are short-circuited.

By inspecting visually (from colour uniformity of CZTSe layer) and analyzing composition, it was noticed that CZTSe films, selenized under low pressure were more uniform. On the other hand, annealing at low pressure and high temperature would result in serious loss of volatile compounds, therefore a combination of two selenization regimes was implemented. Firstly, selenization was performed under 1 mbar pressure at 400 °C for 30 min and then chamber was filled up to 1 bar Ar pressure, temperature raised to 550 °C and dwelled for 15 min. Schematic representation of sub cell efficiencies of CZTSe solar cells selenized at one-step and two-steps are depicted in Fig. 4.43. As can be seen in Fig. 4.43, there are approximately two

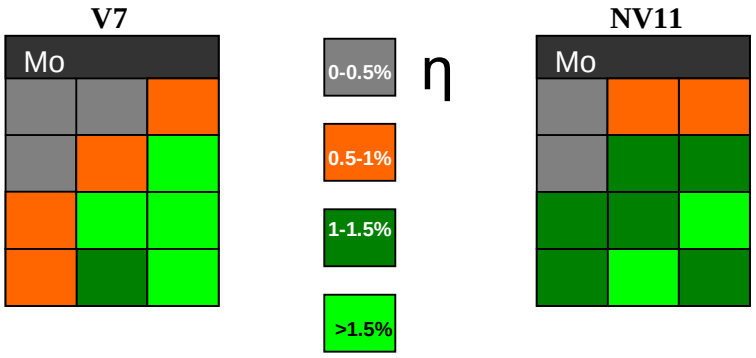

Figure 4.43: The efficiency of CZTSe solar sub cells, where CZT precursor was selenized (V7) one-step, 550 °C, 30 min, 1 bar Ar and (NV11) two-steps 400 °C, 30 min, 1 mbar and 550 °C, 15 min, 1 bar. Square dimensions 3x3 mm^2.

times more solar sub cells with low efficiencies (0-1% grey and orange squares) in the sample annealed at one-step approach than at two-step. This indicated that morphology, composition and consequently physical properties after selenization is more uniform in sample annealed at two-step

selenization approach. On the other hand, the absolute value of sub cell efficiency was higher in the sample annealed at one-step. The average j_{SC} (taken from green and bright green cells) for V7 sample was 26.7 mA/cm^2, whereas for NV11 sample it was 21.3 mA/cm^2. Note that other solar cell parameters such as V_{OC}, R_{sh}, R_s and FF were very similar therefore higher j_{SC} was the main reason of higher overall cell efficiency. It could be related to the larger grain size, because the dwell time at 550 °C at which CZTSe grain growth is promoted is two times longer for one-step selenization approach.

All solar cells fabricated in this work suffered from very low shunt resistance. As a result the FF and V_{OC} were very low as well. According to the theoretical simulation of Si-based solar cells, when series resistance is kept constant (2.3 Ω·cm^2 typical value for CZTSe solar cells studied in this work) and shunt resistance is increased from 10 Ω·cm^2 to 20 Ω·cm^2 the V_{OC} increases by 47%, and j_{SC} by ~13%, whereas if R_{sh} is increased from 20 Ω·cm^2 to 40 Ω·cm^2 the increase of V_{OC} and j_{SC} is 10% and 6%, respectively. Latter indicates that solar cell parameters are greatly influenced in the low R_{sh} region. The R_{sh} of solar cells studied in this work were typically in the range from 10 to 30 Ω·cm^2 therefore we suspect that low R_{sh} is the main cause of low overall solar cell efficiencies (2-3%). Now the source of low R_{sh} could be either formation of highly conductive secondary phases (for example Cu_xSe, $SnSe_2$ [135]) or solar cells are short-circuited because of poor morphology. Even though i-ZnO was deposited to prevent solar cell from short-circuiting, shunt paths still can exist. We did not detect other than ZnSe secondary phase, which is highly resistive and can not create shunt paths, therefore poor morphology and presumably low quality interface between Mo and CZTSe are the main reasons of low R_{sh}. In Fig. 4.44 the cross-section of several CZTSe solar cells are depicted and possible shunt paths are indicated. The occurrence of trenches and not coalesced grains could be related to the

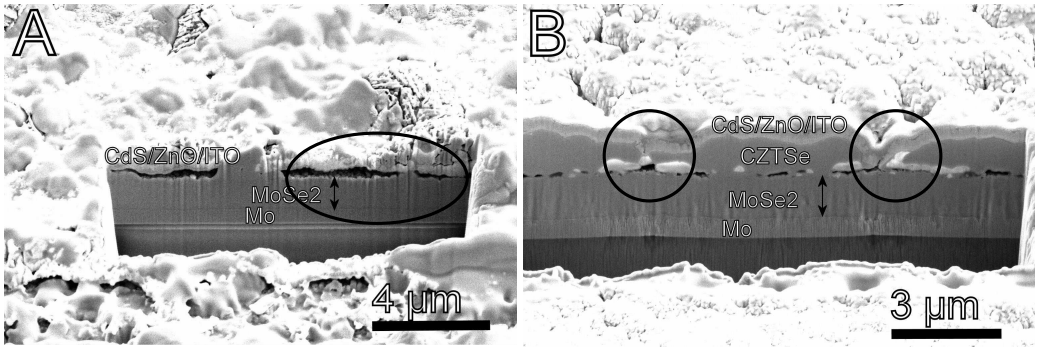

Figure: 4.44: SEM micrographs of FIB prepared CZTSe solar cells cross-section.

peculiarities of CZT electrodeposition. From section 4.2 we know that CZT is deposited at sufficiently negative potential, where hydrogen evolution reaction occurs. Supposing the Mo surface is perfectly uniform the intensity of hydrogen evolution reaction is the same at any point of electrode. However, Mo surface is slightly oxidized thus chemical etching in NH_4-OH is done before electrodeposition. After the etching particular areas of Mo could still contain MoO_x and because hydrogen overpotential on MoO_x is lower than on Mo, the intensity of hydrogen evolution is higher at particular areas. The deposition of CZT at areas where intensive hydrogen evolution occurs is less efficient because of local increase in pH, therefore CZT layer is thinner and composition strongly deviated from expected one. As a result, particular areas actually could be the source of shunt paths.

4.5.4 Selenization of stacked Cu/Zn/Sn/Cu precursor

In this study, the greater attention was given to the selenization of co-electroplated CZT precursor. Only the concept of using flow cell to electrodeposit CZT stacked layers was presented and therefore, the selenization of stacked layer precursor was not deeply investigated.

Two-step selenization conditions, described in 4.5.3, were chosen for selenizing stacked Cu/Sn/Cu/Zn precursor, as reasonable results were achieved for co-electroplated precursors. The morphology and FIB prepared cross-section of CZTSe layer formed from sequentially deposited precursor is depicted in Fig. 4.45. As can be seen from morphology (Fig. 4.45 A), CZTSe layer was relatively compact, composed of various size CZTSe grains. On the other hand, pores were observed (as indicated by circles in the Fig. 4.45 A)

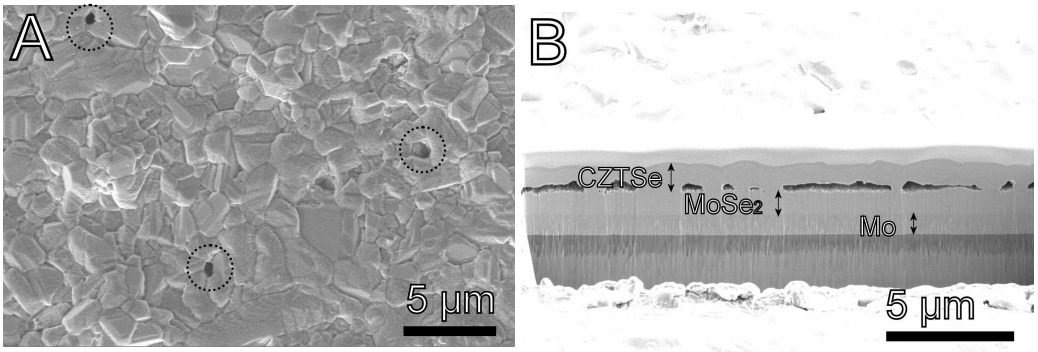

Figure 4.45: SEM micrographs of (A) CZTSe layer morphology and (B) FIB prepared cross-section, formed from Cu/Sn/Cu/Zn precursor by two-step selenization: 400 °C, 30 min, 1 mbar and 550 °C, 15 min, 1 bar.

which was not characteristic for CZTSe films formed from co-electroplated precursor under the same selenization conditions and most probably was related with the incomplete coalescence of grains. Large gaps and holes can be seen in the cross-section as was observed in CZTSe films prepared from co-deposited precursors and as a consequence the thickness of CZTSe layer was uneven.

CZTSe solar cells have been fabricated and solar cell's parameters were measured under illumination. The J-V curve of best performing CZTSe cell is depicted in Fig. 4.46 A and EQE in Fig. 4.46 B. Low solar cell efficiency can be related to the low R_{sh} (11 Ω·cm^2) as it was also observed for co-electroplated

samples. As consequence, the FF was only 32% and led to poor solar cell characteristics. The shape of measured EQE was similar to the one observed

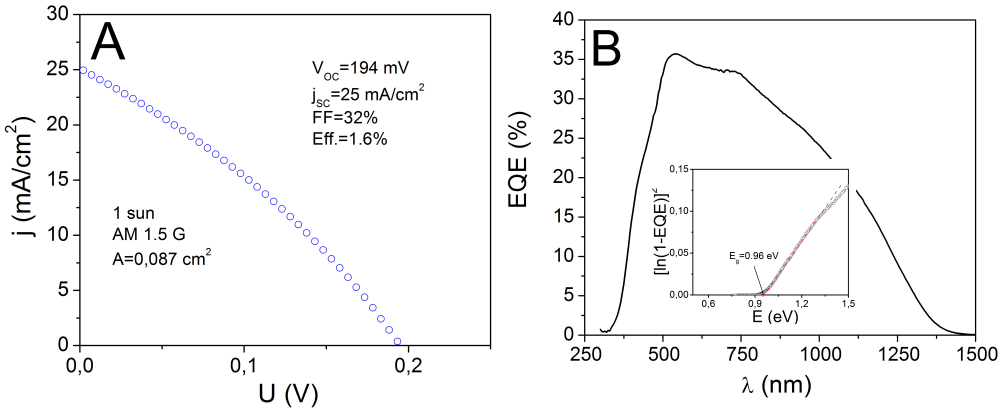

Figure 4.46: (A) J-V curve and (B) EQE of champion CZTSe solar cell fabricated from Cu/Sn/Cu/Zn precursor under two-step selenization conditions.

in CZTSe solar cells fabricated from co-deposited precursor (Fig. 4.36). It rose and reached plateau in the short wavelength region and staredt to gradually decrease from 750 nm. Latter indicates that similar photo current loss mechanism exits in the CZTSe solar cells prepared from stacked layer precursor.

In general, many CZTSe layers formed from stacked layer precursor suffered from poor morphology. In many cases CZTSe film completely peeled off and a lot of collapsed bubbles were observed (not show here). It shows that selenization conditions, which were suitable for co-deposited CZT precursor do not applied for stacked layer precursor. In this case more research is necessary for finding optimal selenization conditions of stacked layer precursor, however it still proves that photovoltaic grade CZTSe film can be formed from stacked CZT precursor deposited using flow cell.

Resume

In summary, selenization step where Cu-Zn-Sn precursor is converted to $Cu_2SnZnSe_4$ compound is a very complex process. Firstly, the initial CZT composition affects CZTSe morphology and it was demonstrated that precursors with stoichiometric Zn/Sn ratio and Sn-rich composition resulted in very poor quality of CZTSe morphology. The effect was even more pronounced under low pressure selenization conditions. On the other hand, preheating of CZT precursors at T > 300 °C where all metals are fully alloyed resulted in significantly improved CZTSe morphology. Furthermore, CZT composition strongly affected solar cell performance, and relatively high efficient solar cells were achieved only from precursor with Cu-poor and Zn-rich composition. Formation of defects in CZTSe was investigated by photoluminescence spectroscopy. It was shown, that the more Cu-poor and Zn-rich composition is the more V_{Cu} defects are dominant, which are necessary for efficient solar cell.

Selenization conditions have to be carefully chosen in order to achieve high quality CZTSe layer. The amount of Se in the container has to be enough to contain saturated Se pressure during selenization at particular temperature. Otherwise the decomposition of CZTSe could occur, which can be detrimental for solar cell performance. On the other hand, as it was shown annealing at high temperature and saturated Se pressure resulted in fully selenized Mo substrate. Therefore selenization temperature, background pressure and amount of Se have to be optimized to decrease the formation of $MoSe_2$ as well as to inhibit the decomposition of CZTSe. The selenization conditions, where the formation of $MoSe_2$ was inhibited to minimum were found to be 510 °C, 15 minutes, 10 mg of Se and 1 bar background pressure for co-electroplated CZT precursor. However large amount of ZnSe was detected in particular sample. Consequently, two-step selenization approach

was tested, as a compromise of annealing at low pressure and high temperature, without fully selenizing Mo. As a result uniform in composition and morphology over 1x2.5 cm^2 area CZTSe layers have been obtained, which showed as high as 1.9% solar cell efficiency. Low values of solar cell efficiency could be caused by the existence of shunt paths and in turn low R_{sh}. The suitable selenization conditions for co-deposited and stacked layer CZT precursor are different and further research on selenization of sequentially deposited Cu/Sn/Cu/Zn precursor is required.

Main results and conclusions

From the study presented in this work, we can point out the main results and conclusions:

1. The optimal potential for electrochemical Cu-Zn-Sn co-deposition under hydrodynamic conditions in the solution containing 20 mM of $CuSO_4$, 18 mM of $ZnSO_4$, 10 mM of $SnSO_4$ and 100 mM of Na_3Cit was found to be -1.4 V vs $Ag/AgCl/KCl_{sat}$ reference electrode. Deposited films were uniform, smooth and well adherent to the Mo substrate. The co-deposition rate increased from 0.05 μm/min in still solution up to 0.24 μm/min in the stirred one, i.e. the deposition time was approximately 4.8 times shorter.
2. The presented electrochemical deposition setup with flow cell proved to be suitable for Cu, Sn and Zn thin film electrodeposition. Among tested electrolytes, Sn and Zn films deposited from methanesulfonic and commercial solutions, respectively, were uniform and well adherent. Optimal electrolyte flow rate for Cu, Sn and Zn films was in the range of 300 – 400 ml/min and deposition potential for Cu and Sn was in the range of -0.93 – -1.0 V vs Pt reference electrode, whereas optimal current density for Zn deposition was found to be 20 mA/cm^2.
3. The as-deposited Cu-Zn-Sn precursor contained hexagonal η-$Cu_{6.26}Sn_5$, cubic γ-Cu_5Zn_8 and hexagonal ε-$CuZn_5$ intermetallic phases and only Sn was observed in pure metallic form. The formation of hexagonal η-$Cu_{6.26}Sn_5$ phase was confirmed by HR-XRD measurements in contrast to monoclinic η´-Cu_6Sn_5 phase reported in literature. After preheating at T > 300 °C in Zn-rich (Zn/Sn >1) and Cu-poor (Cu/(Sn+Zn)<1) CZT precursor only η-$Cu_{6.26}Sn_5$ and γ-Cu_5Zn_8 phases were detected. After preheating at T > 200 °C the crystal lattice of γ-Cu_5Zn_8 was always

enlarged, because of the formation of substitution solid solution of Sn in the latter phase.

4. Because of the probable formation of volatile tin selenide compound during selenization, CZTSe film morphology contained many faults and burst bubbles. The latter effect was pronounced in Sn-rich (Zn/Sn $\leq$ 1) CZT precursor and under low (1 mbar) background pressure conditions.
5. The morphologic defects (burst bubbles and hillocks) were greatly reduced when preheating at *T* > 300 °C was applied to CZT precursor. The elimination of pure Sn phase is thought to be the main reason of improved CZTSe morphology.
6. Preheating at *T* > 300 °C and Cu-poor, Zn-rich initial CZT composition was necessary to achieve less defective and smooth CZTSe morphology and relatively efficient (> 2%) CZTSe solar cells.
7. Champion CZTSe solar cell fabricated from Zn-rich and Cu-poor electrochemically co-deposited and preheated at 350 °C for 10 min under 1 bar Ar pressure CZT precursor, demonstrated η = 2.7 %, V_{OC} = 233 mV, j_{SC} =28.8 mA/cm^2 and FF =39%. CZT precursor was selenized at 550 °C for 30 min under 1 bar Ar pressure with 10 mg of Se.
8. The most detrimental CZTSe solar cell parameter was found to be shunt resistance (R_{sh}), which was in the range of 10-30 Ω·cm^2 in comparison to typical 100-400 Ω·cm^2 values reported in the literature for CZTSe solar cells. Low R_{sh} was associated with the lack of CZTSe film integrity and existence of shunt paths, which in turn presumably were caused by the hydrogen evolution during electrodeposition of Cu-Zn-Sn.

List of articles

1. R. Kondrotas, R. Juškėnas, A. Naujokaitis, G. Niaura, Z. Mockus, S. Kanapeckaitė, B. Čechavičius, K. Juškevičius, E. Saucedo, Y. Sanchez, Investigation of selenization process of electrodeposited Cu-Zn-Sn precursor for $Cu_2ZnSnSe_4$ thin film solar cells*, Thin solid Films* (imparted to journal).
2. R. Kondrotas, R. Juškėnas, A. Naujokaitis, A. Selskis, R. Giraitis, Z. Mockus, S. Kanapeckaitė, G. Niaura, H. Xie, Y. Sanchez, E. Saucedo, Characterization of $Cu_2ZnSnSe_4$ solar cells prepared from electrochemically co-deposited Cu-Zn-Sn alloy, *Sol. Energy Mater. Sol. Cells* **132** 21-28 (2015).
3. R. Juškėnas, D. Avižinis, P. Kalinauskas, A. Selskis, R. Giraitis, V. Pakštas, V. Karpavičienė, S. Kanapeckaitė, Z Mockus, R. Kondrotas, XRD, SEM and photoelectrochemical characterization of ZnSe electrodeposited on Cu and Cu-Sn substrates, *Electrochim. acta* **70**, 118-123 (2012).

List of international conferences

1. V. Pakštas, Z. Mockus, R. Giraitis, R. Kondrotas, A. Naujokaitis, G. Stalnionis, S. Stanionytė, V. Karpavičienė, R. Juškėnas, XRD studies of homogenization and selenization of electrochemically co-deposited Cu-Zn-Sn,Chemija ir Cheminė Technologija 2015, 2015 (Vilnius).
2. R. Juškėnas, G. Niaura, Z. Mockus, S. Kanapeckaitė, R. Giraitis, R. Kondrotas, A. Naujokaitis, Advanced XRD studies of CZTSe and Cu-Zn-Sn precursor layer, 29th European PV solar energy conference and exhibition (Amsterdam, 2014.09) p. 237.
3. A. Naujokaitis, R. Kondrotas, R. Juškėnas, K. Arlauskas, R. Giraitis, Z. Mockus, S. Kanapeckaitė, H. Xie, Y. Sanchez, E. Saucedo, CZTSSe solar

cells fabricated from electrochemically co-deposited precursor, 29th European PV solar energy conference and exhibition (Amsterdam, 2014.09) p. 234.

4. R. Kondrotas, Z. Mockus, S. Kanapeckaitė, A. Naujokaitis, V. Karpavičienė, R. Juškėnas, Formation and characterization of Cu, Zn, Sn layers for a thin film photovoltaics, 11-oji Lietuvos chemikų tartpautinė konferencija CHEMIJA 2013 (Vilnius, 2013.11) p. 3.
5. R. Juškėnas, Z. Mockus, S. Kanapeckaitė, A. Selskienė, R. Giraitis, G. Niaura, R. Kondrotas, A. Koroliov, High quality $Cu_2ZnSnSe_4$ layer formed using electrochemically co-deposited Cu-Zn-Sn precursor, 27th European PV solar energy conference and exhibition (Frankfurt, 2012.09) p. 242.

List of local conferences

6. R. Kondrotas, Elektrochemiškai suformuotų CZTSe, CZTS ir CZTSSe saulės elementų tyrimas, Doktorantų stažuotės užsienio mokslo centruose 2012-2013, 2013.
7. R. Kondrotas, R. Juškėnas, K. Juškevičius, A. Selskis, V. Pakštas, Saulės elemento Mo apatinio kontakto magnetroninis formavimas ir charakterizavimas, Medžiagų inžinierija 2012 (Kaunas 2012) p. 5.

Recommendations

Flow cell design or flow system has to be improved in order to achieve laminar flow over whole electrode surface. One of the options is to widen and increase volume of flow cell, but it would require large volume of electrolyte solution and whole circulation system has to be scaled up appropriately. Another possible option is to decrease flow cell volume (decrease distance between working and counter electrode) and to make the cross-sectional area of inlet and outlet the same as hoses.

Even though stirring was introduced in co-deposition, CZT layer was thicker at the edges of electrode. Therefore the stirring in classical three-electrode cell has to be improved in order to eliminate the formation of vortex and preferential deposition at the edges of working electrode.

In general because of the peculiarities of CZTSe formation the composition of Cu-Zn-Sn precursor should be reconsidered and the greater attention given to the Cu/Zn ratio rather than Zn/Sn. What is more the thickness of electrodeposited Cu-Zn-Sn films should be higher (at least over 550 nm) in order to reduce the morphology faults, caused by hydrogen evolution.

Acknowledgments

I am sincerely and mostly grateful to my supervisor Remigijus Juškėnas for the help, valuable discussions and guidance during my PhD studies, for challenging me to become an independent scientist.

I would also like to express my gratitude to Stasė Kanpeckaitė and Zenius Mockus for the great help with electrochemical co-deposition of CZT precursor, for constructive consultations regarding electrochemistry and electrochemical deposition.

Furthermore, I would like to thank Kęstutis Juškevičius for finding time and even working on weekends to fabricate Mo electrodes. Big thanks to my colleague Raimundas Giraitis for the help with preliminary annealing and selenization processes. I am also deeply thankful to Gediminas Niaura for precise and comprehensive Raman measurements and data interpretation.

Special thanks to SEM and XRD experts Algirdas Sėlskis, Giedrius Stalnionis, Vidas Pakštas and Sandra Stanionytė for conducting morphology, cross-section and phase composition measurements and providing comprehensive data. My profound gratitude to Arnas Naujokaitis, who stayed up late with me to help with a SEM measurements. Overall I would like to thank to all members of Department of Characterization of Materials Structure for the support and help during all PhD studies.

I would also like to express my deepest gratitude to the Solar Energy Materials and Systems group of IREC and Edgardo Saucedo for very sincere hospitality, encouragement and friendly atmosphere during internship at IREC.

The cooperation would not be possible without grant I received. I am grateful to the Lithuania Research council

Last, but not least I thank my family, friends for the unconditional support during the time of writing dissertation.

Notations and abbreviations

CIGS, Cu(In, Ga)Se2
CZTSe, $Cu_2ZnSnSe_4$
CZTS, Cu_2ZnSnS_4
CZTSe(S), $Cu_2ZnSn(S/Se)_4$
CZT, Cu-Zn-Sn
CFA, conventional furnace annealing
DSC, differential scanning calorimetry
EDX, energy dispersive x-ray spectroscopy
E_g, band gap
FIB, focused ion beam
NHE, normal hydrogen electrode
PCE, power conversion efficiency
PL, photoluminescence
RTA, rapid thermal annealing
SEM, scanning electron microscopy
SCE, saturated calomel electrode
TCO, transparent – conducting oxide
XPS, x-ray photoelectron spectroscopy
XRD, x-ray diffraction

a, activity
A, area
α, absorption coefficient, coordination number
β_α, equilibrium constant
C_R^*, bulk concentration of reduced specie
C_O^*, bulk concentration of oxidized specie
d, thickness
$E^{0`}$, formal potential
E^0, standard potential
E, potential
F, Faradays number (96485 C mol^{-1})
FF, fill factor
I_0, dark current
I_L, photo generated current
I_{SC}, short-circuit current
j, current density
j_{SC}, short-circuit current density
L, ligand
M, molar mass
M^{z+}, metal ion
n, number of moles, diode ideality factor
η, efficiency
R, ideal gas constant
$\mathrm{Re}\,d$, reduced specie
R_s, series resistance
R_{sh}, shunt resistance
ρ, density
S, flow rate
T, temperature
Ox, oxidized specie
V_{OC}, open-circuit voltage
ν, reaction rate
Q, electrical charge
z, number of electrons

Bibliography

[1] "Intergovernmental Panel on Climate Change", www.ipcc.ch. Last visited 2014.10.18.

[2] BP Statistical review of world energy June 2014, 63th edition.

[3] "The balance of power in the Earth-Sun system", www.nasa.gov. Last visited 2014.10.18

[4] G. Masson, M. Latour, M. Rekinger, I.T. Theologitis, M. Papoutsi, Global market outlook European for photovoltaics 2013-2017, *Photovoltaic Industry Association*.

[5] http://en.wikipedia.org/wiki/Abundance_of_elements_in_Earth%27s_crust. Last visited 2015.02.10.

[6] M. Powalla, P. Jackson, D Hariskos, S. Paetel, W. Wittle, R. Wurz, E. Lotter, R. Menger, W. Wischmann, CIGS Thin-film solar cell with improved efficiency of 20.8%, *29th European PV solar energy conference and exhibition* (Amsterdam, 2014.09.22-2014.09.26) *Conference program* p. 2.

[7] J. Kim, H. Hiroi, T. K. Todorov, O. Gunawan, M. Kuwahara, T. Gokmen, D. Nair, M. Hopstaken, B. Shin, Y. S. Lee, W. Wang, H. Sugimoto, D. B. Mitzi, High efficiency $Cu_2ZnSn(S,Se)_4$ solar cells by applying a double In_2S_3/CdS emitter, *Adv. Mater*. **26**(44) 7427-7431 (2014).

[8] http://www.bine.info/en/topics/renewable-energy-sources. Last visited 2014.10.18

[9] M. Hartmann, M. Schmidt, A. Jasenek, H.W. Schock, F. Kessler, K. Herz, M. Powalla, Flexible and light weight substrates for $Cu(In,Ga)Se_2$ solar cells and modules, *Proc. of the 28th IEEE Photovoltaic Specialists Conf*., Anchorage, p. 638 (2000).

[10] O. Tober, J. Wienke, M. Winkler, J. Penndorf, J. Griesche, Current status and future prospects of CISCuT based solar cells and modules, *Mater. Res. Soc. Symp. Proc.* **763**, 371 (2003).

[11] K. Ramanathan, J. Keane, R. Noufi, Properties of high-efficiency CIGS thin-film solar cells, *31st IEEE Photovoltaic Specialists Conf.*, Lake Buena Vista (2005).

[12] P. Jackson, D. Hariskos, R. Wuerz, W. Wischmann, M. Powalla, Compositional investigation of potassium doped Cu(In,Ga)Se_2 solar cells with efficiencies up to 20.8%, *Phys. Status solidi RRL* **8**(3), 219-222 (2014).

[13] V. Probst, W. Stetter, W. Riedl, H. Vogt, M. Wendl, H. Calwer, S. Zweigart, K. D. Ufert, B. Freiensten, H. Cerva, F.H. Karg, Rapid CIS-process for high efficiency PV-modules: development towards large area processing, *Thin solid films* **387**, 262-267 (2001).

[14] M. Krunks, O. Kijatkina, H. Rebane, I. Oja, V. Mikli, A. Mere, Composition of $CuInS_2$ thin films prepared by spray pyrolysis, *Thin solid films* **403**, 71-75, (2002).

[15] V. Kapur, A. Bansal, P. Le, O. I. Asensio, Non-vacuum processing of $CuIn_{1-x}Ga_xSe_2$ solar cells on rigid and flexible substrates using nanoparticle precursor inks, *Thin solid films* **431-432**, 53-57 (2003).

[16] R. N. Bhattacharya, M. Oh, Y. Kim, CIGS-based solar cells prepared from electrodeposited precursor films, *Sol. Energy Mater. Sol. Cells* **98**, 198-202 (2012).

[17] D. Lincot, J.F. Guillemoles, S. Taunier, D. Guimard, J. Sicx-Kurdi, A. Chaumont, O. Roussel, O. Ramdani, C. Hubert, J.P. Fauvarque, N. Bodereau, L. Parissi, P. Panheleux, P. Fanouillere, N. Naghavi, P.P. Grand, M. Benfarah, P. Mogensen, O. Kerrec, Chalcopyrite thin film solar cells by electrodeposition, *Sol. Energy* **77(6)**, 725-737 (2004).

[18] S. Spiering, A. Eicke, D. Hariskos, M. Powalla, N. Naghavi, D. Lincot, Large-area Cd-free CIGS solar modules with In_2S_3 buffer layer deposited by ALCVD, *Thin solid films* **451-452**, 562-566 (2004).

[19] R. Bhattacharya, M A. Contreras, G. Teeter, 18.5% Copper Indium gallium diselenide (CIGS) device using single-layer chemical bath deposited ZnS(O, OH), *Jpn. J. Appl. Phys* **43**, L1475-L1476 (2004).

[20] T. Nakada, M. Hongo, E. Hayashi, Band offset of high efficiency CBD-ZnS/CIGS thin film solar cells, *Thin solid films* **431-432**, 242-248 (2003).

[21] K. Korosec, "Solar CIGS market shakeout: less capital and only a few winners", www.smartplanet.com, last visited 2015.02.10.

[22] R. Nitsche, D. F. Sargent, P. Wild, Crystal growth of quaternary 1_2246_4 chalcogenides by iodine vapor transport, *J. Cryst. Growth* **1**, 52-53 (1967).

[23] K. Ito, T. Nakazawa, Electrical and optical properties of stannite-type quaternary semiconductor thin films, *Jpn. J. Appl. Phys*. **27**, 2094-2097 (1988).

[24] H. Katagiri, N. Sasaguchi, S. Hando, S. Hoshino, J. Ohashi, T. Yokota, Preparation and evaluation of Cu_2ZnSnS_4 thin films by sulfurization of e-B evaporated precursors, *Sol. Energy Mater. Sol. Cells* **49**, 407-414 (1997).

[25] H. Katagiri, et al., *Tech. Dig. Photovoltaic Science and Engineering Conf*. 11, Sapporo, p. 647 (1999).

[26] H. Katagiri, et al., *Proc. World Conf. on Photovoltaic Energy Conversion-3*, Osaka, p. 2874 (2003).

[27] H. Katagiri, K. Jimbo, S. Yamada, T. Kamimura, W. S. Maw, T. Fukano, T. Ito, T. Motohiro, Enhanced conversion efficiencies of Cu_2ZnSnS_4-based thin film solar cells by using preferential etching technique, *Appl. Phys Express* **1,** 041201 (2008).

[28] I. Repins, C. Beall, N. Vora, C. DeHart, D. Kuciauskas, P. Dippo, B. To, J. Mann, W. Hsu, A. Goodrich, R. Noufi, Co-evaporated $Cu_2ZnSnSe_4$ films and devices, *Sol. Energy Mater. Sol. Cells* **101,** 154-159 (2012).

[29] Th. M. Friedlmeier, N. Wieser, T. Walter, H. Dittrich, H. W. Schock, *Proceedings of the 14th European conference of photovoltaic science and engineering and exhibition*, Belford (1997).

[30] K. Jimbo, R. Kimura, T. Kamimura, S. Yamada, W. S. Maw, H. Araki, K. Oishi, H. Katagiri, Cu_2ZnSnS_4-type thin film solar cells using abundant materials, *Thin solid films* **515**(15), 5997-5999 (2007).

[31] T. K. Todorov, K. B. Reuter, D. B. Mitzi, High-efficiency solar cell with earth-abundant liquid-processed absorber, *Adv, Energy Mater.* **22** E156-E159 (2010).

[32] T. Todorov, O. Gunawan, S. J. Chey, T. Goislard de Monsabert, A. Prabhakar, D. B. Mitzi, Progress towards marketable earth-abundant chalcogenide solar cells, *Thin solid films* **519**, 7378-7381 (2011).

[33] A. Barkhouse, O. Gunawan, T. Gokmen, T. K. Todorov, D. B. Mitzi, Device characteristics of a 10.1 % hydrazine-processed $Cu_2ZnSn(Se,S)_4$ solar cell, *Prog. Photovolt. Res. Appl*. **20**, 6-11 (2012).

[34] T. K. Todorov, J. Tang, S. Bag, O. Gunawan, T. Gokmen, Y. Zhu, D. B. Mitzi, Beyond 11% efficiency: characteristics of state-of-art $Cu_2ZnSn(S, Se)_4$ solar cells, *Adv. Energy Mater.* **3,** 34-38 (2013).

[35] T. Maeda, S. Nakamura, T. Wada, First principles calculations of defect formation in In-free photovoltaic semiconductors Cu_2ZnSnS_4 and $Cu_2ZnSnSe_4$, *Jpn. J. Appl. Phys*. **50,** 04DP07 (2011).

[36] S. Chen, J. Yang, X. G. Gong, A. Walsh, S. Wei, Intrinsic point defects and complexes in the quaternary kesterite semiconductor Cu_2ZnSnS_4, *Phys. Rev. B* **81,** 245205 (2010).

[37] I. D. Olekseyuk, I. V. Dudchak, L. V. Piskach, Phase equilibria in the Cu_2S-ZnS-SnS_2 system, *J. Alloys Compd.* **368**, 135-143 (2004).

[38] A. Nagaoka, K. Yoshino, H. Taniguchi, T. Taniyama, H. Miyake, Preparation of Cu_2ZnSnS_4 single crystals from Sn solutions, *J. Cryst. Growth* **341**, 38-41 (2012).

[39] A. Nagaoka, K. Yoshino, H. Taniguchi, T. Taniyama, H. Miyake, Growth of $Cu_2ZnSnSe_4$ single crystals from Sn solutions, *J. Cryst. Growth* **354**, 147-151 (2012).

[40] C. P. Björkman, J. Scragg, H. Flammersberger, T. Kubart, M. Edoff, Influence of precursor sulfur content on film formation and compositional changes in Cu_2ZnSnS_4 film and solar cells, *Sol. Energy Mater. Sol. Cells* **98**, 110-117 (2012).

[41] O. Vigil-Galán, M. Espíndola-Rodríguez, M. Courel, X. Fontané, D. Sylla, V. Izquierdo-Roca, A. Fairbrother, E. Saucedo, A. Pérez-Rodríguez, Secondary phases dependence on composition ratio in sprayed Cu_2ZnSnS_4 thin films and its impact on the high power conversion efficiency, *Sol. Energy Mater. Sol. Cells* **117**, 246-250 (2013).

[42] M. Dimitrievska, A. Fairbrother, V. Izquierdo-Roca, A. Pérez-Rodríguez, E. Saucedo, Two ideal compositions for kesterite-based solar cell devices, *Photovoltaic Specialist Conference IEEE 40th* (2014).

[43] H. Katagiri, K. Jimbo, M. Tahara, H. Araki, K. Oishi, The influence of the composition ratio on CZTS-based thin film solar cells, *Mater. Res. Soc. Symp. Proc.* **1165**, 1165-M04-01 (2009).

[44] S. Delbos, Kesterite thin films for photovoltaics: a review, *EPJ Photovoltaics* **3**, 35004 (2012).

[45] S. Chen, A. Walsh, X. Gong, S. Wei, Classification of lattice defects in the kesterite Cu_2ZnSnS_4 and $Cu_2ZnSnSe_4$ earth-abundant solar cell absorbers, *Adv. Mater.* **25**, 1522-1539 (2013).

[46] A. Redinger, S. Siebentritt, Co-evaporation of $Cu_2ZnSnSe_4$ thin films, *Appl. Phys. Lett.* **97**, 092111 (2010).

[47] F. Hergert, R. Hock, Predicted formation reactions for solid-state syntheses of the semiconductor materials Cu_2SnX_3 and Cu_2ZnSnX_4 (X=S, Se) starting from binary chalcogenides, *Thin solid films* **515**, 5953-5956 (2007).

[48] A. Fairbrother, X. Fontané, V Izquierdo-Roca, M. Espíndola-Rodríguez, S. López-Marino, M. Placidi, L. Calvo-Barrio, A. Pérez-Rodríguez, E. Saucedo, On the formation mechanisms of Zn-rich Cu_2ZnSnS_4 films prepared by sulfurizaion of metallic stacks, *Sol. Energy Mater. Sol. Cells* **112**, 97-105 (2013).

[49] R. Schurr, A Holzing, S. Jost, R. Hock, T Vob, J. Schulze, A. Kirbs, A. Ennaoui, M. Lux-Steiner, A.. Weber, I. Kotschau, H. W. Schock, The crystallization of Cu_2ZnSnS_4 thin film solar cell absorbers from co-electroplated Cu-Zn-Sn precursors, *Thin solid films* **517**, 2465-2468 (2009).

[50] H. Yoo, R. A. Wibowo, A. Holzing, R. Lechner, J. Palm, S. Jost, M. Gowtham, F. Sorin, B. Louis, R. Hock, Investigation of the solid state reactions by time-resolved X-ray diffraction while crystallizing kesterite $Cu_2ZnSnSe_4$ thin films, *Thin solid films* **535**, 73-77 (2013).

[51] R. A. Wibowo, S. A. Moeckel, H. Yoo, Ch. Hetzner, A. Hoelzing, P. Wellmann, R. Hock, Intermetallic compounds dynamic formation during annealing of stacked elemental layers and its influences on the crystallization of $Cu_2ZnSnSe_4$ films, *Mater. Chem. Phys.* **142**, 311-317 (2013).

[52] A. Redinger, D. M. Berg, P. J. Dale, S. Siebentritt, The consequences of kesterite equilibria for efficient solar cells, *J. Am. Chem. Soc.* **133**, 3320-3323 (2011).

[53] A. Redinger, M. Mousel, R. Djemour, L. Gutay, N. Valle, S. Siebentritt, $Cu_2ZnSnSe_4$ thin film solar cells produced via co-evaporation and annealing including a $SnSe_2$ capping layer, *Prog. Photovolt: Res. Appl.* **22**(1), 51-57 (2014).

[54] S. López-Marino, M. Placidi, A. Pérez-Tomás, J. Llobet, V. Izquierdo-Roca, X. Fontane, A. Fairbrother, M. Espíndola-Rodríguez, D. Sylla, A. Pérez-Rodríguez, E. Saucedo, Inhibiting the absorber/Mo-back contact decomposition reaction in $Cu_2ZnSnSe_4$ solar cells: the role of a ZnO intermediate nanolayer, *J. Mater Chem. A* **29,** 8338-8343 (2013).

[55] J. J. Scragg, J. T. Watjen, M. Edoff, T. Ericson, T. Kubart, Ch. Platzer-Bjorkman, A detrimental reaction at the molybdenum back contact in $Cu_2ZnSn(S, Se)_4$ thin film solar cells*, J. Am. Chem. Soc.* **134**, 19330-19333 (2012).

[56] W. Li, J. Chen, H. Cui, F. Liu, X. Hao, Inhibiting MoS_2 formation by introducing a ZnO intermediate layer for Cu_2ZnSnS_4 solar cells, *Mater. Lett.* **130**, 87-90 (2014).

[57] D. Kuo, J. Hsu, A. D. Saragih, Effects of the metallic target compositions on the absorber properties and the performance of $Cu_2ZnSnSe_4$ solar cell devices fabricated on TiN-coated Mo/glass substrates, *Mater. Sci. Eng. B* **186**, 94-100 (2014).

[58] B. Shin, Y. Zhu, N. A. Bojarczuk, J. Chey, S. Guha, Control of an interfacial $MoSe_2$ layer in $Cu_2ZnSnSe_4$ thin film solar cells: 8.9% power conversion efficiency with a TiN diffusion barrier, *Appl. Phys. Lett.* **101**, 053903 (2012).

[59] K. Wang, O. Gunawan, T. Todorov, B. Shin, S. J. Chey, N. A. Bojarczuk, D. Mitzi, S. Guha, Thermally evaporated Cu_2ZnSnS_4 solar cells, *Appl. Phys. Lett*. **97,** 143508 (2010).

[60] J. T. Watjen, J. Engman, M. Edoff, Ch. Platzer-Bjorkman, Direct evidence of current blocking by ZnSe in $Cu_2ZnSnSe_4$ solar cells, *Appl. Phys. Lett.* **100**, 173510 (2012).

[61] M. Mousel, A. Redinger, R. Djemour, M. Arasimowicz, N. Valle, P. Dale, S. Siebentritt, HCl and Br2-MeOH etching of $Cu_2ZnSnSe_4$ polycrystalline absorbers*, Thin solid films* **535**, 83-87 (2013).

[62] K. Timmo, M. Altosaar, J. Raudoja, M. Grossberg, M. Danilson, O. Volobujeva,E. Mellikov,. Chemical etching of $Cu_2ZnSn(S, Se)_4$ monograin powder, *Photovoltaic Specialists Conference 35th IEEE* (2010).

[63] A. Fairbrother, E. Garcia-Hemme, V. Izquierdo-Roca, X. Fontané, F. A. Pulgarín-Agudelo, O. Vigil-Galán, A. Pérez-Rodríguez, E. Saucedo, Development of a selective chemical etch to improve the conversion efficiency of Zn-rich Cu_2ZnSnS_4 solar cells, *J. Am. Chem. Soc.* **134**, 8018-8021 (2012).

[64] S. López-Marino, Y. Sánchez, M .Placidi, A. Fairbrother, M. Espíndola-Rodríguez, X. Fontané, V. Izquierdo-Roca, J. López-García, L. Calvo-Barrio, A. Pérez-Rodríguez, E. Saucedo, ZnSe etching of Zn-rich $Cu_2ZnSnSe_4$: an oxidation route for improved solar-cell efficiency, *Chem. Eur. J.* **19**(44), 14814-14822 (2013).

[65] W. Hsu, I. Repins, C. Beal, C. Dehart, G. Teeter, B. To, Y. Yang, R. Noufi, The effect of Zn excess on kesterite solar cells, *Sol. Energy Mater. Sol. Cells* **113**, 160-164 (2013).

[66] X. Zeng, K. F. Tai, T. Zhang, C. W. J. Ho, X. Chen, A. Huan, T. C. Sum, L. H. Wong, $Cu_2ZnSn(S, Se)_4$ kesterite solar cell with 5.1% efficiency using spray pyrolysis of aqueous precursor solution followed by selenization, *Sol. Energy Mater. Sol. Cells* **124**, 55-60 (2014).

[67] A. Neisser, C. Waldauf, S. Moser, D M. Crystalsol, K. Ernits, T. Holopainen, Printing of Large area flexible CZTS solar modules, *29th European photovoltaic solar energy conference and exhibition*, Amsterdam (2014).

[68] F. Jiang, S. Ikeda, T. Harada, M. Matsumura, Pure sulfide Cu_2ZnSnS_4 thin film solar cells fabricated by preheating an electrodeposited metallic stack, *Adv. Energy Mater.* **4**(7) 2014.

[69] J. Yoon, S. Cho, W. M. Kim, J. Park, Y. Baik, T. S. Lee, T. Seong, J. Jeong, Optical analysis of the microstructure of a Mo back contact for Cu(In, Ga)Se_2 solar cells and its effects on Mo film properties and Na diffusivity, *Sol. Energy Mater. Sol. Cells* **95**, 2959-2964 (2011).

[70] J. J. Scofield, A. Duda, D. Albin, Sputtered molybdenum bilayer back contact for copper indium diselenide-based polycrystalline thin-film solar cells, *Thin solid films* **260**(1), 26-31 (1995).

[71] Z. Li, E. Cho, S. J. Kwon, Molybdenum thin film deposited by in-line DC magnetron sputtering as a back contact for Cu(In, Ga)Se_2 solar cells, *Appl. Surf. Sci.* **257**, 9682-9688 (2011).

[72] S. A. Pethe, E. Takahashi, A. Kaul, N. G. Dhere, Effect of sputtering process parameters on film properties of molybdenum back contact, *Sol. Energy Mater. Sol. Cells* **100**, 1-5 (2012).

[73] H. Wu, S. liang, Y. Lin, C. Ni, H. Bor, D. Tsai, F. Shieu, Structure and electrical properties of Mo back contact for Cu(In, Ga)Se_2 solar cells, *Vacuum* **86**, 1916-1919 (2012).

[74] M. Jubault, L. Ribeaaucourt, E. Chassaing, G. Renou, D. Lincot, F. Donsanti, Optimization of molybdneum thin films for electrodeposited CIGS solar cells, *Sol. Energy Mater. Sol. Cells* **95**, S26-S31 (2011).

[75] M. A. Martinez, C. Guillen, Effect of r.f.-sputtered Mo substrate on the microstructure of electrodeposited $CuInSe_2$ thin films, *Surf. Coat. Technol.* **110**, 62-67 (1998).

[76] X. Zhu, Z. Zhou, Y. Wang, L. Zhang, A. Li, F. Huang, Determining factor of $MoSe_2$ formation in Cu(In, Ga)Se_2 solar cells, *Sol. Energy Mater. Sol. Cells*, **101**, 57-61 (2012).

[77] V.K. Kapur, B. M. Basol, A. Halani, C. R. Leidholm, A. Minnick, *12th European photovoltaic energy conference*, (1994).

[78] D. R. Johnson, Microstructure of electrodeposited CdS/CdTe cells, *Thin solid films* **361-362**, 321-326 (2000).

[79] C. J. Hibberd, E. Chassaing, W. Liu, D. B. Mitzi, D. Lincot, A. N. Tiwari, Non-vacuum methods for formation of Cu(In, Ga)(Se, $S)_2$ thin film photovoltaic absorbers, *Prog. Photovolt. Res. Appl.* **18**(20), 434-452 (2010).

[80] A. Ennaoui, M. Lux-Steiner, A Weber, D. Abou-Ras, I Kotschau, H. W. Schick, R. Schurr, A. Holzing, S. Jost, R. Hock, T. Vob, J. Schulze, A. Kirbs, Cu_2ZnSnS_4 thin film solar cells from electroplated precursors: novel low-cost perspective, *Thin solid films* **517**, 2511-2514 (2009).

[81] H. Araki, Y. Kubo, K. Jimbo, W. S. Maw, H. Katagiri, M. Yamazaki, K. Oishi, A. Takeuchi, Preparation of Cu_2ZnSnS_4 thin films by sulfurization of co-electroplated Cu-Zn-Sn precursors, *Phys. Status Solidi C* **6**, 1266-1268 (2009).

[82] Y. Zhang, C. Liao, K. Zong, H. Wang, J. Liu, T. Jiang, J. Han, G. Liu, L. Cui, Q. Ye, H. Yan, W. Lau, $Cu_2ZnSnSe_4$ thin film solar cells prepared by rapid thermal annealing of co-electroplated Cu-Zn-Sn precursors, *Sol. Energy* **94**, 1-7 (2013).

[83] Y. Li, T. Yuan, L. Jiang, Z. Su, F. Liu, Growth and characterization of Cu_2ZnSnS_4 photovoltaic thin films by electrodeposition and sulfurization, *J. Alloys Compd.* **610**, 331-336 (2014).

[84] J. Li, T. Ma, M. Wei, W. Liu, G. Jiang, C. Zhu, The $Cu_2ZnSnSe_4$ thin films solar cells synthesized by electrodeposition route*, Appl. Surf. Sci* **258**, 6261-6265 (2012).

[85] X. He, H. Shen, W. Wang, J. Pi, Y. Hao, X. Shi, Synthesis of Cu_2ZnSnS_4 films from co-electrodeposited Cu-Zn-Sn precursors and their microstructural and optical properties, *Appl. Surf. Sci.* **282**, 765-769 (2013).

[86] Z. Chen, L. Han, L. Wan, C. Zhang, H. Niu, J. Xu, $Cu_2ZnSnSe_4$ thin films prepared by selenization of co-electroplated Cu-Zn-Sn precursors, *Appl. Surf. Sci.* **257**, 8490-8492 (2011).

[87] J. Jeon, K. D. Lee, L. S. Oh, S. Seo, D. Lee, H. Kim, J. Jeong, M. J. Ko, B. Kim, H. J. Son, J. Y. Kim, Highly efficient copper-zinc-tin-selenide (CZTSe) solar cells by electrodeposition, *ChemSusChem* **7**(4), 1073-1077 (2014).

[88] C. Gougaud, D Rai, S. Delbos, E. Chassaing, D. Lincot, Electrochemical studies of one-step electrodeposition of Cu-Zn-Sn layers from aqueous electrolytes for photovoltaic applications, *J. Electrochem. Soc.* **160**(10), D485-D494 (2013).

[89] J. J. Scragg, P. J. Dale, L. M. Peter, Synthesis and characterization of Cu_2ZnSnS_4 absorber layers by an electrodeposition-annealing route, *Thin solid films* **517**, 2481-2484 (2009).

[90] J. J. Scragg, D. M. Berg, P. J. Dale, A 3.2% efficient kesterite device from electrodeposited stacked elemental layers, *J. Electroanal. Chem.* **646**, 52-59 (2010).

[91] J.J. Scragg, Studies of Cu_2ZnSnS_4 films prepared by sulfurisation of electrodeposited precursors, PhD thesis, University of Bath (2010).

[92] S. Ahmed, K. B. Reuter, O. Gunawan, L. Guo, L. T. Romankiw, H. Deligianni, A high efficiency electrodeposited Cu_2ZnSnS_4 solar cell, *Adv. Energy Mater.* **2**, 253-259 (2012).

[93] L. Guo, Y. Zhu, O. Gunawan, T. Gokmen, V. R. Deline, S. Ahmed, L. T. Romankiw, H. Deligianni, Electrodeposited $Cu_2ZnSnSe_4$ thin film solar cell with 7% power conversion efficiency, *Prog. Photovollt: Res. Appl*. **22**(1), 58-68 (2014).

[94] Y. Lin, S. Ikeda, W. Septina, Y. Kawasaki, T. Harada, M. Matsumura, Mechanistic aspects of preheating effects of electrodeposited metallic precursors on structural and photovoltaic properties of Cu_2ZnSnS_4 thin films, *Sol. Energy Mater. Sol. Cells* **120**, 218-225 (2014).

[95] E. M. Mkawi, K. Ibrahim, M. K. M. Ali, M. A. Frrukh, N. K. Allam, Influence of precursor thin films stacking order on the properties of Cu_2ZnSnS_4 thin films fabricated by electrochemical deposition method, *Superlattices Microstruct.* **76**, 339-348 (2014).

[96] M. Meng, L. Wan, P. Zou, S. Miao, J. Xu, $Cu_2ZnSnSe_4$ thin films prepared by selenization of one-step electrochemically deposited Cu-Zn-Sn-Se precursors*, Appl. Surf. Sci.* **273**, 613-616 (2013).

[97] W. Septina, S. Ikeda, A. Kyoraiseki, T. Harada, M. Matsumura, Single-step electrodeposition of a microcrystalline $Cu_2ZnSnSe_4$ thin film with a kesterite structure, *Electrochim. Acta* **88**, 436-442 (2013).

[98] M. Jeon, Y. Tanaka, T. Shimizu, S. Shingubara, Formation and characterization of single-step electrodeposited Cu_2ZnSnS_4 thin films: effect of complexing agent volume, Energy Procedia **10**, 255-260 (2011).

[99] S. G. Lee, J. Kim, H. S. Woo, Y. Jo, A. I. Inamdar, S. M. Pawar, H. S. Kim, W. Jung, H. S. Im, Structural, morphological, compositional and optical properties of single step electrodeposited Cu_2ZnSnS_4 (CZTS) thin films for solar cell application, *Curr. Appl. Phys* **14**, 254-258 (2014).

[100] E. M. Mkawi, K. Ibrahim, M. K. M. Ali, M. A. Farrukh, A. S. Mohamed, Influence of triangle wave pulse on the properties of Cu_2ZnSnS_4 thin films prepared by single step electrodeposition, *Sol. Energy Mater. Sol. Cells* **130**, 91-98 (2014).

[101] K. V. Gurav, J. H. Yun, S. M. Pawar, S. W. Shin, M. P. Suryawanshi, Y. K. Kim, G. L. Agawane, P. S. Patil, J. H. Kim, Pulsed electrodeposited CZTS thin films: effect of duty cycle, *Mater. Lett*. **108**, 316-319 (2013).

[102] K. V. Gurav, Y. K. Kim, S. W. Shin, M. P. Suryawanshi, N. L. Tarwal, U. V. Ghorpade, S. M. Pawar, S. A. Vanalakar, I. Y. Kim, J. H. Yun, P. S. Patil, J. H. Kim, Pulsed electrodeposition of Cu_2ZnSnS_4 thin films: effect of pulse potentials, *Appl. Surf. Sci.* (*In press*) (2014).

[103] J. Ge, J. Jiang, P. Yang, C. Peng, Z. Huang, S. Zup, L. Yang, J. Chu, A 5.5% efficient co-electrodeposited ZnO/CdS/Cu_2ZnSnS_4/Mo thin film solar cell, *Sol. Energy Mater. Sol.* Cells **125**, 20-26 (2014).

[104] P. Zanello, Inorganic electrochemistry: theory, practice and applications, *Royal Society of Chemistry*, 2003.

[105] M. Schlesinger, M. Paunovic, Modern electroplating, **55**. *John Wiley & Sons* (2011).

[106] D. Plaušinaitis, Metalų kompleksinių junginių elektrochemija, VU, Vilnius (2010).

[107] W. Shockley, H. J. Queisser, Detailed balance limit of efficiency of p-n junction solar cells, *J. Appl. Phys*. **32**, 510-519 (1961).

[108] L. Kaupmees, M. Altosaar, O. Volobujeva, T. Raadik, M. Grossberg, M. Danilson, E. Mellikov, P. Barvinschi, Isothermal and two-temperature zone selenization of Mo layer, *Adv. Mater. Sci. Eng.* **2012**, 11 (2011).

[109] R. M. Hansen, Adherent Electroplating on molybdenum, PhD thesis, Newark College of Engineering, New Jersey (1952).

[110] Q. Huang, K. Reuter, S. Amhed, L. Deligianni, L. T.Romankiw, S. Jaime, P. P. Grand, V. Charrier, Electrodeposition of indium on copper for CIS and CIGS solar cell applications, *J. Electrochem. Soc.* **158**(2), D57-D61 (2011).

[111] M. Slupska, P. Ozga, Electrodeposition of Sn-Zn-Cu alloys from citrate solutions, *Electrochim. Acta* **141**, 149-160 (2014).

[112] K. Obata, N. Dohi, Y. Okuhama, S. Masaki, Y. Okada, M. Yoshimoto, Tin, lead and tin-lead alloy plating baths, U.S patent 4.459.185, 1984.

[113] K. N. Tu, R. D. Thompson, Kinetics of interfacial reaction in bimetallic Cu-Sn thin films, *Acta metal*. **30**, 947-952 (1982).

[114] R. Juškėnas, Z. Mockus, S. Kanapeckaitė, G. Stalnionis, A. Survila. XRD studies of the phase composition of the electrodeposited copper-rich Cu–Sn alloys, *Electrochim. Acta* **52**, 928–935 (2006).

[115] Kh. M. S. Youssef, C. C. Koch, P. S. Fedkiw, Influence of additives and pulse electrodeposition parameters in production of nanocrystalline zinc from zinc chloride electrolytes*, J. Electrochem. Soc.* **151**(2), C103-C111 (2004).

[116] M. Ganchev, J. Iljina, L. Kaupmees, T. Raadik, O. Volobujeva, A. Mere, M. Altosaar, J. Raudoja, E. Mellikov, Phase composition of selenized $Cu_2ZnSnSe_4$ thin films determined by X-ray diffraction and Raman spectroscopy, *Thin solid films* **519**, 7394-7398 (2011).

[117] K. V. Gurav, S. M. Pawar, S. W. Shin, M. P. Suryawanshi, G. L. Agawane, P. S. Patil, J. Moon, J. H. Yun, J. H. Kim, Electrosynthesis of CZTS films by sulfurization of CZT precursor: effect of soft annealing treatment, *Appl. Surf. Sci.* **238**, 74-80 (2013).

[118] S. Furtauer, D. Li, D. Cupid, H. Flandorfer, The Cu-Sn phase diagram, part I: new experimental results, *Intermetallics* **34**, 142-147 (2013).

[119] M. Kowalski and P. J. Spencer, Thermodynamic reevaluation of the Cu-Zn system, *J. Phase Equilib.* **14** (4), 432-438 (1993).

[120] R. Juškėnas, V. Pakštas, A. Sudavičius, V. Kapočius, V. Karpavičienė, Formation of intermetallic phases during ageing of Zn electroplate on the Cu substrate, *Appl. Surf. Sci.* **229**, 402-408 (2004).

[121] T. A. Siewert, J. C. Madeni, S. Liu, Formation and growth of intermetallics at the interface between lead-free solders and copper substrates, *Proceedings of the APEX Conference on Electronics Manufacturing, Anaheim, California* **23** (7), 583-594 (2003).

[122] B. Shin, N. A. Bojarczuk, S. Guha, On the kinetics of $MoSe_2$ interfacial layer formation in chalcogen-based thin film solar cells with a molybdenum back contact, Appl. Phys. Lett. **102**, 091907 (2013).

[123] J. J. Scragg, P. J. Dale, D. Colombara, L. M. Peter, Thermodynamics aspects of the synthesis of thin-film materials for solar cells, *ChemPhysChem* **13**, 3035-3046 (2012).

[124] T. Schmidt, K. Lischka, Excitation-power dependence of the near-band-edge photoluminescence of semiconductors, *Phys. Rev. B* **45**, 8989-8994 (1992).

[125] S. R. Kodigala, $Cu(In_{1-x}Ga_x)Se_2$ based thin film solar cells, Academic Press (2011).

[126] M. Grossberg, J. Krustok, K. Timmo, M. Altosaar, Radiative recombination in $Cu_2ZnSnSe_4$ monograins studied by photoluminescence spectroscopy, *Thin Solid Films* **517**, 2489-2492 (2009).

[127] J. P. Leitao, N. M. Santos, P. A. Fernandes, P. M. P. Salome, A. F. da Cunha, J. C. Gonzalez, G. M. Ribeiro, F. M. Matinaga, Photoluminescence and electrical study of fluctuating potentials in Cu_2ZnSnS_4-based thin films, *Phys. Rev. B* **84**, 024120 (2011).

[128] R. Djemour, M. Mousel, A. Redinger, L. Gutay, A. Crossay, D. Colombara, P. J. Dale, S. Siebentritt, Detecting ZnSe secondary phase in

$Cu_2ZnSnSe_4$ by room temperature photoluminescence, *Appl. Phys. Lett*. **102,** 222108 (2013).

[129] A. Redinger, D. M. Berg, P. J. Dale, R. Djemour, L. Gutay, T. Eisenbarth, N. Valle, S. Siebentritt, Route toward high-efficiency single-phase $Cu_2ZnSn(S, Se)_4$ thin film solar cells: model experiments and literature review, *IEEE J. Photovoltaics* **1**(2), 200-206 (2011).

[130] C. Klingshirn, Semiconductor Optics, Springer New York (2001).

[131] G. Brammertz, Y. Ren, M. Buffiere, S. Mertens, J. Hendrickx, H. Marko, A. E. Zaghi, N. Lenaers, C. Koble, J. Vleugels, M. Meuris, J. Poortmans, Electrical characterization of $Cu_2ZnSnSe_4$ solar cells from selenization of sputtered metal layers, *Thin solid films* **535**, 348-352 (2013).

[132] G. Rey, A. Redinger, J. Sendler, T. P. Weiss, M. Thevenin, M. Guennou, B. E. Adib, S. Siebentritt, The band gap of $Cu_2ZnSnSe_4$: effect of order-disorder, *Appl. Phys. Lett.* **105**, 112106 (2014).

[133] J. He, J. Tao, X. Meng, Y. Dong, K. Zhang, L. Sun, P. Yang, J. Chu, Effect of selenization time on the growth of $Cu_2ZnSnSe_4$ thin films obtained from rapid thermal processing of stacked metallic layers, *Mater. Lett.* **126**, 1-4 (2014).

[134] E. H. Baker, The vapor pressure and resistivity of selenium at high temperatures, *J. Chem. Soc. A*, 1089-1092 (1968).

[135] S. Temgou, R. Bodeux, N. Naghavi, S. Delbos, Effects of $SnSe_2$ secondary phases on the efficiency of $Cu_2ZnSn(S_x,Se_{1-x})_4$ based solar cells, *Thin solid films* (In press).